ABSTRACT

Title of dissertation: SOME NOVEL PHENOMENA AT HIGH DENSITY

Evan Berkowitz, Doctor of Philosophy, 2013

Dissertation directed by: Professor Paulo Bedaque
Department of Physics

Astrophysical environments probe matter in ways impossible on Earth. In particular, matter in compact objects are extraordinarily dense. In this thesis we discuss two phenomena that may occur at high density.

First, we study toroidal topological solitons called vortons, which can occur in the kaon-condensed color-flavor-locked phase of high-density quark matter, a candidate phase for the core of some neutron stars. We show that vortons have a large radius compared to their thickness if their electrical charge is on the order of 10^4 times the fundamental charge. We show that shielding of electric fields by electrons dramatically reduces the size of a vorton.

Second, we study an unusual phase of degenerate electrons and nonrelativistic Bose-condensed helium nuclei that may exist in helium white dwarfs. We show that this phase supports a previously-unknown gapless mode, known as the half-sound, that radically alters the material's specific heat, and can annihilate into neutrinos. We provide evidence that this neutrino radiation is negligible compared to the star's surface photoemission.

SOME NOVEL PHENOMENA AT HIGH DENSITY

by

Evan Scott Berkowitz

Dissertation submitted to the Faculty of the Graduate School of the
University of Maryland, College Park in partial fulfillment
of the requirements for the degree of
Doctor of Philosophy
2013

Advisory Committee:
Professor Paulo Bedaque, Chair/Advisor
Professor Kaustubh Agashe
Professor Thomas Cohen
Professor Carter Hall
Professor Don Perlis

Dedication

For my family,
friends,
and own edification.

College Park, MD
April 2013

Acknowledgements

I owe my gratitude to all the people who have made this ~~monstrosity~~ thesis possible.

First and foremost I'd like to thank my advisor, who taught me and guided me well. I learned a great deal through the course of graduate school, and Paulo is the reason.

I would also like to thank Tom Cohen, Aleksey Cherman, Mike Buchoff, Brian Tiburzi, Prabal Adhikari, Vojtěch Krejčiřík, Srimoyee Sen, Amy Nicholson, and the rest of TQHN for being fun and interesting colleagues and for providing a lively and enlightening learning environment.

Special thanks go to Loretta Robinette, Yuri Kubota, and Jane Hessing, who always looked out for me and helped me with anything I ever asked.

Throughout my time at Maryland I have had great fortune to be monetarily supported by a Departmental Fellowship, a Research Assistantship funded under Department of Energy Grant DE-FG02-93ER-40762, a JSA/Jefferson Lab Graduate Fellowship, and the UMD Graduate School Ann G. Wylie Dissertation Fellowship.

My housemates at 1729 Kenyon Street, including in particular Daniel de Zeeuw, Eric Kuo, Erin Braswell, Ashley Meadows, Ali Recht, and Laurel Gray made living in DC a blast, and having them around made my house a home. I've also had a great group of friends in DC, including my college friends Steven Lynch, Alex Burg, John Cloutier, and Jeremy James, my "DC friends" who I met through 934 T Street, USA, and an excellent cohort of classmates as well, who made the nonacademic parts of my graduate school experience fun. I expect that the friendships I've built over the last five years will last for quite some time.

Finally, I am most grateful to have such a terrific family who always encouraged and supported me. Without my parents, sister, grandparents, and cousins, and the rest of my family, my life would have been dramatically incomplete.

Table of Contents

List of Tables

List of Figures

List of Abbreviations

BEC	Bose-Einstein Condensate
BCS	Bardeen-Cooper-Schrieffer
χPT	Chiral Perturbation Theory
CFL	Color-Flavor-Locked or Color-Flavor-Locking phase
CFL+K^0	Kaon-Condensed CFL or CFL Plus K^0
COWD	Carbon-Oxygen White Dwarf
EFT	Effective Field Theory
HeWD	Helium White Dwarf
IR	Infrared
LHS	Left-Hand Side
QCD	Quantum Chromodynamics
RHS	Right-Hand Side
SM	Standard Model
TF	Thomas-Fermi
TQHN	Theoretical Quarks, Hadrons, and Nuclei Research Group
UV	Ultraviolet
VEV	Vacuum Expectation Value
WD	White Dwarf

List of Symbols and Standard Notation

- Very often natural units ($c = \hbar = k_{\rm B} = 1$) are used without explicit mention.
- The action for a gauge theory is rationalized, or in particle physics convention, meaning $\mathcal{L} = -\frac{1}{4}F^2$ and Maxwell's equations have no explicit factors of 4π.
- On a vector (or tensor), Greek indices run from 0 to 3 while Latin indices run from 1 to 3. Vectors are sometimes written **bold**.

$\approx$	Is approximately equal to
$\propto$	Is proportional to
$\sim$	Scales like
$\gg$	Is much, much greater than
$\ll$	Is much, much less than
$\parallel$	Labeled quantity is a longitudinal degree of freedom
$\perp$	Labeled quantity is per-unit length, or is a transverse degree of freedom
$\odot$	Indicates the labelled quantity is that of the sun
$\mathbb{1}$	The unit matrix
α	Electromagnetic fine structure constant, $\alpha = e^2/4\pi \approx 1/137$
β	The coolness, the inverse temperature $1/T$
γ^μ	The Dirac matrices, $\{\gamma^\mu, \gamma^\nu\} = 2\eta^{\mu\nu}\mathbb{1}$
γ_5	The fifth gamma matrix; $\gamma_5 = i\gamma_0\gamma_1\gamma_2\gamma_3$
Γ	The ratio of Coulomb to thermal energy when a Coulomb crystal melts
Γ	The gamma function
$\Gamma(k, k')$	The annihilation probability per unit time and volume of half-sound quasiparticles with momenta k and k' into neutrinos
δ	String thickness
δ_{ij}, δ^{ij}	The Kronecker delta, 1 if $i = j$ and 0 otherwise
Δ	Superconducting gap
Δ_s	The strange axial charge, -0.16 ± 0.15
ϵ	The Levi-Civita totally-antisymmetric tensor
ζ	The Riemann zeta function
$\eta^{\mu\nu}$	The Minkowski metric, $\eta^{\mu\nu} = \text{diag}\,[+1, -1, -1, -1]$.

θ The Heaviside step function
θ_D The Debye temperature in (6.31); equal to m_A
θ_{W} The Weinberg angle, or weak mixing angle; $\sin^2\theta_{\mathrm{W}} \approx 0.24$

λ^a The generators of SU(3), the Gell-Mann matrices, normalized so $\mathrm{tr}\left[\lambda^a\lambda^b\right] = 2\delta^{ab}$
λ_{T} The thermal de Broglie wavelength

μ Chemical potential
μ_{ab} The various fictitious chemical potentials in the CFL EFT (3.2) from the commutator terms in (3.3), given explicitly in (3.7)

ξ Correlation length
ξ A gauge-fixing parameter for R_ξ gauges

π^a The eight Goldstone modes composing Σ
$\Pi^{\mu\nu}$ The electromagnetic polarization tensor
Π One of two arbitrary functions characterizing $\Pi^{\mu\nu}$, as in (5.6)
$\Pi^\perp$ One of two arbitrary functions characterizing $\Pi^{\mu\nu}$, as in (5.6)

ρ Mass density

Σ The chiral multiplet containing the eight Goldstone modes in CFL

ϕ The argument of a complex number, $z = |z|\, e^{i\phi}$
ϕ The axial coordinate in cylindrical, spherical, or toroidal coordinates
φ Any generic field, or the electric potential
Φ_B Magnetic flux

χ The electron field

ψ The second-quantized ion field.

ω_p Electron plasma frequency

a Scattering length
a Radius of the reference circle in toroidal coordinates
a_0 Bohr radius $= \hbar/\alpha m_e c \approx 5.3 \cdot 10^{-11}$ m
$\mathcal{A}$ Amplitude for a process
A A parameter of the CFL EFT (3.2), matched to QCD in (3.4).

A^μ	A gauge potential
B	Magnetic field
c	Speed of light, $\approx 3 \times 10^8$ m/s, typically set to 1
c_s	Speed of sound
c_v	Specific heat
c_H	Speed of the gapless quasiparticle of nuclear condensate (5.33)
C	The ratio $T_{\rm C}/T_{\rm Bose}$, as in (4.10)
đ	Used in integrals to denote $\mathrm{d}/2\pi$; eg. $\int đ^4p = \int \mathrm{d}^4p/(2\pi)^4$
$\mathbf{d}$	Dipole moment
D^μ	The context-appropriate covariant derivative
det	Determinant
Det	Functional determinant
e	The size of the electron's charge, roughly 0.3
E	Electric field
E_p	Energy for a given momentum p
f	The equivalent of the pion decay constant in the CFL EFT (3.2), matched to QCD in (3.4)
f_i	One of the dimensionless functions in Appendix A
F	The free energy
$F^{\mu\nu}$	The field strength tensor
g	The strong coupling constant
g_A	The nucleon axial charge ≈ 1.26
$g_{\rm W}$	The weak coupling constant, $g_{\rm W}^2 = 8G_F m_{\rm W}^2/\sqrt{2} \approx 0.426$
$g^{\mu\nu}$	The metric tensor
G_F	The Fermi coupling constant, roughly $1.17 \cdot 10^{-5}\mathrm{GeV}^{-2}$
G_N	Newton's gravitational constant, roughly $6.67 \cdot 10^{-8}\mathrm{dyne{\cdot}cm^2/g^2}$
$\hbar$	Planck's reduced constant
h	An oscillation in field magnitude, as in (5.7)
$\mathcal{H}$	Hamiltonian density
h.c.	Hermitian conjugate
Im	Imaginary part

$\mathcal{J}^{\perp}$	The angular momentum per unit length carried by a vorton in the inner toroidal region.
J	Total angular momentum
J_{out}	The angular momentum in the gauge fields in the $r > 2R$ region
k_{B}	Boltzmann's constant, $k_{\mathrm{B}} = 8.618 \cdot 10^{-5}\mathrm{eV/K}$
k_{F}	The Fermi momentum
ℓ	The inter-nucleus spacing in a high-density regime.
$\mathcal{L}$	Lagrangian density
$\mathcal{L}_{\mathrm{quad}}$	The part of the Lagrangian density at most quadratic in fields
L	Luminosity
$\mathrm{Li}_{\frac{3}{2}}$	A polylogarithm function
m	Electron mass
m_{ab}	The mass of CFL mesons at asymptotic density given in (3.6)
$m_{\pi^{\pm},\mathrm{K}^{\pm},\mathrm{K}^{0,\bar{0}}}$	Mass of the CFL mesons at non-asymptotic densities, as in (3.8)
m_q	Mass of quark species q
m_{red}	A reduced mass, as in (5.27)
m_s	Screening mass, as in (5.26)
m_A	The photon mass, as in (5.13)
m_{W}	The W-boson mass, 80.38 GeV
m_{Z}	The Z-boson mass, 91.18 GeV
M	Ion mass
M_i	Mass of species i
$\mathbb{M}$	The matrix of quark masses $\mathrm{diag}\,[m_u, m_d, m_s]$
n	Number density
n_e	Electron number density
N	Winding number of K^+ core in a CFL+K^0 vorton.
N	Nucleon isospin doublet
$\mathcal{O}$	Order of
$\widehat{\mathcal{O}}$	Any operator
P	Pressure
$\mathbb{Q}$	The matrix of quark charges under electromagnetism, $e/3\,\mathrm{diag}\,[2,-1,-1]$
$\mathcal{Q}^{\perp}$	The charge per unit length of a vorton
Q	The total charge of a vorton.

Q	Neutrino emissivity
Q	Electric charge operator in (6.5) and (6.6)
$\mathbf{r}$	The spatial coordinate
R	Vorton radius, used as an IR cutoff when appropriate
R_0	Vorton radius at equilibrium
Re	Real part
S	Action
T^3	The third component of weak isospin, as an operator $T^3 = \tau^3/2$
T	Temperature
T_{Bose}	The free Bose gas condensation temperature, as in (4.8)
T_{C}	Nuclear condensation temperature
T_{melt}	The temperature at which a Coulomb crystal melts, as in (4.5)
tr	Trace
Tr	Functional trace
u	A toroidal coordinate
v	A speed in the CFL EFT (3.2), matched to QCD in (3.4)
v	The toroidal coordinate: how far a point is from the reference circle.
v	A vacuum expectation value
v_{F}	The Fermi velocity
V	Effective potential
w	Winding number around a vortex
Z	The atomic number of a vorton or nucleus ($Z = Q/e$ for a vorton)
Z	The Z-boson

Part 0

Introduction

Compact objects are astrophysical objects that are extremely dense. The compact objects with the surest theoretical and observational footing are white dwarfs, neutron stars, black holes, while more exotic possibilities include quark stars, strange stars, and others. These objects create their high-density matter via gravitational confinement—such a technique is not realizable in an Earth-based laboratory, so these objects provide a unique way of probing an otherwise-inaccessible portion of the phase diagram of matter.

Compact stars are typically the end of a star's evolutionary lifecycle. When it is done burning its nuclear fuel, a generic main-sequence star will finish its life as a white dwarf (WD), which is held up entirely by quantum-mechanical electron degeneracy pressure. If its mass is less than the famous Chandrasekhar limit of about 1.4 solar masses, the electron degeneracy pressure will stabilize it eternally, and the remainder of the star's life will be simply radiating whatever heat it still contains.

On the other hand, if its mass is more than the Chandrasekhar limit, or if the star becomes heavier than that limit by accreting (from a binary partner, for example), or collides with another white dwarf, then the degeneracy pressure cannot sustain the star, and it will collapse in a catastrophic explosion known as a supernova. Depending on just how heavy the star is, it might collapse into a black hole or a neutron star. To get an idea of how these objects compare, a typical white dwarf density is $10^6 \mathrm{g/cm}^3$, while a typical neutron star's *crust* is that dense and its core is around 6 to $8 \cdot 10^{14} \mathrm{g/cm}^3$, or roughly comparable with nuclear density.

From a nuclear physics standpoint, a black hole is relatively uninteresting,

but both white dwarfs and neutron stars are playgrounds on which we can test our understanding of matter at high density.

This thesis is organized into two disparate, stand-alone parts, each focuses on an aspect of matter in these high-density environments.

Part 1 is about vortons, which are toroidal topological objects that can arise in a certain phase of high-density quark matter that may occur in neutron star cores. Vortons can arise in any two-bosonic-species system if both species want to condense but repel one another. If one species gets trapped in the core of a vortex loop in the bulk of the other, it can provide an angular momentum barrier that stabilizes the loop and prevents it from shrinking under its own tension.

Part 1 investigates vortons in both cold atom BECs and the more complicated case of high-density quark matter, where the quarks can pair into a BCS-like color superconductor. If the quark masses are not negligible compared to the chemical potential, the low-energy excitations of this color superconductor themselves try to condense, providing a perfect environment for vortons. The work described in this section was originally published in References [1], [2], and [3].

Part 2, is about a particular phase that may occur in white dwarfs made of helium, where the nuclei get close enough together that they become a charged Bose-Einstein condensate, neutralized by a background of degenerate electrons. We show that this condensate supports an unusual gapless quasiparticle, which we call the half-sound, that was first described in Reference [4]. We discuss two possible observational signatures that would reveal whether this phase occurs in helium white dwarf cores.

First, we show that a gas of these half-sound phonons has a very low specific heat compared to the other uncondensed phases that otherwise occur. This low specific heat may change the cooling curve of these objects, which might be detectable through careful population studies.

Second, we quantify the likelihood that two half-sound phonons annihilate and yield a neutrino-antineutrino pair. We show that this process is very large compared to the expectation from naïve dimensional analysis, but is only competitive with surface photoemission if the condensation temperature is very high. It is with this motivation that we study a similar model and show that it does not have a very high condensation temperature, so that it seems unlikely that any star's cooling curve will be noticeably altered by the fact that the star's core is radiating neutrinos. This discussion will broadly follow References [5] and [6].

Broadly speaking, then, this thesis is about two different high-density phenomena which may be relevant to the physics of compact objects.

Let us begin.

Part 1

Vortons

Introduction

A vorton is a toroidal soliton that can exist in any system of two bosonic species where the species repel one another yet each species is individually inclined to form a Bose-Einstein condensate (BEC). A vorton is a vortex loop of one species which has a core inhabited by a condensate of the second species. When a straight vortex has a charged condensate in its core it is typically referred to as a superconducting string[7]. Superconducting strings and vortons were originally discussed while trying to understand the implication of GUT-scale models on the physics of the early universe[8].

Vortices, which we will discuss in Chapter 1, terminate at the boundaries of the bulk they live in, or can be thought to have infinite extent. They have a property known as *winding number* which characterizes the vorticity of the surrounding field. The winding number, as we will see, is an integer and thus cannot change smoothly from one value to another: it is conserved in time. Therefore, we are guaranteed that vortices with winding number 1 are stable.

We should refine the notion of winding number conservation a bit. Globally, winding number is conserved, but two vortices might combine to form a new vortex whose winding number was the original vortices' sum, or a vortex with a large winding number might split into smaller vortices. If two vortices with exactly opposite winding numbers encounter one another, they can even annihilate, leaving no vortex at all. Nonetheless, after the vortices have had time to settle down, their nonzero winding number guarantees there will be some vortices about.

Vortices need not be pinned to the boundary. Instead, a vortex might close

on itself—making a loop. If a vortex is reminiscent of a tornado or hurricane, then a vortex loop is a smoke ring. In this case the winding number characterizes the circulation of the field through the loop.

It is hard to see how to stabilize a vortex loop alone: any point and the one directly across the center of the loop will have opposite winding numbers and therefore could annihilate. Thus, vortex loops in single-species systems typically shrink from their own tension, eventually collapsing to nothing. If they are in motion relative to the bulk, such vortices might be sustained by the Magnus force.

For a vorton, however, the situation is different. The existence of the second species provides dynamical stability even if the loop is at rest relative to the bulk. If the two species repel one another, then the second species can live in the "eye" of vortices of the first species.

If the second species has nonzero conserved quantities, like electric charge or angular momentum, it can give the loop a stable equilibrium radius. In particular, if the core species might have a winding number l of its own, as indicated in Figure 1. In this case, the energy E of a vorton with radius R will scale like

$$E = TR + \frac{l^2}{R} \tag{1}$$

where T is the tension that shrinks a regular vortex loop. In contrast, it is easy to see that an energy of this form is minimized for some finite R_0, so that the equilibrium circumstance is a vorton that is stable against shrinking itself to nothing.

Suppose there was a region filled with a bulk of condensate of one species. Strong enough repulsive interactions ensure that it is energetically unfavorable for

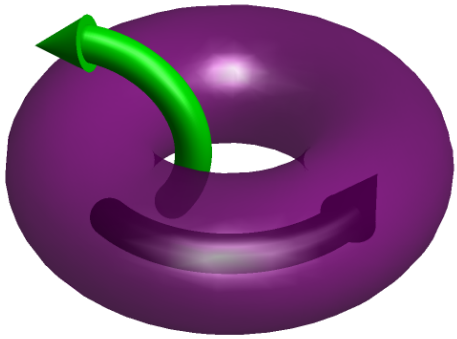

Figure 1: The purple torus separates the bulk species from the interior core species. The winding of the circulation of the bulk is indicated by the green arrow, while the winding of the inner species is indicated in black.

any of the second species to also be in that region, so before discussing vortons it is prudent to understand the vortices that arise in a single-species condensate.

In the first chapter of this part we will discuss a simple vortex, and in the following chapters we will discuss two different systems that support vortons: two-species cold-atom laboratory experiments and the color-flavor-locked phase of high-density quark matter. The cold-atom case follows the story here, while the dense quark matter case is more subtle because they are electrically charged, and both gauge invariance and overall charge neutrality add nontrivial complication. It is thus prudent to understand the cold atom case before the high density case. Cold atom vortons are discussed in Chapter 2; dense matter vortons in Chapter 3.

Chapter 1

Typical Vortices

Simple BECs support vortices. A vortex is a one-dimensional defect. A vortex in a real medium stretches across the bulk and terminates in two places on its boundary, or eventually shrinks to nothing under the influence of its own tension. In order to avoid discussing the specifics of the size, shape, and boundary of the bulk, it is often most simple to think about the bulk being infinitely large, in which case the vortex is infinitely long. It is also simplest for many purposes to consider a straight vortex.

In this chapter we will review the topological stability of straight vortices, and discuss how to determine their tension. These results will be used in the discussion of vortons in later chapters of this part.

1.1 Topological Stability of a Vortex

To understand the topological properties of an infinitely long straight vortex, one may simply consider a cross-sectional slice, and then translate that slice along the length of the vortex. The boundary of such a two-dimensional slice can be entirely parameterized by an angle $\theta \in [0, 2\pi)$, the axial coordinate.

The ground state of a condensed complex scalar (or pseudoscalar) φ can be

described by a real magnitude f and a phase ϕ that changes from place to place,

$$\varphi(\mathbf{r}) = f(\mathbf{r})\, e^{i\phi(\mathbf{r})}, \tag{1.1}$$

where $\mathbf{r}$ is the coordinate in space. In most systems the ground state will be homogeneous, so that ϕ can be set to zero by a global phase convention and $f(r) = v$ and we call v the vacuum expectation value (VEV). The phase ϕ also takes values in the range $[0, 2\pi)$. We can think of ϕ at any fixed radius (including the limiting value $r = \infty$) as a function of θ. Because θ represents a physical location and the condensate must be single-valued, we know that ϕ must be periodic in θ, modulo 2π. That is, it must be that

$$\phi(r, \theta + 2\pi) = \phi(r, \theta) + 2\pi w \tag{1.2}$$

where w is any integer and we suppress the z dependence under the assumption of translational symmetry. This directly encodes the fact that the first homotopy group of the circle, $\pi_1(S^1)$, is the group of integers, $\mathbb{Z}$. Any two distinct $\phi(\theta)$s may be smoothly transformed into one another if they have the same w, while if they have distinct w no smooth transformation can exist. Such functions are said to be topologically distinct, or to belong to different topological sectors, or to have different winding numbers.

The winding number of a particular φ around some region containing the origin may be calculated by integrating the logarithmic derivative of φ around a

curve that goes around that region once

$$2\pi w \equiv \oint d\mathbf{r} \cdot ((-i\nabla)\log\varphi) = -i\log\left(\frac{\varphi(r_0,\theta_0+2\pi)}{\varphi(r_0,\theta_0)}\right) \tag{1.3}$$

$$= -i\log\left(e^{i(\phi(r_0,\theta_0+2\pi)-\phi(r_0,\theta_0))}\right) = -i\log\left(e^{2\pi i w}\right) \tag{1.4}$$

where r_0 and θ_0 specify some point on the curve, as long as that curve avoids regions where $f(\mathbf{r})$ vanishes. The second line follows from the first because by single-valuedness $f(r,\theta+2\pi) = f(r,\theta)$, and the final equality follows from (1.2). If $f(\mathbf{r})$ vanishes the field is automatically single-valued without the restriction (1.2), and moreover we cannot take the logarithmic derivative and the winding number along the curve is not well-defined. As long as we do not encounter anyplace where $f(\mathbf{r})$ vanishes we are free to deform the curve however we like and we are guaranteed to get the same answer. If we take the curve to be the boundary at infinity, then we say that whole two-dimensional slice has winding number w.

That no smooth transformation can connect functions with different winding numbers implies three things. First, suppose the winding number around some region is nonzero. Then, somewhere in that region $f(\mathbf{r})$ must vanish. This is most simply illustrated by example. Let

$$\varphi(\mathbf{r}) = f(r)e^{iw\theta}, \tag{1.5}$$

the typical axially-symetric vortex ansatz, where we only require $f(r=\infty) = v$. It is easy to verify that the winding number is w. Because $w \neq 0$, the value of φ at the origin would be multivalued unless $f(0) = 0$.

Secondly, if one slice of a vortex has winding number w, so do all the other

slices. In this case simply consider the smooth transformation to be translation along the vortex. We therefore say the whole vortex has winding number w.

Finally, if the time evolution of such a configuration is smooth, it must be that the winding number is conserved in time, so that we can never take a field configuration that starts with some winding number and evolve it to a configuration with another winding number without creating regions where the VEV vanishes. Because a field typically develops a VEV to minimize energy in the first place such a change will be a tunneling process; such a change cannot be the result of the classical equations of motion. We therefore say that winding number is conserved in time, even though extraordinarily rare quantum fluctuations might allow us to escape this conclusion.

1.2 Vortex Tension

A major factor in the evolution of a vortex is its tension. If both ends of a vortex are not tethered to something rigid, then the vortex will shrink along its length until it disappears. It is therefore important to understand how to compute the tension of such an object.

The tension T of a vortex is simply the energy per unit length of the field configuration with the vortex with the energy per unit length of the condensed ground-state subtracted off.

Let us consider, for example, a model where the Lagrangian is given by

$$\mathcal{L} = |\partial\varphi|^2 - V\left(|\varphi|^2\right) \tag{1.6}$$

with a potential that has a global minimum at $|\varphi|^2 = v^2$. The ground state is homogeneous: $\varphi_0(\mathbf{r}) = v$, while an axially-symmetric vortex with winding number w can be generically parameterized by $\varphi(\mathbf{r}) = f(r)\exp(iw\theta)$, with $f(r)$ some function that needs to be determined and that will depend on the potential $V\left(|\varphi|^2\right)$.

In this model $f(r)$ will minimize the energy per unit length, which is naïvely the integral of the Hamiltonian density

$$T\left[\varphi(\mathbf{r})\right] = \int \mathrm{d}^2 r\ \mathcal{H} = \int \mathrm{d}^2 r\ \ |\partial\varphi|^2 + V\left(|\varphi|^2\right). \tag{1.7}$$

Because $V(|v|^2)$ need not be 0, this integral is divergent. This divergence is superficial, and reflects the fact that the cross-section that we consider is infinite in extent. The correct expression for the tension is

$$T\left[f(r), w\right] = T\left[f(r)e^{iw\theta}\right] - T\left[v\right] \tag{1.8}$$

which can be considered simply a shift of the potential, zeroing it at $|v|^2$. If we expect that the system will minimize its energy then this expression not only determines the tension as a function of the radial profile: it also dictates that the preferred radial profile $f(r)$ should minimize $T\left[f(r), w\right]$. We should note here that in most cases if $|w| > 1$, a single vortex with winding w is disfavored and instead $|w|$ vortices of winding number ± 1 (following the sign of w) is energetically preferred.

Depending on the situation, we may require field configurations to have certain quantities conserved. In that case, instead of minimizing the Hamiltonian density, we will minimize an analogous expression that allows us to minimize the action subject to those constraints by incorporating Lagrange multipliers (which act like chemical potentials) and their corresponding conserved quantities. While these technical steps

might differ, the simple understanding and procedure for regularizing the relevant per-unit-length quantities discussed here are directly analogous.

Chapter 2

Vortons in Two-Species BECs

Since the initial laboratory creation of BECs in cold atom traps experimental capabilities have developed rapidly, so that such set-ups are commonplace, allowing for a plethora of interesting detailed studies of BEC physics. In particular, experimentalists can reliably create two-species condensates in such traps (for some examples see Refs. [9, 10, 11]) and such systems are known to support vortices, vortons, and another class of topological soliton: the Skyrmion[12, 13]. Moreover, the manipulation of Feshbach resonances[14, 15] afford the experimenter the ability to tune interactions (usually one at a time) as they like[16]. For a relatively recent review of this technique, see Reference [17]. These circumstances raise the possibility that vortons might be observed in the laboratory as a matter of course or even might be created purposefully as objects of interest in their own right.

This chapter will closely follow Reference [3]. We will discuss straight vortices with condensed cores in two-species BECs, the corresponding vortons, and mechanisms by which such vortons can arise in the laboratory. For concreteness we will focus on lithium-rubidium systems and potassium-rubidium systems. Numerical studies that will be discussed in Sec. 2.2 indicate that when the ratio of mass of the species making up the bulk to the mass of the species which resides in the vortex core is large, the corresponding vortons have a larger aspect ratio R/δ. We therefore

typically discuss systems where the bulk is rubidium. We will provide evidence that these realistic systems can contain observable vortons.

It is simpler to read, write, think, and think clearly about "lithium" and "rubidium" than "species 1" and "species 2". Therefore, we may in the text use lithium and rubidium as names of the two species, but until specific masses or scattering lengths are plugged in the discussion may be understood as general and these names as mere convenience.

2.1 Vortices with Condensed Cores

Cold-atom traps are easily used to trap spinless nonrelativistic bosons. When these bosons are dilute, meaning that the relevant scattering lengths are much smaller than the interparticle spacing, they are well-described by the Hamiltonian

$$\mathcal{H} = \frac{\hbar^2}{2M_{\mathrm{Rb}}} \left|\nabla\varphi_{\mathrm{Rb}}\right|^2 + \frac{\hbar^2}{2M_{\mathrm{Li}}} \left|\nabla\varphi_{\mathrm{Li}}\right|^2 + V(\varphi_{\mathrm{Rb}}, \varphi_{\mathrm{Li}}), \tag{2.1}$$

with

$$\begin{aligned} V(\varphi_{\mathrm{Rb}}, \varphi_{\mathrm{Li}}) = \quad & \frac{1}{2}\frac{8\pi\hbar^2 a_{\mathrm{Rb}}}{M_{\mathrm{Rb}}} \left|\varphi_{\mathrm{Rb}}\right|^4 + \frac{1}{2}\frac{8\pi\hbar^2 a_{\mathrm{Li}}}{M_{\mathrm{Li}}} \left|\varphi_{\mathrm{Li}}\right|^4 \\ & + \frac{2\pi\hbar^2 a_{\mathrm{RbLi}}}{M_{\mathrm{RbLi}}} \left|\varphi_{\mathrm{Rb}}\right|^2 \left|\varphi_{\mathrm{Li}}\right|^2 - \mu_{\mathrm{Rb}} \left|\varphi_{\mathrm{Rb}}\right|^2, \end{aligned} \tag{2.2}$$

where φ_i is a second-quantized field that annihilates species i ($i \in \{\mathrm{Li}, \mathrm{Rb}\}$), a_i and M_i are that species' scattering length and mass, a_{RbLi} is the interspecies scattering length and M_{RbLi} is the reduced mass. The chemical potential μ_{Rb} incentivizes the uniform condensation of rubidium. Ignoring effects of the lithium and at leading

order in the diluteness expansion ($n_{\mathrm{Rb}}^{-1/3}$ and $n_{\mathrm{Li}}^{-1/3} \ll a_{\mathrm{Rb}}$, a_{Li}, and a_{RbLi}),

$$\mu_{\mathrm{Rb}} = \frac{8\pi\hbar^2 a_{\mathrm{Rb}}}{M_{\mathrm{Rb}}} n_{\mathrm{Rb}}, \tag{2.3}$$

where n_{Rb} is the asymptotic number density of the rubidium.

We treat the lithium and rubidium asymmetrically because of the physical situation we will be interested in: a vast bulk of rubidium that forms a reservoir that essentially fixes the density of rubidium and a conserved number of lithium atoms that are stranded in the core of a vortex in that bulk.

We enforce the fact that the lithium atoms are trapped in the core by restricting ourselves to the situation when the two species are phase-separated, meaning that the interspecies repulsion makes a uniform mixture of both species unstable against clumping and separating in space. This instability turns on when

$$\frac{4a_{\mathrm{Rb}}a_{\mathrm{Li}}}{M_{\mathrm{Rb}}M_{\mathrm{Li}}} < \left(\frac{a_{\mathrm{RbLi}}}{M_{\mathrm{RbLi}}}\right)^2 \tag{2.4}$$

and prevents the lithium from leaking out of the vortex core[18]. By artificially manipulating a_{RbLi} with the Feshbach resonance tuning technique, one may toggle or enhance this instability.

Condensation is characterized by a non-vanishing matrix element of the respective field operator φ. When the system is dilute in the sense mentioned above, the mean-field approximation becomes accurate and the matrix elements themselves obey the classical equations of motion—the Gross-Pitaevski equations. For convenience we will represent the matrix element by the same symbol as the operator itself.

A straight vortex of a single species is well described by the ansatz (1.5),

$$\varphi_{\mathrm{Rb}}(\mathbf{r}) = f_{\mathrm{Rb}}(r)e^{iw\theta} \tag{2.5}$$

where r and θ are cylindrical coordinates and the ansatz is invariant under translations along z, the axial coordinate. To keep φ_{Rb} single-valued w must be an integer and $f_{\mathrm{Rb}}\left(r=0\right)=0$. The chemical potential μ_{Rb} entices the asymptotic value to simply reflect the bulk density, $f_{\mathrm{Rb}}\left(r\rightarrow\ \infty\right)=\sqrt{n_{\mathrm{Rb}}}$. Energetically, if $|w|>1$, the vortex will split into $|w|$ vortices of equal winding, so we will always take $w=1$, but keeping w general provides a quick way to identify phenomena that are connected to the vorticity.

The radial profile $f_{\mathrm{Rb}}(r)$ may be determined by solving the Gross-Pitaevski differential equations with the boundary conditions $f_{\mathrm{Rb}}(0)=0$, $f_{\mathrm{Rb}}(\infty)=\sqrt{n_{\mathrm{Rb}}}$. Alternatively, it may be determined by equivalently minimizing the energy with respect to $f(r)$, which is the approach we will take throughout this work. This approach limits us to discussing equilibrium and prevents us from making a detailed study of the dynamical stability of the resulting field configurations. The dynamical stability of Skyrmions has been demonstrated by detailed numerical calculations[19, 20], but we are satisfied to determine the equilibrium properties with significantly less effort and then to argue the stability of vortons.

In order to understand how thick the single-species vortex is, let us make a simple variational argument from (2.1) with $\varphi_{\mathrm{Li}}=0$. A constant may be added to $\mathcal{H}$ so that

$$\mathcal{H}=\frac{\hbar^2}{2M_{\mathrm{Rb}}}\left|\nabla\varphi_{\mathrm{Rb}}\right|^2+\frac{1}{2}\frac{8\pi\hbar^2a_{\mathrm{Rb}}}{M_{\mathrm{Rb}}}\left(\left|\varphi_{\mathrm{Rb}}\right|^2-n_{\mathrm{Rb}}\right)^2+\mathcal{O}\left(n_{\mathrm{Rb}}^2\left|\varphi_{\mathrm{Rb}}\right|^0\right). \tag{2.6}$$

A rough guess for the shape of $f_{\mathrm{Rb}}(r)$ might be a simple linear rise from 0 at the origin to $\sqrt{n_{\mathrm{Rb}}}$ at radius δ, so that the gradient of f_{Rb} near zero is simply $\sqrt{n_{\mathrm{Rb}}}/\delta$. With a field profile of that form, the energy is easily computed to be

$$E(\delta) = \int_0^R 2\pi r \mathrm{d}r \; H = \frac{n_{\mathrm{Rb}}\pi}{6M_{\mathrm{Rb}}}\left(3 + 3w^2 + 8an\pi\delta^2 + 6w^2 \ln\left(\frac{R}{\delta}\right)\right) \tag{2.7}$$

where R is an IR cutoff. This energy is minimized by a thickness

$$\delta = \frac{\sqrt{3}w}{\sqrt{8\pi a_{\mathrm{Rb}} n_{\mathrm{Rb}}}}, \tag{2.8}$$

which is sensibly R-independent. So, the string thickness is of the scale $1/\sqrt{8\pi a_{\mathrm{Rb}} n_{\mathrm{Rb}}}$, also called the healing length, and is proportional to the winding number. The factor of $\sqrt{3}$ depends on the profile being linear; picking another reasonable profile will change this pure number but not the parametric dependence of the string thickness δ on the scattering length or density.

So far our discussion has been limited to the case when φ_{Li} vanishes. Instead let us consider the case when the mean-field solution takes the form

$$\varphi_{\mathrm{Rb}} = f_{\mathrm{Rb}}(r)e^{iw\theta} \quad \text{as before and} \quad \varphi_{\mathrm{Li}} = f_{\mathrm{Li}}(r)e^{ikz}. \tag{2.9}$$

Using these functional forms in (2.1) and the energy per unit length $E_\perp$ is

$$E^\perp = \int \mathrm{d}r \; 2\pi r \Bigg[\frac{\hbar^2}{2M_{\mathrm{Rb}}}\left(\left(\frac{\partial f_{\mathrm{Rb}}}{\partial r}\right)^2 + \frac{w^2}{r^2} f_{\mathrm{Rb}}^2\right) + \frac{\hbar^2}{2M_{\mathrm{Li}}}\left(\left(\frac{\partial f_{\mathrm{Li}}}{\partial r}\right)^2 + k^2 f_{\mathrm{Li}}^2\right) + V(f_{\mathrm{Rb}}, f_{\mathrm{Li}}) + \frac{1}{2}\frac{8\pi\hbar^2 a_{\mathrm{Rb}}}{M_{\mathrm{Rb}}} n_{\mathrm{Rb}}^2 \Bigg], \tag{2.10}$$

where the last term has been added to zero the energy of the homogeneous ground state: $w = 0$, $f_{\mathrm{Rb}}(r) = \sqrt{n_{\mathrm{Rb}}}$, and $f_{\mathrm{Li}}(r) = 0$.

Since we require, for stability purposes, the interspecies interaction to be repulsive, we know $a_{\mathrm{RbLi}} > 0$. Then, by looking at the potential, it is obvious that the field profiles which minimize $E^{\perp}$ definitely have $f_{\mathrm{Li}}(r) = 0$. This, however, corresponds to a vortex loop without any condensate in its core. However, we have not yet included the fact that the number of lithium atoms is fixed and that these atoms are trapped in the core. To incorporate this requirement into the case of an infinitely long vortex we should minimize the energy per unit length with the number of lithium atoms per unit length

$$N_{\mathrm{Li}}^{\perp} = \int \mathrm{d}r \; 2\pi r \; f_{\mathrm{Li}}^2(r) \tag{2.11}$$

fixed. This incentivizes f_{Li} to take nonzero values, while the repulsive lithium-rubidium interaction encourages the lithium to occupy the rubidium vortex core, where f_{Rb} goes to zero and the repulsive interaction energy is least.

A nonzero k in (2.9) corresponds to the inner species flowing along the axis of the vortex (and will correspond to flowing around the vorton). That k not vanish will therefore be important to provide an angular momentum barrier. However, we should note that a larger k tends to reduce the lithium condensate in much the same way that forcing too much current through a superconductor can quench the superconductivity (as happened, for example, to the LHC magnets). This effect will be made more explicit in Section 3.2.1.

With the expressions for straight vortices in hand we can now discuss vortons.

2.2 Vortons

A vorton is a toroidal vortex loop with a condensed core, or, more simply, a loop of superconducting string. When the aspect ratio R/δ is large, the curvature corrections are small and the expression for the energy per unit length (2.10) becomes a reliable approximation to the true energy per unit length.

With the realization that the energy of a straight superconducting string reliably approximates the energy of a superconducting loop when $R/\delta \gg 1$, we can think of a vorton as simply a straight superconducting string in space that is periodic along its length. In particular, let $z = \pm\pi R$ be identified. Then the arc length along the vorton is simply the extent of the superconducting string. The periodicity in z also supplies a constraint: any field must obey

$$\varphi(r, \theta, z - \pi R) = \varphi(r, \theta, z + \pi R). \tag{2.12}$$

In particular, this means that the phase of lithium in (2.9) must be

$$k = \frac{l}{R} \tag{2.13}$$

where l is an integer. This l is the winding number of the lithium's phase around the vortex loop in much the same way w is the winding number of the rubidium's phase around the boundary, and can be computed given a field configuration by direct analogy with w in (1.3).

What is the effect of neglecting the curvature effects by this compactification? The energy of a straight vortex in a compactified space will have no gradients along the length of the vorton, and these gradients are guaranteed to raise the

energy. Therefore we expect that doing a more precise calculation with a curved loop should yield an equilibrium radius larger than one calculated with the present approximation, so that our calculations of R_0/δ should be considered pessimistic.

With the quantization of k in place we can now see how the inner condensate provides stability and protects the vorton against shrinking to nothing. The total energy and total number of lithium atoms are given by

$$E = 2\pi R E^{\perp} \quad \text{and} \quad N_{\mathrm{Li}} = 2\pi R N_{\mathrm{Li}}^{\perp} \tag{2.14}$$

respectively. The energy scales like

$$E \sim 2\pi R T + \frac{L^2}{R} \tag{2.15}$$

where T simply denotes the part of $E^{\perp}$ that is independent of R and L^2 characterizes the remaining terms (solely the term proportional to k). We see that one term scales like R and another like R^{-1}. This guarantees that the vorton does not shrink forever but instead stabilizes at some finite equilibrium radius R_0. What is the origin of this stabilization?

For a superconducting string, k parameterizes the current that flows in the condensed core. Bending that current into a loop obviously gives rise to an angular momentum perpendicular to the plane of circulation. Moreover, the fact that this piece of the energy scales like R^{-1} indicates that this stabilizing term is indeed coming from an angular momentum barrier.

Minimizing E with respect to f_{Rb}, f_{Li}, and R while holding N_{Li}, n_{Rb}, a_{Rb}, a_{Li}, a_{RbLi}, M_{Rb}, M_{Li}, w and l fixed yields good candidate field configurations. We will always take $w = 1$ so that the Rubidium vortex cannot split apart. The sign of w

is conventional, in the sense that the two vortons with opposite w have exactly the same equilibrium size, since the energy is an even function of w.

Performing such a minimization cannot be done analytically. However, some behaviors are easy to predict. For example, a larger angular momentum should naturally lead to a larger equilibrium radius but should not change the string thickness too drastically. Therefore, increasing l should increase R_0 and R_0/δ.

Another dependence that is easy to understand is how things should change as a function of the interspecies scattering length. As that interaction becomes more and more repulsive, the region where the two species coexist should shrink, so that eventually increasing a_{RbLi} should not matter any more.

Contrastingly, how some parameters affect the aspect ratio are not so easy to predict. For example, as espoused in the introduction to this chapter, when the ratio of the mass of the bulk species to the mass of the core species is large, R_0/δ grows. This is why we primarily focus on rubidium and lithium, and even use their names as handy placeholders. However, that R/δ grows with $M_{\mathrm{Rb}}/M_{\mathrm{Li}}$ is by no means obvious. Decreasing M_{Li} increases the energy (and pressure) of a given field profile and vorton shape. If we could adjust the mass of the inner species, the vorton would respond by altering itself in two ways: making the field profile wider (and thus increasing δ) or making the vorton longer (and thus increasing R_0). It is difficult to argue *a priori* which increase will be larger, and therefore whether a large mass ratio helps justify the geometrical approximation $R_0/\delta \gg 1$ must be determined numerically.

2.3 Realistic Numbers

Let us now discuss realistic cold atom numbers. For concreteness and experimental relevance we take the condensates to be the $| F = 1, m_F = 1 \rangle$ hyperfine states of their respective species. For the bulk condensate we will use realistic numbers of ^{87}Rb, while the core species might be either ^{7}Li or ^{41}K[21, 22, 23, 24]. The interspecies scattering length a_{RbLi} can be tuned through the use of a Feshbach resonance[16], guaranteeing that we are always in the phase-separation regime.

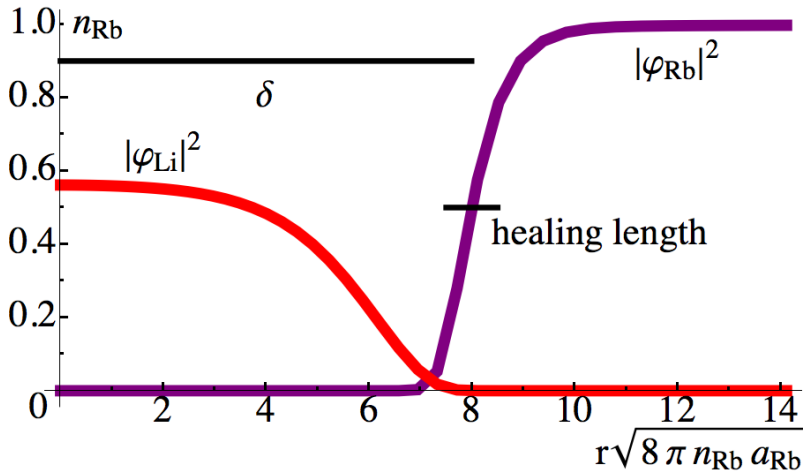

Figure 2.1: The field profiles for ^{7}Li (red) and ^{87}Rb (purple), with $l = 5$ and all other parameters given by the first row of Table 2.1. The string thickness δ and the healing length $(8\pi n_{\mathrm{Rb}} a_{\mathrm{Rb}})^{-\frac{1}{2}}$ are shown in black for easy reference. Because the natural scale for the radial changes are given by the rubidium healing length, we scale the radial coordinate by that amount. We similarly show the densities in units of n_{Rb}. This figure is a modified version of a figure first produced for Reference [3].

In order to numerically minimize the energy with a fixed number of lithium atoms, given in (2.14), we pick the two species, which amounts to picking the two

masses and three scattering lengths (one may be tuned by an external magnetic field), the asymptotic number density of the rubidium, and the number of trapped lithium atoms. The question becomes: how do we know how many lithium atoms we should require to keep the vorton stable and big enough?

If the scattering lengths of the two species are similar (as is the case for the atomic systems of interest), then it is reasonable to think that the vorton will be stabilized when the densities (and thus pressures) are roughly comparable. Thus, we can estimate the required number of lithium atoms by simply multiplying the cross section of the vorton $\pi\delta^2$, where δ is of order of the healing length by the vorton's length $2\pi R$. If we then specify a rough aspect ratio R_0/δ that we want the vorton to have, we can estimate

$$N_{\mathrm{Li}} \approx 2\pi \left(\frac{R_0}{\delta}\right) \delta \ \pi\delta^2 n_{\mathrm{Li}}. \tag{2.16}$$

So for example, a bulk of rubidium with number density around $10^{13}\mathrm{cm}^{-3}$ has a healing length of roughly $0.45\mu m$. If we want a vorton with $R_0/\delta \approx 2.5$ then we can use (2.16) to learn that such a vorton should require roughly 10^4 lithium atoms.

With this estimate in hand, we can now perform numerical minimizations where we expect the vortons to be of reasonable size. Such a minimization leads to radial profiles like the one shown in Figure 2.1, which was produced with the parameters specified by the first line of Table 2.1. The angular momentum number $l = 5$ was motivated by current limitations of Gauss-Laguerre beam technology, which will be further discussed in Section 2.4.2. We see that the scale on which the rubidium changes is indeed roughly the healing length, and that the string thickness

δ is also of this scale (it is roughly 7 or 8 times larger in this case). In Table 2.1 we show the numerical results for a few experimentally reasonable choices of the species, bulk density, the number of trapped core atoms, and the density of the bulk species. We see that all of these choices yield vortons of reasonable size with R_0/δ around 2. This ratio is not that large, meaning that curvature corrections to the energy in (2.14) may not be negligible. However, as argued earlier, these corrections are expected to make vortons larger, and thus we expect the reported R_0/δ ratios to be underestimates. These results make it reasonable to pursue more detailed numerical simulations of vortons and may justify experimental investigation.

2.4 Production Mechanisms

With the stability of reasonably-sized and reasonably-proportioned vortons established, we should now ask: can vortons be realized easily in the laboratory? There are two mechanisms that we will discuss by which vortons might be produced. The first, the Kibble-Zurek mechanism[25, 26], works by taking a hot system and rapidly cooling it, quickly eliminating thermal fluctuations and locking in whatever topological quantities where there by chance. The second, using Raman scattering and Gauss-Laguerre beams, is a method that is more technically challenging but should allow an experimenter to create vortons intentionally.

Table 2.1: R_0/δ for different values of parameters for $l = 5$.

Scattering lengths are given in terms of the Bohr radius $a_0 \approx 0.53$Å.

The interspecies scattering length can be made large by Feshbach resonance techniques.

The lengths R_0 and δ are in units of μm and the density of the bulk is given in cm^{-3}.

Species 1	Species 2	M_1/M_2	a_1/a_0	a_2/a_0	a_{12}/a_0	n_1	N_2	R_0	δ	R_0/δ
^{87}Rb	^{7}Li	12	100	40	5000	4×10^{13}	2×10^{4}	7.9	3.4	2.3
^{87}Rb	^{7}Li	12	100	40	5000	4×10^{12}	2×10^{4}	19	7.6	2.5
^{87}Rb	^{7}Li	12	100	40	5000	4×10^{13}	2×10^{3}	4.4	1.7	2.5
^{87}Rb	^{41}K	2.12	100	85.5	5000	4×10^{13}	2×10^{4}	5.3	3.1	1.7
^{87}Rb	^{41}K	2.12	100	85.5	5000	4×10^{12}	2×10^{4}	12	6.3	1.9
^{87}Rb	^{41}K	2.12	100	85.5	5000	4×10^{13}	2×10^{3}	2.8	1.4	1.9

2.4.1 The Kibble-Zurek Mechanism

The topological winding numbers w and l provide a vorton with stability at low temperatures, where thermal fluctuations cannot dissipate vorticity by, for example, sending the condensate in some region to zero. This suggests one way to create vortons: start at a high temperature, where the phase of the fields are uncorrelated beyond some length, and cool it fast enough that the phases in different places do not have time to correlate. One possible configuration of the phases in such a system is that the vorticity around a certain region is nonzero, meaning that there is a vortex. These vortices are left over as defects in much the same way crystals or magnets can have planes where two misaligned crystal structures or magnetic domains meet.

Rapid cooling locking in vortices is called the Kibble-Zurek mechanism, and was first understood in the context of early-universe cosmology[25, 27, 26, 28], but has shown up in a variety of physical circumstances (for some good examples see Refs. [28, 29, 30]) and is known to survive spatial inhomogeneities[31]. Moreover, experiments have verified this mechanism producing vortices in trapped ^{87}Rb[32].

Suppose we tuned via Feshbach resonance the interspecies scattering to be negligible, so that the system was not in the phase-separation regime specified by (2.4), and the system was warm enough so that the phase of the rubidium atoms were uncorrelated. Then, quenching the system could create vortices in the rubidium and subsequently tuning the interspecies scattering length to turn on the phase-separation instability should cause those vortices to trap nearby lithium atoms.

Any net vorticity that the lithium has will provide a finite angular momentum and sustain such a vorton.

Modeling such a process is complex, but some reasonable assumptions and simple arguments can help us approximate the likelihood of such a vorton arising. We first assume that we can cool rapidly so that the phases of both fields in each place are the same before and after the cooling, so that the phases remain uncorrelated from place to place. If we can turn on the phase-separation instability quickly, the lithium atoms will quickly get ejected or become trapped by the potential created by the rubidium bulk.

If we assume that the two species are decoupled before the cooling, the vorticity of each is governed by its respective correlation lengths. The correlation lengths ξ_{Rb} and ξ_{Li} can be estimated to be the inverse of the typical phonon momentum at the initial temperature, $k = T/c_s$, where

$$c_s = \sqrt{4\pi a n}/M \tag{2.17}$$

is the speed of sound for the appropriate species, so that the correlation length is

$$\xi = \frac{TM}{4\pi a n}. \tag{2.18}$$

The correlation length of the rubidium will set the scale on which vortices are created (out of equilibrium) and by which they are separated. The rubidium vortices will be oriented randomly, so that some of the neighboring vortices will be oriented in the opposite sense, or so that a few of the neighboring vortices will form a directed cycle where the angular momentum around each vortex points towards the next vortex. These vortices can connect to form a loop. This process is topological

in the sense that if the correlation length were scaled up with the other relevant lengths, the same vortices would still form a loop. We therefore know that the number of vortices that form a loop is given by some fixed probability distribution having to do with combinatorics and nothing else.

Of these vortices, we should try to understand what fraction will be stabilized by their core of trapped lithium. As we have seen, a nonzero l (or equivalently, a net angular momentum around the loop) is required to stabilize a vorton with finite R_0. Following an argument from Reference [26] let us estimate this winding number now.

The winding number l is given, by analogy with (1.3),

$$2\pi l = \oint \mathrm{d}\mathbf{s} \cdot (-i\nabla \log \varphi_{\mathrm{Li}}) = \oint \mathrm{d}\mathbf{s} \cdot \nabla \left(\text{phase of } \varphi_{\mathrm{Li}}\right) \tag{2.19}$$

where $\mathbf{s}$ is the length differential around the loop. Because the phase of φ_{Li} is uncorrelated on the length scale ξ_{Li}, it should change between 0 and π roughly $2\pi R/\xi_{\mathrm{Li}}$ times. However, because of the random nature of thermal fluctuations it is extremely unlikely that the phase should always go in one direction, but instead should randomly increase or decrease by π that many times. Therefore, we expect the total change in phase to be 2π times the typical distance moved in a one-dimensional random walk in $2\pi R/\xi_{\mathrm{Li}}$ steps. In other words, we expect

$$|l| \sim \sqrt{\frac{2\pi R}{\xi_{\mathrm{Li}}}} \tag{2.20}$$

$$\approx \sqrt{2\pi \frac{M_{\mathrm{Rb}}}{M_{\mathrm{Li}}}} \left(\frac{a_{\mathrm{Li}} n_{\mathrm{Li}}}{a_{\mathrm{Rb}} n_{\mathrm{Rb}}}\right)^{1/4} \tag{2.21}$$

where we used $R \sim \xi_{\mathrm{Rb}}$ in the second line. We see the advantage of using atoms with disparate masses: if the bulk species is much heavier than the inner species,

the likelihood that the Kibble-Zurek mechanism produces vortons with large angular momentum is enhanced. We could also try to create systems with a very sparse bulk and a dense inner species—such a scenario would similarly help enhance the angular momentum of the vorton.

2.4.2 Raman Scattering and Gauss-Laguerre Beams

The Kibble-Zurek mechanism is simply one of odds—in each run of the experiment one is stuck with the vortices that thermal fluctuations provided initially. We now address how vortons might be created intentionally by the experimentalist. The idea behind this procedure was suggested to us by Porto[33].

A loop of vortex could be created in the bulk by using two counter-propagating beams tuned in a particular fashion. The first frequency should be chosen to take the bulk and move it to an excited state; the second should match the transition from the excited state to a different state in the hyperfine multiplet of the original. Let us denote these two frequencies ω_a and ω_b, and note that the requirement that ω_b returns the excited state to the same hyperfine multiplet implies ω_a and ω_b are nearly equal. One well-known choice for the excited state would be the D_1 line of rubidium.

By aligning lasers of the two frequencies in opposite directions atoms will absorb a photon of the first frequency and thus momentum $\hbar k = \hbar\omega_a/c$. Then, by stimulated emission the same atoms emit photons in the opposite direction, so that it gains a momentum $\hbar\omega_b/c$, for a total momentum of $\hbar(\omega_a + \omega_b)/c$. This allows us

to take a part of the bulk and give it a net flow in one direction.

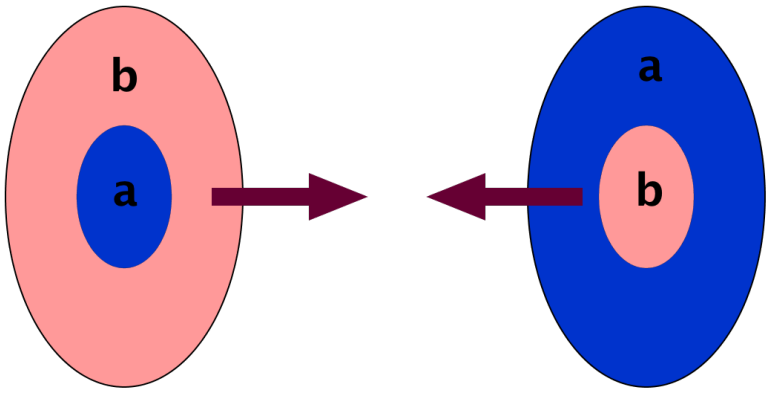

Figure 2.2: The geometry of the two counter-propagating beams. The two colors (and letters) represent the two frequencies, while the dark red arrow represent the direction of propagation. Figure reproduced from Reference [3].

Now it is easy to make a vorton. If, instead of the beams being wholly one frequency or the other, we arrange it so that the cross-section of one beam could have a disk of one frequency surrounded by an annulus of the other frequency, while in the other beam the frequencies would be switched, as shown in Fig. 2.2, the central cylinder would be kicked one way, while the rest of the bulk would be kicked the other way. At the cylindrical interface, there would be dramatic shearing, which would very likely lead to the creation of vortex loops.

This injection of momentum could potentially throw the atoms out of the trap. For example, the D_1 transitions mentioned earlier would give the atoms energy of the order of 10μK. By making the lasers dim and limiting the number of optically scattered atoms, these high-energy atoms could scatter off of nearby atoms and distribute their optically-gained momentum, diluting the large deposited energy.

With these vortex loops created in the rubidium bulk, one need only tune the system into the phase-separation regime described by (2.4). Then, as in the Kibble-Zurek mechanism, the lithium will quickly leave the rubidium bulk by either totally fleeing it or by taking shelter in the rubidium vortices.

Once trapped, the vorton can be stabilized by giving the lithium atoms a net angular momentum around the loop. This can be accomplished with Gauss-Laguerre beams[34, 35], which are beams with annular cross-sections and helical phases. For some good visualizations of such beams, see Reference [36]. To understand how this can spin up the lithium, imagine an infinite Archimedes screw, but from a perspective that rotates with the screw and translates with the rising water. From this point of view, the water simply spins cyclicly around the screw's core. This is a reasonable way to imagine how Gauss-Laguerre beams impart angular momentum around the vortex loop.

These helical beams are regularly produced in laboratories, and higher-order beams (beams with large orbital angular momentum) can be made with great fidelity. Current technology limits small beams to $l \lesssim 5$, which motivated our choice $l = 5$ when displaying some numerical predictions for vorton size in Table 2.1, as vortons with larger angular momentum are intuitively going to be larger than vortons with smaller angular momentum. With improvements to beam generation technology, one expects a larger attainable l and thus larger equilibrium vortons[37, 38].

⋆ ⋆ ⋆

This concludes our discussion of vortons in atomic traps. In the next chapter we

will investigate another system which supports vortons: the kaon-condensed color-flavor-locked phase of quark matter. We will make extensive use of the intuition and terminology developed here, but as we will see, when the species involved are charged scalars subtleties involving gauge invariance complicate the relatively simple procedure discussed here, as well as introduce far-field effects that aid stabilization.

Chapter 3

Vortons in Kaon-Condensed Color-Flavor-Locked Quark Matter

A large fraction of the content in this chapter is either directly reproduced verbatim from or prominently inspired by my candidacy paper[39].

3.1 The Kaon-Condensed Color-Flavor-Locked Phase

At high temperature it is clear that Quantum Chromodynamics (QCD) is weakly-coupled and perturbative, and one might therefore expect that QCD is also perturbative at high density. However, in the last decade or so, it has become clear that even though it is weakly coupled, the true behavior at finite density is a non-perturbative color-superconducting phase[40, 41, 42]. This presents a difficulty for understanding high-density phenomena from first-principles, because we lack a good computational method for extracting non-perturbative behavior directly from the QCD Lagrangian. At zero density, we can use direct lattice simulations to inform our understanding, but at finite density the Euclideanized action remains complex, rendering the usual strategy of estimating the partition function by importance sampling the functional integral exponentially difficult—an issue known as the fermion sign problem.

Instead, we are forced to rely on an effective field theory (EFT) approach to describe such color-superconducting phases. These phases arise in essentially

the same manner as normal electromagnetic superconductivity arises in familiar systems—the Cooper pairing of fermions. In contrast to familiar superconductors in which the only species free to pair are electrons, the nonabelian structure of QCD's $SU(3)_C$ gauge group provides a large number of imaginable pairings.

For phenomenologically interesting densities (eg. conceivable densities of neutron star cores), we only need to concern ourselves with the three lightest quark flavors. For a good review of the most widely expected phases in this case and some calculational methods required for this kind of analysis see References [42, 43]. Among the the possible pairings with three quark flavors and three colors is a particularly symmetrical Cooper pairing scheme, which characterizes the phase known as color-flavor-locked matter (or sometimes simply color-flavor-locking; abbreviated CFL either way). At asymptotically high density, the symmetry breaking pattern is known because QCD becomes weakly coupled, shoring up the EFT on which we will rely.

The coincidental matching between the number of phenomenologically relevant flavors and the number of colors the quarks in the SU(3) fundamental representation can carry allows one to pair all of the quarks. The condensate is characterized by[44]

$$\left\langle q^a_{L,i} C q^b_{L,j} \right\rangle = -\left\langle q^a_{R,i} C q^b_{R,j} \right\rangle \sim \mu^2 \Delta \, \epsilon^{abZ} \epsilon_{ijZ} \tag{3.1}$$

where the Δ is the superconducting gap and ϵ the Levi-Civita tensor. The quark fields q are labeled by color indices i and j that run from 1 to 3, flavor indices a and b that run over {up, down, and strange}, and chiral labels L and R that represent the left- and right-handed parts of the spinor. We can treat the two chiral components

independently when the quark chemical potential μ is much larger than the quark masses. That CFL is the preferred ground state may be motivated heuristically by noticing that it allows the largest conceivable number of Cooper pairs to form, and pairing tends to deform the Fermi surface and save energy.

Because of its non-singlet color structure, this symmetry breaking pattern obviously is not gauge invariant. There are equivalent gauge-invariant order parameters[42], but it is typically simplest and most convenient to discuss the problem with the clearer language afforded by glazing over this subtlety. One concern may be that these colored quark pairs violate confinement, but the size of these pairs is smaller than the confinement scale (roughly 1 fm), which we know from the high densities (and thus small inter-particle spacing) where CFL may exist.

The condensate in (3.1) also assumes perfect SU(3) flavor symmetry. For asymptotically high densities, the quark masses are negligible and this assumed symmetry is justified and is enhanced to $\mathrm{SU(3)_L} \times \mathrm{SU(3)_R}$. As we lower the density, however, at some point the strange quark mass m_s will make non-negligible corrections to the behavior of the system. The quark masses act as explicit $\mathrm{SU(3)_F}$-breaking terms. We will discuss how to incorporate such explicit flavor breaking below.

This CFL condensate breaks the overall $\mathrm{SU(3)_L} \times \mathrm{SU(3)_R} \times \mathrm{SU(3)_C} \times U(1)_\mathrm{B} \times U(1)_\mathrm{A}$ symmetry to $\mathrm{SU(3)_{C+L+R}} \times \mathbb{Z}_2 \times \mathbb{Z}_2$. The two $\mathbb{Z}_2$ symmetries are remnants of the two initial U(1) symmetries (the exact baryon and approximate axial symmetries) and correspond to sending $\{q_L, q_R\} \rightarrow \{-q_L, \mp q_R\}$. The remaining $\mathrm{SU(3)_{C+L+R}}$ (sometimes written $\mathrm{SU(3)_{CFL}}$) is a common diagonal to the three orig-

inal SU(3) groups.

As in any symmetry-broken phase, the low-energy dynamics of a CFL condensate are described by Goldstone modes. The modes resulting from the pairing in (3.1) resemble the familiar pseudoscalar mesons which arise from the breaking of chiral symmetry in the vacuum.

The number of Goldstone modes is set by the number of broken generators. In this case there are $(3\times 8+1+1)-8 = 18$ broken generators. Eight of these are eaten by gluons, which pick up a mass $g\mu$, where g is the strong coupling constant[45]. This is one hallmark of color superconductivity.

The condensate also breaks the electromagnetic $\mathrm{U}(1)_{\mathrm{EM}}$ contained in $\mathrm{SU}(3)_{\mathrm{L+R}}$. However, a linear combination of one diagonal generator of the $\mathrm{SU}(3)_{\mathrm{C}}$ gauge group with the $\mathrm{U}(1)_{\mathrm{EM}}$ generator still annihilates the condensate. This leads to a remnant $\mathrm{U}(1)_{\mathrm{Q}}$ gauge symmetry, which we will refer to as electromagnetism for simplicity. In fact, the difference between $\mathrm{U}(1)_{\mathrm{EM}}$ and $\mathrm{U}(1)_{\mathrm{Q}}$ is small when the electromagnetic fine structure constant α ($\approx 1/137$) is small[46] compared to $g^2/4\pi$ (which is roughly .2 in these circumstances).

The ten uneaten generators are the physical Goldstone modes and together compose the light degrees of freedom in the CFL phase. Two of these modes are associated with the generic superfluidity associated with breaking $\mathrm{U}(1)_{\mathrm{B}}$ and $\mathrm{U}(1)_{\mathrm{A}}$. The other eight modes for a multiplet under the remaining $\mathrm{SU}(3)_{\mathrm{CFL}}$ symmetry, just as the eight familiar mesons transform under the approximate $\mathrm{SU}(3)_{\mathrm{F}}$ flavor symmetry of Gell-Mann. The EFT that describes these modes is therefore strikingly similar to familiar chiral perturbation theory (χPT) used to describe low-energy

QCD vacuum-meson dynamics[47, 48, 49].

At asymptotically high density, where the flavor symmetry is exact, the Goldstone modes are exactly massless. However, when the quark masses are taken into account, the smallness of the explicit breaking will correspond to these modes' lightness, just as the pion's light mass is explained by isospin breaking. In fact, the analogy with breaking Gell-Mann's $\mathrm{SU}(3)_{\mathrm{F}}$ flavor symmetry is used in naming the degrees of freedom these Goldstone modes encode. So, very often "kaon", "pion", and "eta" correspond not to the familiar *in vacuo* mesons but to the Goldstone modes that arise in the CFL phase unless explicitly mentioned—typically context is enough to distinguish these two uses.

The explicit flavor breaking has two effects. The first is that, as mentioned above, the Goldstone modes get small masses. Interestingly, the mass hierarchy is mixed up compared to the familiar vacuum mesons. For example, the chiral singlet, analogous to the η' and associated with $\mathrm{U}(1)_{\mathrm{B}}$ breaking, is lightest. The lightest modes in the chiral singlet are the neutral kaons and charged kaons (which are almost degenerate) and the pions and eta are heavier. This mass hierarchy will be made explicit once we have the effective Lagrangian.

The second explicit effect of the flavor breaking is a fictitious chemical potential term that enters the time-like derivatives. This chemical potential may be thought of as a correction to the ultra-relativistic limit, so that energies of order of the Fermi momentum k_{F} are corrected to $k_{\mathrm{F}} - m_q^2/2k_{\mathrm{F}}$, where m_q^2 represents some combination of the relevant quark masses. As this correction becomes appreciable (i.e. as the density is lowered) the mesons have their mass-squared reduced, until the mass-

squared of the lightest meson (the neutral kaon) reaches zero and becomes negative. To resolve this instability, the neutral kaons condense and form a superfluid. Once the neutral kaons condense, the phase is called kaon-condensed CFL, or CFL+K^0.

Through interactions, the K^0 condensate prevents the other Goldstone modes from condensing. As we will see, the condensation of K^0 over K^+ is only favored by small effects like isospin breaking and electromagnetism. Therefore, generically it is only through interactions that K^+ is prevented from condensing—if one could remove the K^0 condensate, it would create a place for $K^+$to condense. With our knowledge from Chapter 2 we know that these ingredients are enough to create vortons. There are various subtleties, though, that complicate the analysis compared to that simple case. For example, K^+ is charged, and the vorton core will be electromagnetically superconducting and can carry electromagnetic charge. As we will see, the gauging of this field causes significant complication.

3.1.1 The CFL+K^0 Effective Lagrangian

Let us now formalize the description of the CFL and CFL+K^0 phases.

The EFT for these Goldstone modes can be written in terms of a chiral multiplet Σ which transforms under $\mathrm{SU(3)_L} \times \mathrm{SU(3)_R}$ as $\Sigma \to g_L \Sigma g_R$, where $g_{L,R}$ are group elements of the indicated SU(3). The eight Goldstone modes are the fluctuations about the expectation value of Σ, Σ_0. The modes π^a parameterize Σ by $\Sigma = \exp(i\pi^a \lambda^a / f)\Sigma_0$, where λ^a are the eight generators of SU(3) with $\mathrm{tr}\left[\lambda^a \lambda^b\right] = 2\delta^{ab}$ and f is analogous to the pion decay constant.

The lowest-order effective Lagrangian density required to capture both the CFL and CFL+K^0 phases is

$$\begin{aligned}\mathcal{L}_{\text{eff}} =& \frac{f^2}{4}\,\text{tr}\left[\nabla_0\Sigma^\dagger\cdot\nabla_0\Sigma - v^2 D_i\Sigma^\dagger\cdot D_i\Sigma\right] - \frac{1}{4}F_{\mu\nu}F^{\mu\nu} \\ &+ 2A\,\det\left[\mathbb{M}\right]\,\text{tr}\left[\mathbb{M}^{-1}\Sigma + \text{ h.c. }\right]\end{aligned} \tag{3.2}$$

where the derivatives are

$$D_\mu\Sigma = \partial_\mu\Sigma - iA_\mu\left[\mathbb{Q},\Sigma\right] \quad \text{and} \quad \nabla_0 = D_0\Sigma + i\left[\frac{\mathbb{M}\mathbb{M}^\dagger}{2k_{\text{F}}},\Sigma\right], \tag{3.3}$$

k_{F} is the Fermi momentum (which we will often simply take to be the chemical potential μ), A_μ is the electromagnetic potential, $\mathbb{Q} = \frac{e}{3}\,\text{diag}\left[2,-1,-1\right]$ is the quark charge matrix under the $\text{U}(1)_{\text{Q}}$ symmetry, $F_{\mu\nu}$ is the associated field strength tensor, and $\mathbb{M} = \text{ diag}\left[m_u, m_d, m_s\right] \approx \text{ diag}\left[2,5,95\right]$ MeV is the quark mass matrix.

One interesting aspect of this Lagrangian is the $\mathcal{O}\left(\mathbb{M}^2\right)$ mass term. This term differs from the usual term in χPT, which is linear in $\mathbb{M}$. This can be thought about in a heuristic manner that drives to the heart of the matter. A single mass insertion transforms a left-handed quark into a right-handed quark, and vice-versa. However, the condensate in (3.1) preserves left- and right-handed quark number modulo 2; single mass insertions would disrupt this property. Indeed, at low densities the usual chiral condensate $\langle\,\bar{q}_R q_L\,\rangle$ will become non-negligible and allow the two chiralities to mix.

The mass term in effective Lagrangian given in (3.2) is not the only possible $\mathcal{O}\left(\mathbb{M}^2\right)$ term, but all other possible terms are suppressed by powers of Δ/μ according to the power scheme given in Reference [50].

There are two other differences between this effective Lagrangian and the canonical χPT Lagrangian. First, the theory has a preferred frame and differentiates between space and time derivatives. The second is the modification of the time derivatives with the commutator term. This term is a result of demanding gauge invariance while integrating out the gluons, but may also be thought of as the first-order correction to the ultra-relativistic approximation, $E = p + m^2/2p$. Gauge invariance fixes the coefficient of this correction. Since these commutator terms modify the time derivative, we can think about their effect in exactly the same way we think about chemical potentials.

Typically when we construct an effective theory there are constants in the effective Lagrangian that are simply unknown and incalculable, and that must be fit. In contrast, the constants in the effective Lagrangian in (3.2) can be calculated at asymptotically high density where the additional terms in the effective theory are guaranteed to be very small and QCD is calculable. This matching yields

$$f^2 = \frac{21 - 8\ln 2}{18}\frac{\mu^2}{2\pi^2}, \quad , v^2 = \frac{1}{3}, \quad \text{and} \quad A = \frac{3}{4\pi^2}\Delta^2, \tag{3.4}$$

and the details of this calculation can be found in References [45, 47].

The equations of motion for the gauge potentials are

$$\begin{aligned} \partial_\mu F^{\mu 0} &= -\frac{f^2}{4}\,\mathrm{tr}\left[i\nabla^0\Sigma^\dagger \cdot [\mathbb{Q}, \Sigma] + \text{ h.c.}\right] \\ \partial_\mu F^{\mu i} &= -\frac{f^2}{4}\,\mathrm{tr}\left[iD^i\Sigma^\dagger \cdot [\mathbb{Q}, \Sigma] + \text{ h.c.}\right]. \end{aligned} \tag{3.5}$$

It is straightforward to read off the expressions for the electrical charge and current. We note that there is a subtlety: a field that has no time dependence still carries charge. In fact, the time-dependence of the fields is not a gauge-invariant concept:

only time-variation, chemical potential, and electromagnetic gauge potential taken together are gauge invariant.

When the chemical potentials are small compared to μ, they do not affect the expectation value of Σ, and we can read off the masses as an expansion around $\Sigma_0 = \mathbb{1}$. This describes the CFL phase. Let us examine these masses now.

First, define

$$m_{ab} = \sqrt{\frac{4A}{f^2} m_c \left(m_a + m_b\right)} \tag{3.6}$$

where c is the quark flavor not specified by a and b. This is the form of explicit, k_{F}-independent meson masses that the $\mathcal{O}\left(\mathbb{M}^2\right)$ mass term provides. Also define

$$\mu_{ab} = \frac{m_a^2 - m_b^2}{2k_{\mathrm{F}}}, \tag{3.7}$$

the fictitious chemical potential arising from the $\mathbb{M}\mathbb{M}^\dagger/2k_{\mathrm{F}}$ commutators. Note that all of these chemical potentials vanish as $k_{\mathrm{F}} \to \infty$. Finally, note the symmetry $m_{ab} = m_{ba}$ and antisymmetry $\mu_{ab} = -\mu_{ba}$. With this notation in hand the masses of the mesons are

$$m_{\pi^\pm} = m_{ud} \pm \mu_{ud}, \quad m_{\mathrm{K}^\pm} = m_{us} \pm \mu_{us}, \quad \text{and} \quad m_{\mathrm{K}^{0,\bar{0}}} = m_{ds} \pm \mu_{ds}, \tag{3.8}$$

At asymptotic densities all the μ_{ab} vanish and the meson pairs are degenerate, but non-negligible quark masses favor one of each pair over the other. The neutral pion and eta mesons have masses of a similar form, but as they lie on the diagonal when other fields vanish they commute with the $\mathbb{M}\mathbb{M}^\dagger$ matrix in the covariant timelike derivative and thus are never split or enticed to condense, regardless of the size of the chemical potential term.

Note that compared to chiral perturbation theory the mass hierarchy at asymptotic density is inverted: $m_{\mathrm{K}^{0,\bar{0}}} < m_{\mathrm{K}^{\pm}} < m_{\pi^{\pm}}$. This ordering is easy to see by simply examining how each depends on the greatest quark mass, m_s, in (3.6). Even though the chemical potential for the charged kaons μ_{su} is slightly greater than the chemical potential for the neutral kaons, the neutral kaons start out with a lower mass and will get to zero mass, and thus will condense, first. This small isospin-breaking effect is compounded by the fact that the K^+ meson is charged and for the system to remain neutral any charged particle must come along with a charge-balancing electron (or positron) which may cost a significant amount of energy—the Fermi energy. There are some loopholes which may favor K^+, including the effect of fluctuations of the gauge field, which can actually lower m_{K^+}[51]. We will ignore these loopholes and assume that K^0 condenses.

With all of the other fields vanishing, the vacuum expectation value of the K^0 condensate is given by[50]

$$\cos\left(\frac{\left|\mathrm{K}^0\right|\sqrt{2}}{f}\right) = \frac{m_{sd}^2}{\mu_{sd}^2}. \tag{3.9}$$

If the right-hand side is more than 1, then the neutral kaons do not condense. Because μ_{sd} vanishes at asymptotically high densities we know that above some density the K^0 condensate cannot exist. At lower densities the the K^0 condensate is a neutral superfluid. A similar relation would hold for the K^+ condensate if the K^0 were for some reason prevented from condensing. We therefore expect that the K^+ could condense in a K^0 vortex.

One consideration for these superconducting strings is the effect of the explicit

breaking of the phases associated with K^0 and K^+ by weak interactions. This breaking amounts to tipping the canonical Mexican-hat potential used to describe Goldstone modes. The result is that the phase that wraps around vortices does not wrap homogeneously—instead it barely changes throughout most of the wrapping and then quickly changes through almost the entirety of 2π. This domain-wall like feature must terminate on the vortex, so one can imagine it as a membrane stretched across the middle of a vorton. As such, vortons in CFL+K^0 are sometimes called "drum vortons"[52]. However, the thickness of the domain wall is so much larger than radii or the vortons we will find, that the "fast" change by 2π is not noticeable[53]. Moreover, the effect arises from weak interactions, so it already provides only a small correction to vorton behavior. For these reasons, we henceforth ignore this effect.

3.2 Unshielded Vortons

Because CFL+K^0 superfluid condensate breaks K^0 number, it supports global vortices. Vorticity manifests itself as a phase that wraps around the center of the vortex. In order for the field to remain single-valued, it must vanish at the vortex's core. Thus, at the core of the K^0 vortices, the interactions that might otherwise prevent the K^+ from condensing disappear.

In contrast to some familiar superfluid EFTs (for example, superfluid ^{4}He), the EFT for the CFL+K^0 mesons is valid to short enough scales that the core of K^0 vortices is within the regime of validity. Thus, it is sensible to discuss the possibility

of a K^+ superconducting core for K^0 vortices. Upon the formation of a charged condensate, the vortices will be superconducting; superconducting wires may have an overall electrical charge and carry current.

Since the pions are much heavier than the kaons, we will assume that they play no role in vorton behavior and simply turn them off. We will keep all of the "electromagnetic" $U(1)_Q$ dynamics, and keep all the nonlinear inter-meson interactions. Previous studies of CFL vortons similarly ignored the pions, but also ignored the $U(1)_Q$ dynamics and linearized effective Lagrangian.

Our strategy for discussing vortons is the following: since we are interested in equilibrium properties, any valid field configuration must minimize not just the action, but the Lagrangian. Attempting to capture the full toroidal geometry is quite difficult, so instead we will separate space into three regions. The first region is the space within the torus of radius R and thickness R, where we treat the vorton simply as a straight superconducting string length $2\pi R$. The second is the space outside of the sphere of radius $2R$, where the gradients in the K^0 condensate are negligible but the electromagnetic effects are not. The third space between these two surfaces, the apple-core shaped region, which we will neglect for simplicity; this uncontrolled approximation should make the vortons configurations we find smaller than true configurations, so that the aspect ratios we find should be considered pessimistic. A cross-section is shown in Figure 3.1; rotating that slice about the vertical axis gives the three spatial regions. Since we are interested in configurations where it is easy to distinguish a toroidal vorton from a configuration that looks more like a bialy or red blood cell, we require the radius to be much larger than the core of the vortex,

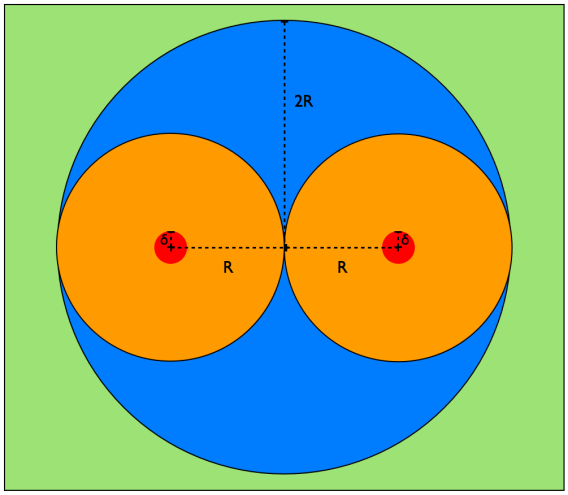

Figure 3.1: The three regions we consider: the inner torus (orange in color), the apple-core shape (blue), and the region outside the sphere (green). The radius R should be significantly larger than the string thickness δ. Figure reproduced from Reference [1].

whose radius is characterized by the string thickness δ. Since we will require $R \gg \delta$ anyway, we are justified in neglecting the terms arising from the curvature of the vortex by treating the inner torus as simply a straight vortex of length $2\pi R$.

Let us first consider an infinite, straight K^0 vortex. If z is the direction along the vortex, the K^0 field generically takes the form

$$\mathrm{K}^0 = \mathrm{K}^0(r)e^{iw\theta} \tag{3.10}$$

where ϕ is the axial coordinate, r the axial distance, and w the vorticity, in direct analogy to (1.5). As was argued there, $\mathrm{K}^0(r)$ ought vanish at $r = 0$. Additionally, infinitely far away the vortex should not matter and the field should take the value

given by (3.9). Thus, we know that $\mathrm{K}^0(r)$ has the limits

$$\mathrm{K}^0(0) = 0 \quad \text{and} \quad \mathrm{K}^0(\infty) = \frac{f}{\sqrt{2}} \arccos\left(\frac{m_{sd}^2}{\mu_{sd}^2}\right). \tag{3.11}$$

In the straight vortex case, we will think of the z-direction as straight; in the case of the vorton we will think of it as it as tangential to the vortex core.

To describe a charge- and current-carrying K^+ condensate at the center of the vortex we take

$$\mathrm{K}^+ = \mathrm{K}^+(r)e^{i(\omega t - kz)} \tag{3.12}$$

where the frequency ω contributes to the charge density, t is time, and k is the wavenumber along the $z-$direction which contributes to the current. All that is known on general grounds about the function $\mathrm{K}^+(r)$ is that it should be flat at $r = 0$ (as cusps there should be energetically costly) and should diminish relatively quickly with the radial coordinate (due to interactions with K^0).

As in the cold-atom case, the phase of the core species along the vortex, in this case K^+, will provide an angular momentum barrier. Because K^+ is charged and the phase k contributes to an electrical current, this barrier simply reflects the fact that two antiparallel currents (those on opposite sides of the vorton) repel.

Before extremizing the Lagrangian, we must decide which quantities should be held constant—which quantities we will consider conserved. The electric charge of a vorton can only change by the conversion of a charged kaon into a neutral kaon (and the absorption of an electron, and the emission of a neutrino). This weak process should proceed slowly, as the volume of K^+ is smaller than the surrounding electron clouds (as we will discover). Eventually, this process will reach equilibrium; the final

state will be vortons with no electric charge (and thus, we will find, no vorton at all). We will concern ourselves with timescales much shorter than this equilibration process, so that we can consider the electric charge to be conserved.

The angular momentum may similarly be changed, either by the emission of a kaon or a photon. Again, we consider timescales much shorter than that so that we can consider the angular momentum to be constant. The estimation of these timescales we leave for future work. There is one more fixed quantity: the winding number of the K^+ field along the vorton.

The quantization of k was already discussed in Sec. 2.2 and first for CFL+K^0 vortons in Reference [52]. However, neither discussion considered full gauge-covariant derivatives. The effects are somewhat subtle. The time-dependent phase of the K^+ field in (3.12) can be changed by $U(1)_Q$ gauge transformations, and is thus is not an observable. In contrast, the z-dependent phase is quantized

$$k = \frac{N}{R} \tag{3.13}$$

and the winding number N remains a physical observable, since it cannot be changed by periodic gauge transformations (that is, group transformations continuously connected to the identity).

Given a loop of superconducting wire, the quantization of the fluxoid connects N to the magnetic flux Φ_B that threads the superconducting loop and the current density j^z at the loop's center by [54]

$$2\pi N = e\Phi_B - \oint dz \frac{j^z(r=0)}{\frac{f^2v^2}{2e}\,\mathrm{tr}\left[\left|[\mathbb{Q},\Sigma]\right|^2\right]}. \tag{3.14}$$

In most familiar condensed matter systems, the superconducting sample is large

compared to the London penetration length $1/m_\gamma$ so the current that flows through the center of the loop is exponentially small. Then the integral term in (3.14) is negligible and it then appears as though the magnetic flux itself is quantized. While qualitatively the flux and fluxoid are different entities, quantitatively they are very similar in this "thick-wire" case. Cosmic strings, on the other hand, are typically analyzed in the "thin" wire approximation[7], where the current might penetrate deep into the wire and erase any evidence of the quantization of magnetic flux. In our case, we will find that the penetration length might be comparable to the thickness of the wire; the vortex not obviously in the "thick" or "thin" wire regime. Thus, for us the distinction between the fluxoid and the flux is quite significant.

Next, even though in principle A_z and N/R (or more properly Φ_B and N) are independent physical observables, they do not enter calculations separately. Instead they appear in just such a combination so that they always give the current density j^z; this can be traced to the fact that the contributions of A_z and N/R both originate in the $U(1)_Q$ covariant derivative $D_z = \partial_z + A_z$. This poses a puzzle, because although N is conserved, it does not determine the current, and we cannot deduce how the current should change as the radius of the vorton changes. In fact, the Lagrangian enjoys a discrete symmetry—if we increase N by 1 and the magnetic flux by $2\pi/e$, the resulting vorton will have the same current, and so the Lagrangian will not differ for these two different vortons.

In the ungauged case the dependence of the current density j on the vorton radius R is quite straightforward: $j \sim k \sim N/R$. This scaling was, in fact, used to argue for the stability of the ungauged vorton in Section 2.2. However, the gauge

invariance could conceivably cause trouble—could it be that the gauge field could arrange itself in such a way that it cancels the R^{-1} behavior of j? As will be made explicit in (3.43), a stabilizing effect of this sort survives through the conservation of angular momentum.

We have argued that in order to describe a vorton, we should specify *both* N and the magnetic flux — these quantities together give the current. If we specify both the current and the charge, we can compute the angular momentum, and only through the angular momentum do these quantities enter the calculation of the size of a vorton. Instead of specifying both N and Φ_B, we will therefore just specify the angular momentum. Thus, when we specify the angular momentum, we are actually discussing a whole class of vortons whose magnetic flux and winding number conspire to give the specified value of the angular momentum. While vortons supporting different amounts of magnetic flux and winding number are in principle physically distinct objects, the stability and equilibrium properties of vortons related by having the same angular momentum must be the same.

Therefore, when we minimize the Lagrangian, we should aim to keep the charge and angular momentum fixed. The simplest way to accomplish this conceptually is to use Lagrange multipliers. We define

$$F = \nu Q + \Omega J - L_{\text{eff}} \tag{3.15}$$

and recognize that extremizing F extremizes L_{eff} and therefore solves the equations of motion while guaranteeing that the field configuration has the required conserved quantities. We will need to eliminate the Lagrange multipliers ν and Ω in favor of

their respective conserved quantities, charge Q and angular momentum J.

The functional F is a global quantity. As discussed earlier, we should compute F by integrating over all space. We approximate this integral by separating the whole space into the torus, the apple-core (which we neglect), and the region outside of the sphere, as shown in Figure 3.1. This allows us to break up F into two parts:

$$F = F_{r>2R} + 2\pi R\, \mathcal{F}^{\perp} \tag{3.16}$$

where

$$\mathcal{F}^{\perp} = \int_0^R d^2r\ \nu\mathcal{Q} + \Omega\mathcal{J} - \mathcal{L} \tag{3.17}$$

and where $\mathcal{Q}$ and $\mathcal{J}$ are the charge and angular momentum densities, respectively, and $F_{r>2R}$ is the contribution to F from outside of the sphere of radius $2R$. We will compute $\mathcal{F}^{\perp}$ by simply taking the fields to be those of an infinite straight vortex, which becomes exact in the limit $R \gg \delta$. We will make a variational ansatz which will make computation of $F_{r>2R}$ simple, as it will have no charge density in this region and the angular momentum will only be carried in the electromagnetic fields. In Section 3.3 we will remedy some of the violence of the approximations made in calculating F outside of the torus of radius R by solving for the electromagnetic fields and surrounding electrons numerically.

To progress any further, we must compute F. In Section 3.2.1 we compute $\mathcal{F}^{\perp}$, and in Section 3.2.2 we compute $F_{r>2R}$.

3.2.1 Straight Superconducting Vortices

As discussed above, a straight, infinitely-long K^0 vortex implies that the K^0 field takes the form

$$\mathrm{K}^0 = \mathrm{K}^0(r)e^{iw\theta} \tag{3.18}$$

where w is the vorticity, θ the axial coordinate, with the boundary conditions

$$\mathrm{K}^0(0) = 0 \quad \text{and} \quad \mathrm{K}^0(\infty) = \frac{f}{\sqrt{2}} \arccos\left(\frac{m^2_{\mathrm{K}^0}}{\mu^2_{sd}}\right). \tag{3.19}$$

For definiteness, and upon energetic grounds, we will consider only $w = 1$. Since this vortex can have a K^+ condensate at its core, without loss of generality we can let K^+ take the form

$$\mathrm{K}^+ = \mathrm{K}^+(r)e^{i(\omega t - kz)} \tag{3.20}$$

where ω and k are part of the gauge-covariant quantities that enable the K^+ field to carry charge and current, with boundary conditions

$$\mathrm{K}^+(\infty) = 0 \quad \text{and} \quad \partial_r \mathrm{K}^+(0) = 0. \tag{3.21}$$

These charges and currents source electromagnetic fields.

Motivated by axial symmetry, we can pick a gauge where two of the gauge potentials vanish, $A_\phi = A_r = 0$. The four coupled, nonlinear equations for $\mathrm{K}^0(r)$, $\mathrm{K}^+(r)$, $A_0(r)$ and $A_z(r)$ of motion follow simply from (3.2). Unfortunately, even in the case of an infinite straight vortex they are not solvable analytically. Instead, we will assume a simple ansatz which captures the overall behavior of the kaons. We will *not* pick an ansatz for the gauge fields but instead will solve their equations of motion.

The simplest ansatz that has all of the radial behavior we expect for the kaon fields is

$$\mathrm{K}^0(r) = \left|\mathrm{K}^0\right| \theta(r-\delta), \quad \text{and} \quad \mathrm{K}^+(r) = \left|\mathrm{K}^+\right| \theta(\delta - r), \tag{3.22}$$

where δ is the string thickness. We treat both $\left|\mathrm{K}^+\right|$ and δ as variational parameters, but fix $\left|\mathrm{K}^0\right|$ to be its expectation value given by (3.9). Obviously, these step functions are a drastic over-simplification and do not solve the equations of motion; the real radial profiles should be continuous and differentiable, and should overlap one another. However, these profiles allow us to solve analytically the electromagnetic equations of motion and understand how the size of the condensates are affected by the electromagnetic fields. They therefore allow us to develop good intuition for how the solutions behave and to drive to the heart of the conceptual difficulties gauge invariance brings.

Treating $\left|\mathrm{K}^+\right|$ and δ as variational parameters means that our ansatz has fixed square profiles, but electromagnetic effects can change the vortex width and the photon mass (which we will see depends on the charged condensate). When we solve the equations of motion for the gauge field, it is convenient to use only gauge-invariant quantities. These combinations are

$$\tilde{\omega}(r) = \omega - eA_0(r) - \mu_{su} \quad \text{and} \quad \tilde{k}(r) = k + eA_z(r). \tag{3.23}$$

Alone, the time dependence ω, the size of the gauge field A_0, and the quantity μ_{su} are meaningless: explicit time dependence and the chemical potential may be absorbed into an overall shift in A_0; only grouped into $\tilde{\omega}$ do they take on a gauge-invariant meaning. An analogous statement may be made about k and A_z. In the

static solution we are looking for we may assume that the gauge fields are time independent. Then, in Coulomb gauge and with the ansätze in (3.18), (3.20) and (3.22), the gauge field equations of motion (3.5) reduce to

$$\nabla^2\tilde{\omega} = \tilde{\omega} m_\gamma^2\, \theta(\delta - r) \quad \text{and} \quad \nabla^2\tilde{k} = \tilde{k} v^2 m_\gamma^2\, \theta(\delta - r), \tag{3.24}$$

where

$$m_\gamma^2 = f^2 e^2 \sin^2\left(\left|\mathrm{K}^+\right| \sqrt{2}/f\right) \tag{3.25}$$

is the mass of the photon inside the vortex core (outside of the vortex core the photon is massless). We also see that the photon mass has a maximal possible value fe, which is an effect that is missed in the linearized theory. The charge and current densities may be read off directly from the right side of these equations.

The electromagnetic field equations of motion, by gauge invariance, are homogeneous equations of $\tilde{\omega}$ and $\tilde{k}$ respectively. In contrast, when electromagnetism is sourced by spin-half fermions, the equations of motion are not homogeneous—the electric charge is proportional to the fermion number alone. Instead, we find that a nonzero K^+ field only carries charge if the gauge field is nonzero. This implies that if the charge density vanishes at the wire's core there cannot be electric charge anywhere. This is apparent in the explicit solutions to (3.24). An analogous statement holds for current density.

This situation is very peculiar, and stands in contrast to typical electrostatic or magnetostatic problems, where we can set up a charge or current and ask about the fields. Instead we need to solve the gauge equations of motion, and *only then* do we know what the charge distribution is!

Luckily, we can solve these exactly. The solutions are

$$\tilde{\omega}(r) = \begin{cases} \tilde{\omega}_0 \ I_0(m_\gamma r) & r < \delta \\ \tilde{\omega}_0 \ \left(I_0(m_\gamma \delta) + m_\gamma \delta I_1(m_\gamma \delta) \log\left(\frac{r}{\delta}\right)\right) & r > \delta \end{cases} \tag{3.26}$$

$$\tilde{k}(r) = \begin{cases} \tilde{k}_0 \ I_0(v m_\gamma r) & r < \delta \\ \tilde{k}_0 \ \left(I_0(v m_\gamma \delta) + v m_\gamma \delta I_1(v m_\gamma \delta) \log\left(\frac{r}{\delta}\right)\right) & r > \delta \end{cases} \tag{3.27}$$

where I_0 and I_1 are the 0^{th} and 1^{st} modified Bessel function and $\tilde{\omega}_0 \equiv \tilde{\omega}(r=0)$ and $\tilde{k}_0 \equiv \tilde{k}(r=0)$. The values of $\tilde{\omega}_0$ and $\tilde{k}_0$ determine the charge per unit length and total current flowing through the vortex core. In fact, we can relate $\tilde{\omega}_0$ and $\tilde{k}_0$ to the charge per unit length $\mathcal{Q}^\perp$ and the total current I via Gauss' and Ampere's law respectively. One finds

$$\mathcal{Q}^\perp = +\frac{2\pi}{e}\tilde{\omega}_0 \ m_\gamma \delta I_1(\ m_\gamma \delta) = \ \ \tilde{\omega}_0 \ m_\gamma \delta f_1(m_\gamma \delta), \tag{3.28}$$

$$I \ \ = -\frac{2\pi}{e}\tilde{k}_0 v m_\gamma \delta I_1(v m_\gamma \delta) = -\tilde{k}_0 v m_\gamma \delta f_1(v m_\gamma \delta) \tag{3.29}$$

The apparent difference in sign between the charge and current is due to the difference in sign of the gauge fields when defining $\tilde{\omega}$ and $\tilde{k}$.

We show the dimensionless function f_1 in (3.28) and (3.29), but as other dimensionless functions arise, we will not give their explicit expressions. However, they are collected for convenience in Appendix A.

We can now compute the Lagrangian per unit length $\mathcal{L}^\perp$ of such a superconducting vortex. We use an infrared cutoff equal to the radius of the inner toroidal region to compute

$$\mathcal{L}^\perp = \int_0^R d^2 r_\perp \ \mathcal{L}_{\text{eff}} = \tilde{\omega}_0^2 m_\gamma \delta f_3(m_\gamma \delta) - \tilde{k}_0^2 v m_\gamma \delta f_3(v m_\gamma \delta) + f_4 + A f_5.$$

The dependence of $\mathcal{L}^\perp$ on K^+ is hidden inside the photon mass, and the K^0 gradients are inside f_4. The quantity $\mathcal{L}^\perp$ is a function of the variables $\{\left|\mathrm{K}^+\right|, \delta, R, \tilde{\omega}_0, \tilde{k}_0\}$.

Extremizing $\mathcal{L}^\perp$ would yield a variational approximation to the equations of motion for an infinite superconducting vortex. There are two qualitatively different solutions: either the vortex is superconducting, and $\sin(\sqrt{2}\left|\mathrm{K}^+\right|/f) \neq 0$ or the K^+ condensate is quenched and $\sin(\sqrt{2}\left|\mathrm{K}^+\right|/f)$ vanishes. The first breaks the $\mathrm{U}(1)_Q$ symmetry and the photon gets a mass, as described; the second does not. Due to the compact nature of the fields, there are two quenched solutions: $\sqrt{2}\left|\mathrm{K}^+\right|/f$ vanishes or is π. The first corresponds to $\Sigma = \mathbb{1}$ and is the quenched solution one finds with a linearized theory, the second corresponds to $\Sigma = \mathrm{diag}(-1, 1, -1)$. In both cases, Σ is diagonal and thus commutes with $\mathbb{Q}$, so from (3.5) it is easy to see that the photon mass must vanish. Despite the presence of this unusual solution, the familiar behavior of current and charge on the value of the condensate remains: a larger charge per unit length tends to push the condensate toward $\pm\frac{\pi}{2}$, a larger current tends to push the condensate toward the nearest quenched solution.

If we were primarily concerned with straight vortices, we could get the equations of motion for $\left|\mathrm{K}^+\right|$ and eliminate $\tilde{\omega}_0$ and $\tilde{k}_0$ in favor of $\mathcal{Q}^\perp$ and I (or equivalently, the linear momentum per unit length), which are fixed for such objects. However, for a circular loop whose radius R can change, the total current is not fixed, so to use this calculation of $\mathcal{L}^\perp$ to inform us about vortons, we need to compute the rest of the contributions to $\mathcal{F}^\perp$.

The charge per unit length was already computed when we solved the equations of motion for the gauge field, and is given in (3.28). The angular momentum per

unit length requires additional calculation. The total momentum density for the field configuration is

$$T^{0i} = \frac{f^2}{4}\,\mathrm{tr}\left[vD^i\Sigma^\dagger\cdot\nabla^0\Sigma + \text{ h.c.}\right] + (\mathbf{E}\times\mathbf{B})^i\,. \tag{3.30}$$

We are interested in the momentum that flows along the vortex. With our ansätze, we find

$$T^{0z} = \tilde{\omega}_0\tilde{k}_0 v f^2 \sin^2\left(\frac{|\mathrm{K}^+|\sqrt{2}}{f}\right)\times\begin{cases}(I_0(m_\gamma r)I_0(m_\gamma v r) + I_1(m_\gamma r)I_1(m_\gamma v r)) & r<\delta\\ \frac{\delta^2}{r^2}I_1(m_\gamma\delta)I_1(m_\gamma v\delta) & r>\delta,\end{cases} \tag{3.31}$$

The contribution from outside of the vortex is provided entirely by the electromagnetic Poynting vector. The total angular momentum per unit length is given by

$$\begin{aligned}\mathcal{J}^\perp &= \int_0^R d^2r_\perp\,\sqrt{R^2+r_\perp^2+2Rr_\perp\cos\phi}\;T^{0z}\\ &\approx \int_0^R d^2r_\perp\;R\;T^{0z} = Rm_\gamma\delta\tilde{k}_0\tilde{\omega}_0 f_2,\end{aligned} \tag{3.32}$$

where we have inserted the lever-arm from the vorton's center to the vortex's center, R, to approximate the angular momentum per unit length. Corrections due to different portions of the vortex being different distances from the vorton's center are negligible in the limit $R \gg \delta$. One may worry about whether this simplification significantly changes the angular momentum; numerical verification allays this fear—one way to understand this is that the angular momentum density falls off like r^{-2} and so very little is carried near the edges of the torus.

Through the results in (3.28), (3.30), and (3.32) we have completely specified $\mathcal{F}^\perp$. We now compute $F_{r>2R}$.

3.2.2 Far Fields

In the region far from the vorton (outside of the sphere of radius $2R$), the main contribution to F and the conserved quantities comes from the electromagnetic fields.

For simplicity, we will approximate the fields in this region by the leading pieces of their multipole expansions. Since the vorton can carry charge, we will keep the electric monopole term; since it can carry current, we will keep the magnetic dipole term. The fields are

$$\mathbf{E}_{out} = \frac{Q}{4\pi r^2}\widehat{\mathbf{r}} \tag{3.33}$$

$$\mathbf{B}_{out} = \frac{1}{4\pi r^3}\left(3(\mathbf{m}\cdot\widehat{\mathbf{r}})\widehat{\mathbf{r}} - \mathbf{m}\right) \tag{3.34}$$

$Q = 2\pi R\mathcal{Q}_\perp$ is the total vorton charge, and $\mathbf{m} = \pi R^2\ I\ \widehat{\mathbf{z}}$ is the magnetic moment of the vorton, assuming it lies in the xy-plane.

Their contribution to the total Lagrangian outside of the sphere is

$$\begin{aligned} L_{out} &= \int_{r>2R} \mathrm{d}^3 r\ \mathcal{L}_{eff} = \int_{r>2R} \mathrm{d}^3 r\ \frac{\mathbf{E}_{out}^2 - \mathbf{B}_{out}^2}{2} = \frac{1}{2}\int_{2R}^{\infty} \mathrm{d}r\ r^2\ \mathrm{d}\Omega\ \left(\mathbf{E}_{out}^2 - \mathbf{B}_{out}^2\right) \\ &= \frac{Q^2}{16\pi R} - \frac{m^2}{96\pi R^3} = (2\pi R\ \delta m_\gamma)\left(\tilde{\omega}_0^2\ f_7 - v\tilde{k}_0^2\ f_8\right). \end{aligned} \tag{3.35}$$

Further contributions from multipole terms will be down by at least factors of 4, which correspond to the factor of 2 in front of the cutoff $r_{min} = 2R$ as well as geometrical factors. These contributions will change the dimensionless numbers in f_7 and f_8 but will not change the qualitative dependence.

If we are to numerically minimize F with respect to our variational parameters, the sign difference between the electric and magnetic contributions will pose a problem. This sign difference will resolve itself when we eliminate the Lagrange

multipliers, and both contributions will enter F with the same sign.

The static electromagnetic fields also carry angular momentum, as the Poynting vector curls around the vorton's axis of symmetry. This angular momentum is

$$J_{out} = \int_{r>2R} \mathrm{d}^3 r \ \mathbf{r} \times \mathbf{S} = \int_{2R}^{\infty} r^2 \mathrm{d}r \ \mathrm{d}\Omega \ \mathbf{r} \times \left(-\frac{Qm \sin\theta}{(4\pi)^2 r^5} \widehat{\phi} \right) = \frac{Q\mathbf{m}}{12\pi R}$$
$$= (2\pi R) R m_\gamma \delta \tilde{k}_0 \tilde{\omega}_0 \ f_6, \tag{3.36}$$

which is arranged to be easily added to the contribution to the angular momentum from $2\pi R \mathcal{J}_\perp$. This completes the calculation of $F_{r>2R}$.

3.2.3 Stability

Having computed all contributions to F, we gather the results from (3.28), (3.30), (3.32), (3.35) and (3.36). Substituting these into (3.16) via (3.17), we find

$$F = \nu \left(2\pi R \tilde{\omega}_0 m_\gamma \delta f_1(m_{\gamma\delta})\right) + \Omega(2\pi R^2 m_\gamma \delta \tilde{k}_0 \tilde{\omega}_0)(f_2 + f_6) - 2\pi R \left(f_4 + A f_5\right)$$
$$- 2\pi R \delta m_\gamma \tilde{\omega}_0^2 \left(f_3(m_\gamma \delta) + f_7\right) + 2\pi R \delta m_\gamma v \tilde{k}_0^2 \left(f_3(v m_\gamma \delta) + f_8\right) \tag{3.37}$$

We now eliminate the Lagrange multipliers by minimizing F with respect to $\tilde{\omega}_0$ and $\tilde{k}_0$. These minimizations yield

$$\Omega = -\frac{2\tilde{k}_0 v}{\tilde{\omega}_0 R} \frac{f_3(v m_\gamma \delta) + f_8}{f_2 + f_6} \tag{3.38}$$
$$\nu = 2\tilde{\omega}_0 \left(\frac{f_3(m_\gamma \delta) + f_7}{f_1} + \frac{\tilde{k}_0^2 v}{\tilde{\omega}_0^2} \frac{f_3(v m_\gamma \delta) + f_8}{f_1} \right) \tag{3.39}$$

which we can plug back into (3.37) so that

$$F = \ 2\pi R m_\gamma \delta \left[\tilde{\omega}^2 \left(f_3(m_\gamma \delta) + f_7\right) + \tilde{k}^2 \left(f_3(v m_\gamma \delta) + f_8\right) \right] - 2\pi R \left(f_4 + A f_5\right). \tag{3.40}$$

Having eliminated the Lagrange multipliers from F, we can trade $\tilde{\omega}_0$ and $\tilde{k}_0$ for the conserved quantities. The quantities are given by

$$Q = 2\pi R\ \mathcal{Q}^{\perp} \qquad = 4\pi^2 R\tilde{\omega}_0 m_\gamma \delta I_1(m_\gamma \delta), \tag{3.41}$$

$$J = 2\pi R\ \mathcal{J}^{\perp} + J_{out} \qquad = 2\pi R^2 m_\gamma \delta \tilde{\omega}_0 \tilde{k}_0 (f_2 + f_6). \tag{3.42}$$

It is straightforward to eliminate $\tilde{\omega}_0$ in favor of Q and $\tilde{k}_0$ in favor of $J/\tilde{\omega}_0$.

Note that $\tilde{k}_0 \sim J/\tilde{\omega}_0 R^2 \sim J/QR$ so that the scaling of $\tilde{k}_0$ as R^{-1}, which in the ungauged case was used to argue for stabilization, is apparent. This is critically important, or vortons would not wind up with a stable equilibrium radius. Also note that whenever the angular momentum enters F, it will always be divided by Q, so that the angular momentum barrier is reduced for a vorton that carries a lot of charge. Making this trade for the conserved quantities gives

$$F = \frac{Q^2}{R}\frac{f_3(m_\gamma\delta) + f_7}{8\pi^3 \delta m_\gamma I_1(m_\gamma \delta)} + \frac{J^2}{Q^2 R}\frac{8\pi^3 \delta m_\gamma \left(f_3(v m_\gamma \delta) + f_8\right) I_1(m_\gamma \delta)}{(f_2 + f_6)^2} - 2\pi R(f_4 + A f_5). \tag{3.43}$$

We can see the explicit R dependence, and it follows the general pattern of (2.15). We know, therefore, that certainly there is a minimum R_0, and that the contributions to this quantity can indeed be thought of as separated into a tension and a barrier against collapse composed of electrostatic repulsion and an angular momentum barrier.

Eliminating $\tilde{\omega}_0$ and $\tilde{k}_0$ from F make it a function of $\{Q, J, w, \left|\mathrm{K}^+\right|, \delta, R\}$. Only one consideration remains: because of the way we artificially separated space into three regions and discarded the apple-core region, F has extra unphysical sensitivity to R: if we compute F when there is no vorton (ie. Q, J, w, $\left|\mathrm{K}^+\right|$, and δ all vanish)

it still depends on R. We therefore subtract this artifact off and understand that what me mean by F hereafter is this repaired quantity that gives no preference to any R when there is no vorton at all.

For any given fixed "atomic number" $Z = Q/e$ and J (and $w = 1$), we minimize F numerically with respect to $\left|\mathrm{K}^+\right|$, R and δ simultaneously. It is a good sanity check to take this F and taking the limit $e \to 0$, so that electromagnetism is totally removed, to see if we schematically recover a familiar expression or if anything goes wrong. Because f_2, f_3, f_6, f_7, and f_8 all are proportional to e^{-2}, nothing goes wrong as long as we think of Z as being a real physical quantity—the number of condensed particles.

3.2.4 Realistic Numbers

To get a feel for CFL+K^0 vortons we should plug in some realistic quantities for the parameters that are vorton-independent, like k_F and Δ, and then explore different J and Z that have reasonable R_0/δ.

For specificity we pick a gap $\Delta = 66$ MeV and a chemical potential $\mu = 450$ MeV. However, a wide range of reasonable parameters which still have K^0 condensation have qualitatively similar results. We show the numerical results of such a minimization as a function of Z and J in Figure 3.2. In order to avoid drawing faulty conclusions, we do not plot anything if the resulting equilibrium radius is smaller than the string thickness. That is, if $R_0/\delta < 1$, that region is whited out in the plots.

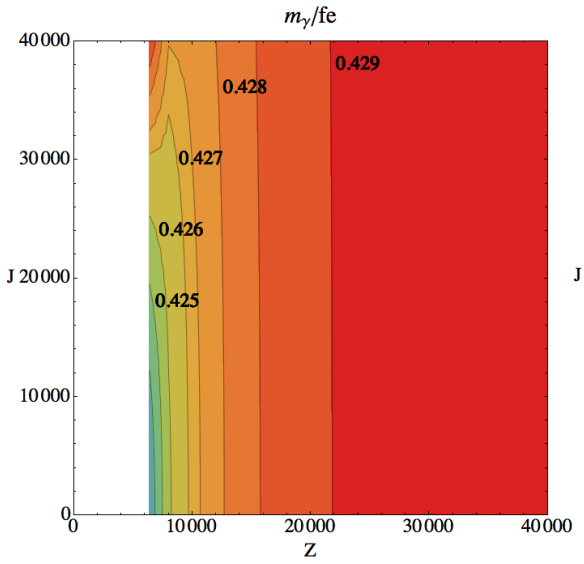

(a) Photon mass

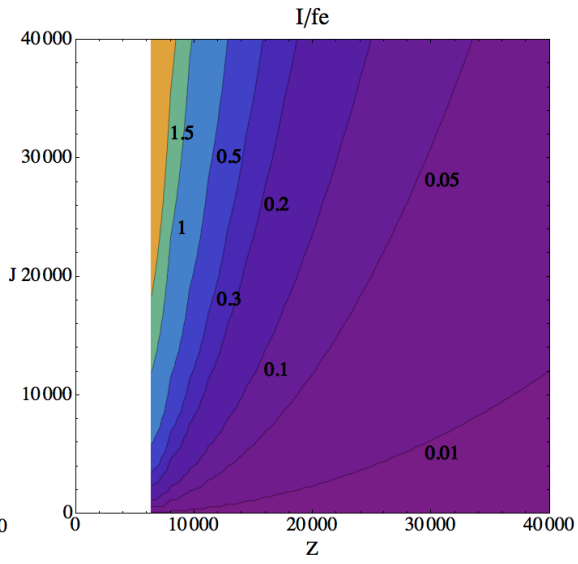

(b) Electromagnetic current

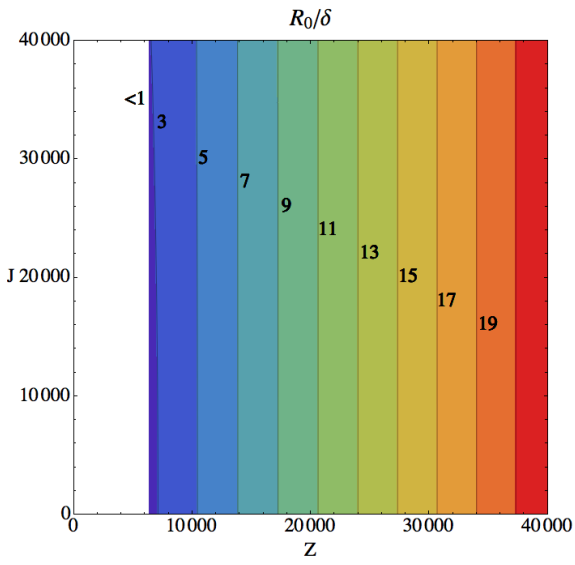

(c) Aspect ratio R_0/δ

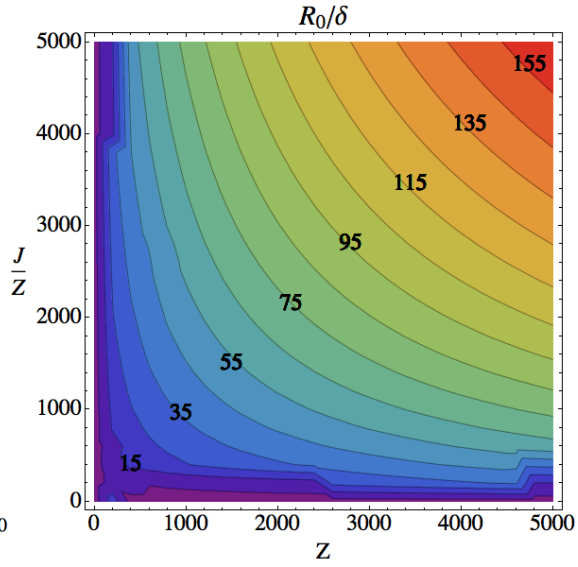

(d) Aspect ratio with rescaled J

Figure 3.2: Various equilibrium quantities as a function of Z and J for the EFT parameters $\Delta = 66$ MeV and $\mu = 450$ MeV. These figures are directly reproduced from Reference [1].

Figure 3.2a shows the condensate's slight variation in the region where $R/\delta > 1$: m_γ/fe changes from 0.428 only in the third decimal. Figure 3.2b shows the electrical current when the vorton is at its equilibrium radius. Figure 3.2c shows the aspect ratio R_0/δ of a vorton at equilibrium radius, the current I respectively, as functions of the parameters Z and J. We only plot $Z, J > 0$, since they always enter into F quadratically. We do not show the string thickness δ because its variation is also slight: for this choice of Δ and μ and the shown Z and J, δ varies between 25 and 29 fermi and its behavior adds no qualitative insight for the other graphs. The breakdown scale for the effective theory $1/\Delta \approx 4$ fm, is significantly smaller than the thickness of the core $\delta \approx 27$ fm, as suggested. This justifies the use of the EFT to describe these vortons.

We can verify that the current decreases with Q (and R) and increases with J. For a fixed Z, the current increases with angular momentum. For a fixed angular momentum, the current goes down with both the radius and the charge, so that in principle the scaling $I \sim R^{-1}$ is maintained, but with a Z-dependent coefficient.

In the first three figures, we see that these J affect the equilibrium radius only slightly, if at all. However, this is an artifact of the fact that $\tilde{k}_0 \sim J/QR$: at such large Qs, one needs a sizable J to overcome its suppression by Q keep any angular momentum barrier. That is, the effectiveness of the angular momentum depends on the per-unit-charge quantity and not the absolute quantity. The equilibrium radius is plotted with the J axis rescaled to be J/Z in Figure 3.2d for the same gap and chemical potential. In this rescaled view, one can more easily see sustaining effect of the angular momentum barrier.

From this choice of gap and chemical potential we learn a lesson which carries over to other parameter choices: to get a configuration where $R \gg \delta$ requires large (order 10^4 or larger) Z and J/Z. Moreover, even the largest vortons shown in Figure 3.2d have radii which are much smaller than the thickness of the possible domain wall mentioned at the end of Section 3.1.1, meaning it doesn't contribute significantly to F, providing an *a posteriori* justification of our ignoring the domain wall to begin with. The region where vortons are too small, which in the other figures was a region defined by a fixed Z, in this figure corresponds to a region defined by a hyperbola that is essentially too small to see.

3.2.5 Potential Improvements

Vortons for a specific choice of gap and density were characterized in Section 3.2.4 by a variational calculation that made a number of important approximations.

The first is the obvious issue of geometry—but as argued the gradients that become relevant when R_0 isn't much larger than δ should help make vortons larger. The second is that the step-function ansätze for the kaon fields in (3.22) is a dramatic oversimplification. This can be remedied with some simpler variational functions, but as argued in Section 2.2, the region where the two species overlap should quickly saturate in importance in the calculation of $\mathcal{F}^{\perp}$. While the expectation is that a better variational function should yield smaller vortons, this saturation should limit the size of this effect. Finally, we only considered the leading term in the

multipole expansion for the electromagnetic fields in the $r > 2R$ region. However, the higher multipoles should be small—the electric dipole is obviously zero, so in both electric and magnetic fields both corrections start at the quadrupole. Is there any approximation we made which, when removed, could dramatically shrink the size of the vortons we considered?

The answer is yes, and it is the subject of Section 3.3: we have assumed that vortons are electrically unshielded. That is, we assumed that one side of the vorton repels the other with the full Coulomb force while electrons (or positrons, depending on the sign of Z) should surround the vorton to maintain charge neutrality. We will see that while this is not a fatal correction to the assertion that vortons are supported by the CFL+K^0 phase, the same vorton charge and angular momentum will have a notably smaller aspect ratio.

3.3 Vortonium

In the previous section we discussed electromagnetically bare vortons. However, we found that for recognizably-toroidal vortons we needed large electric charges ($Z \sim 10^4$). In order for there to be a bulk filled with vortons, however, there cannot be an overall electric charge—the charge must be neutralized. We therefore must study the mechanism by which a charged vorton neutralizes its environment—electrons (or positrons, depending on the vorton's charge's sign). These electrons will not only shield the long-distance monopole field neutralizing the bulk, but will also get into the space within the vorton, shielding one side from the other. By this

mechanism we can see that if there are vortons, they are surrounded by an electron cloud, and we should really study the size of this vortonic "nucleus" surrounded by electrons—a system we name "vortonium".

To understand how to treat the electrons, we should get a grasp on roughly how dense they should be. One method for characterizing the behavior of a large number of electrons is the Thomas-Fermi approximation[55, 56]. In the typical non-relativistic Thomas-Fermi approximation, the radius of an atom is roughly $a_0/Z^{1/3}$, so that the electron number density should be roughly

$$\frac{Z \text{ electrons}}{\text{Volume} = (a_0/Z^{1/3})^3} = \frac{Z^2}{a_0^3}. \tag{3.44}$$

or an interparticle spacing of $a_0/Z^{2/3}$, which corresponds to a Fermi momentum of almost 200 MeV when $Z = 10^5$. Thus, the nonrelativistic approximation is totally inapplicable here; indeed, we should use the corresponding *ultra*relativistic approximation, and expect that it should be quite good.

In the previous section we strove to ensure that we had an qualitative analytical understanding of how the various variational parameters entered into the expression of F. If we wish to incorporate the shielding of electrons via the ultrarelativistic Thomas-Fermi approximation, this will no longer be possible. Faithful incorporation of the shielding requires that electrons get between the two sides of the vorton, meaning that the artificial separation of the geometry discussed in Section 3.2 into the far region $r > 2R$, the apple-core region, and the torus needs to be reconsidered. Keeping these divisions as they are presents a problem: the electromagnetic effects in all three regions may be dramatically modified and are certain to be related.

Instead, we will consider a different geometric division but for simplicity and to be able to reuse as much of the results from the previous work as possible, we will only alter the geometric separation for the electric fields. For the electric fields, we will consider the torus of radius R and thickness δ (instead of thickness R). That is, we will minimize

$$F_{\text{vortonium}} = F_{\text{vorton}} - F_{\text{far } E} - F_{\text{near } E} + F_{\text{TF}} \tag{3.45}$$

where F_{vorton} is the repaired quantity described below (3.43), $F_{\text{far } E}$ is electric contribution in the $r > 2R$ region, $F_{\text{near } E}$ the electric contribution between the torus of thickness δ and the torus of thickness R, and F_{TF} is the contribution which we will find numerically by solving the ultrarelativistic Thomas-Fermi equations for a toroidal charge of radius R, thickness δ, and charge eZ.

We will not recompute the electromagnetic contributions to the angular momentum or other electric-field-dependent quantities, because this would add significant complication, to the extent that we would be better off starting from scratch and solving the problem with an entirely numeric approach.

This is a totally uncontrolled approximation, but is obviously an improvement over the previous one and allows us to include the desired shielding effects.

Both $F_{\text{far } E}$ and $F_{\text{near } E}$ are easy to compute. The former is given by

$$F_{\text{far } E} = \int_{2R}^{\infty} \mathrm{d}^3 r \, \frac{1}{2} \left(\frac{Q}{4\pi r^2} \right)^2 = \frac{(eZ)^2}{16\pi R} \tag{3.46}$$

and the latter by

$$F_{\text{near } E} = 2\pi R \int_{\delta}^{R} \mathrm{d}^2 r_{\perp} \, \frac{1}{2} \left(\frac{\lambda}{2\pi r} \right)^2 = \frac{(eZ)^2}{8\pi R} \log\left(\frac{R}{\delta} \right). \tag{3.47}$$

We now must compute F_{TF}.

3.3.1 Shielding by Electrons

The Thomas-Fermi approximation formalizes the idea that we can treat the local number density of electrons n instead of each electron individually by letting

$$n = \frac{1}{3\pi^2} k_{\mathrm{F}}^3 \tag{3.48}$$

where k_{F} is the Fermi momentum. Gauss' law

$$\nabla^2 \varphi = en \tag{3.49}$$

allows us to compute the electric potential given a distribution of electrons with local density n.

Finally, the requirement that the system is in equilibrium enforces the fact that we should not be able to save any energy by moving an electron from one point to another. That is, the equilibrium condition is

$$d\left(k_{\mathrm{F}} - e\varphi\right) = 0 \tag{3.50}$$

where we have approximated the energy $\sqrt{k^2 + m^2} \approx k_{\mathrm{F}}$, the ultrarelativistic approximation. This is equivalent to saying that k_{F} and $e\varphi$ differ only by a constant:

$$k_{\mathrm{F}} - e\varphi = -e\varphi_\infty \tag{3.51}$$

where φ_∞ is the electric potential infinitely far away.

We can combine these three equations and eliminate n and k_{F} in favor of φ only,

$$\nabla^2 \varphi = \frac{16}{3} \alpha^2 \left(\varphi - \varphi_\infty\right)^3 . \tag{3.52}$$

This equation appears more complex than it truly is: because φ_∞ is a constant, $\nabla^2\varphi_\infty$ is zero and may be subtracted from the left-hand-side to yield an equation homogeneous in $(\varphi - \varphi_\infty)$. We can then absorb φ_∞ into φ as a very simple change of variables. Alternatively, we could have set φ_∞ to zero at the start, which amounts to a partial choice of gauge. Either way, the equation we actually need to solve is not (3.52) but the simpler

$$\nabla^2\varphi = \frac{16}{3}\alpha^2\varphi^3, \tag{3.53}$$

the ultrarelativistic Thomas-Fermi equation.

Solving (3.53) would provide us with a complete, self-consistent description of the electric potential under the assumptions described above, in the sense that the potential both directs electrons to their equilibrium positions and accounts for the electrons being in those positions to begin with. It does leave out some features of a first-principles solution: electron interaction energy (which was assumed to be negligible in (3.48)) and density gradients. Both of these effects are small compared to the Fermi momentum at these large densities, so we should not be concerned that they will make a noticeable difference. Equation (3.53) also describes the crusts of strange stars and quark-nugget models of dark matter[57, 58, 59, 60, 61]. In these situations though, the sources providing the attractive electrical field are either very large, and thus can be considered locally flat, or are quite small and can be considered spherical; our situation necessitates toroidal geometry.

Perhaps unsurprisingly, the toroidal nature of the problem is particularly well adapted to toroidal coordinates, which are reviewed in Appendix B. In this orthog-

onal system, the axial coordinate and the coordinate u are both naturally compact, but the coordinate v, which characterizes how close a point is to the reference circle, is not: it runs over the interval $[0, \infty)$. In order to solve (3.53) numerically, we must therefore cut v off.

As v gets larger, one gets closer to the reference circle, so it is natural to cut v off in such a way that implements the artificial separation of space we already discussed—separating the superconducting torus of radius R and thickness δ where $\left|\mathrm{K}^{+}\right|$ is condensed and the insulating region at

$$v_{\max} = \operatorname{arcsinh} \sqrt{\left(\frac{R}{\delta}\right)^2 - 1} \tag{3.54}$$

in a toroidal system with a reference circle of radius

$$a = \sqrt{R^2 - \delta^2}. \tag{3.55}$$

This artificial cutoff physically excludes electrons from the condensed region, and thus creates a pressure that shrinks δ. Numerically we find that these changes are roughly 10% and thus ignoring them are good enough for our purposes here.

This gives us a finite region in toroidal coordinates in which we need to solve (3.53) numerically. In order to get a nontrivial solution (ie. $\varphi \neq 0$), we must specify the boundary conditions. Intimately connected with the boundary conditions are issues of symmetry.

We can use the axial symmetry to enforce independence of the solution on the axial coordinate, reducing the problem by a dimension. We henceforth suppress all discussion of the axial coordinate. The physical problem is also symmetric across the xy-plane, which allows us to study only the region $z > 0$. The fact that the

solution is symmetric under reflections across the xy-plane and that it should be smooth gives the boundary conditions

$$\partial_u \varphi \Big|_{u=0} = 0 \quad \text{and} \quad \partial_u \varphi \Big|_{u=\pi} = 0 \tag{3.56}$$

while the fact that we expect no cusps along the z-axis from axial symmetry leads us to the boundary condition

$$\partial_v \varphi \Big|_{v=0} = 0. \tag{3.57}$$

With only these three conditions the solutions will automatically fulfill the requirements of these symmetries.

The fourth boundary of the uv-grid is at $v_{\max}$, where we require the electric field to be that of a wire with circular cross section $\pi\delta^2$ and linear charge density $Ze/2\pi R$. This amounts to enforcing

$$\partial_v \varphi \Big|_{v=v_{\max}} = 2\left(\frac{Ze}{2\pi R}\right) \coth v_{\max}. \tag{3.58}$$

All four boundary conditions for the electric potential φ are Neumann conditions, as expected by gauge symmetry. In order to help the numerical procedure converge we also pick a gauge,

$$\varphi\,(u = 0, v = 0) = \varphi_\infty = 0. \tag{3.59}$$

These conditions all together pose a totally well-formed mathematical question. However, we have not enforced an important physical motivation for considering the effect of electrons in the first place—overall charge neutrality! How does the solution to this equation with only those boundary conditions know that there

should be enough electrons in the system in order to kill the monopole field? It is not obvious that this neutrality condition has been implemented.

Surprisingly, toroidal coordinates implement this condition automatically. It is easy to show that the radial spherical coordinate is given by

$$r^2 = a^2 \frac{\cosh v + \cos u}{\cosh v - \cos u} \tag{3.60}$$

so that large r^2 corresponds to small $u^2 + v^2$, so that the sphere $r = \infty$ corresponds to the point $(u, v) = (0, 0)$.

The multipole expansion for the electric potential is

$$\varphi(\mathbf{r}) = \varphi_\infty - \frac{Q_{total}}{4\pi} \frac{1}{r} - \frac{\mathbf{d} \cdot \widehat{\mathbf{r}}}{4\pi} \frac{1}{r^2} + \cdots \tag{3.61}$$

which translates into toroidal coordinates simply

$$\varphi(u, v) = \varphi_\infty - \frac{Q_{\text{total}}}{4\pi} \frac{\sqrt{u^2 + v^2}}{2a} - \frac{\mathbf{d} \cdot \widehat{\mathbf{r}}}{4\pi} \frac{u^2 + v^2}{4a^2} + \cdots . \tag{3.62}$$

when r is large and the arrangement of charges can be totally encapsulated by a net charge Q_{total} and a dipole moment $\mathbf{d}$. The dipole moment $\mathbf{d}$ must vanish by parity and axial symmetries, while the quadrupole will be nonzero.

Because we have already demanded the solution obey the boundary conditions $\partial_u \varphi\,(u = 0, v) = 0$ and $\partial_v \varphi\,(u, v = 0) = 0$, we have guaranteed that infinitely far away at the point $(u, v) = (0, 0)$ the potential φ is flat in both directions—precisely what we need to ensure that the total charge vanishes! That is, charge neutrality is accidentally implemented by the other symmetry conditions in these coordinates. This is a happy surprise, and makes attaining charge-neutral combinations of vortons and electrons easier than one might otherwise expect.

Because the physical system of interest has a number of additional scales (R, δ) compared to the typical spherical situation (where one only has Z and m_e), there is no simple rescaling we can perform to get a universal-up-to-rescaling solution that solves the Thomas-Fermi equation. There is a rescaling that can reduce the number of independent variables from 3 (Z, R, and δ) to 2, but for clarity it is simpler to simply think of fixing all three separately. Therefore, for each Z we will numerically solve (3.53) for a large number of radii and string thicknesses, and use the solution to compute F_{TF}.

To solve (3.53) we imagine a fictitious time dimension t and any starting field configuration $\varphi(t=0)$ and evolve it according to

$$\nabla^2\varphi - \frac{16}{3}\alpha^2\varphi^3 = \frac{\operatorname{csch} v}{(r^2-\delta^2)^{3/2}}\frac{d\varphi}{dt} \tag{3.63}$$

so that as $\varphi(t)$ reaches a temporal fixed point it solves the Thomas-Fermi equation. The coefficient in front of the time derivative is chosen to reduce some numerical instabilities.

To generate numerical solutions we first pick Z, R, and δ, so that we can calculate $v_{\max}$ and the boundary condition there. We then discretize the coordinates u and v onto a 32×32 grid and start with a simple interpolated polynomial that satisfies the boundary conditions at the wire that we evolve forward in fictitious

time. We iterated this procedure for

$$
\begin{aligned}
R &\in \{80,\ 100,\ 120,\ 140,\ \cdots 800\}\ \text{fm} \\
Z &\in \{250,\ 500,\ 750\} \cup \{1250,\ 2500,\ 3750,\ 5000,\ \cdots 50000\} \\
\delta &\in \{1,\ 2,\ 3,\ 4, \cdots 35\}\ \text{fm}.
\end{aligned}
\tag{3.64}
$$

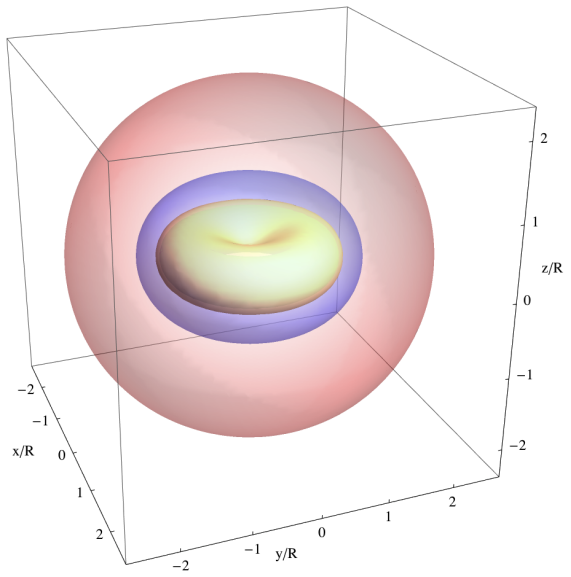

Figure 3.3: The three kinds of equipotentials—toruses (green), biconcave disks (orange), and oblate spheres (blue and red). Figure reproduced from Reference [2].

The resulting electric potentials are easy to understand qualitatively, and typical solution has three kinds of equipotentials, as shown in Figure 3.3. Very close to the wire, the equipotentials are toruses. Farther away, they are biconcave disks—they look more like a bialy or red blood cell. Farther yet they look like oblate spheres, and extremely far away those spheres lose their oblateness and become rounder and rounder.

Having propounded on the importance and accidental ease of producing solutions which produce objects that are overall charge-neutral, we can check the numerical procedure by calculating the number of electrons from the electric potential and comparing it to charge of the vorton. The number of electrons is given by

$$\int_{\text{outside}} 2\pi \, \mathrm{d}A \, \nabla^2 \varphi(u, v) \tag{3.65}$$

where the 2π comes from the axial integration and the area differential and gradient live in the uv-plane. We performed this check for all of the calculated gauge configurations. The number of electrons matched the vortonic charge Z (modulo a sign) to within 1.8% every time; only 2% of the examples differed by more than 1%; only 25% by more than 0.5%. We verified that for a handful of specific examples, the results of this check can be improved by using a finer grid.

Using the generated electric potentials we can compute the corresponding contribution to F. The gauge field contributes

$$F_{\text{TF}}\left(Z, R, \delta\right) = \int 2\pi \, \mathrm{d}A \, \frac{1}{2} \left(-\nabla\varphi\right)^2 . \tag{3.66}$$

Note that the total F will depend on K^+ but also on the parameters of the EFT, μ, Δ, and $\mathbb{M}$, and must be recalculated if those parameters change, while F_{TF} is independent of these choices and so may be calculated once for all choices and reused over and over again. With F_{TF} evaluated at the points given by (3.64) we can make an interpolating function that works anywhere in the range defined by the extremes of those variable ranges.

3.3.2 Results

With this interpolating function of F_{TF} we can simply minimize $F_{\text{vortonium}}$ given in (3.45). For ease of comparison with the unshielded vortons discussed in Section 3.2, we pick the same EFT parameters $\Delta = 66$ MeV and $\mu = 450$ MeV. The results of this minimization are shown in Figure 3.4.

It is clear from Figure 3.4a that the condensate again saturates at roughly half its possible maximum, slightly increased from the unshielded case. In Figure 3.4b we see that now the string thickness varies much more than in the unshielded case: in the plotted region it changes by a factor of two, whereas in the unshielded case it changed by only 4 fermi across the whole plotted range.

Comparing Figure 3.2c to Figure 3.4c, it is apparent that the electric shielding makes a major difference in the aspect ratio R_0/δ. This change results both from the changing string thickness and the changing radius R_0. Not only are the vortons smaller, but they also grow more slowly as a function of Z.

This slower growth is expected, as illustrated by a simple argument. At leading order, the electrons should simply cancel the electromagnetic effects entirely. This would give a charge-independent radius. However, the cancellation is made imperfect by Pauli blocking—the electrons cannot all go and sit exactly where they are needed. Thus, there should be some remnant electromagnetic effects that makes the vorton get bigger with Z. However, as its radius gets bigger, more electrons can shield it effectively, meaning that it will grow more slowly than one might otherwise expect.

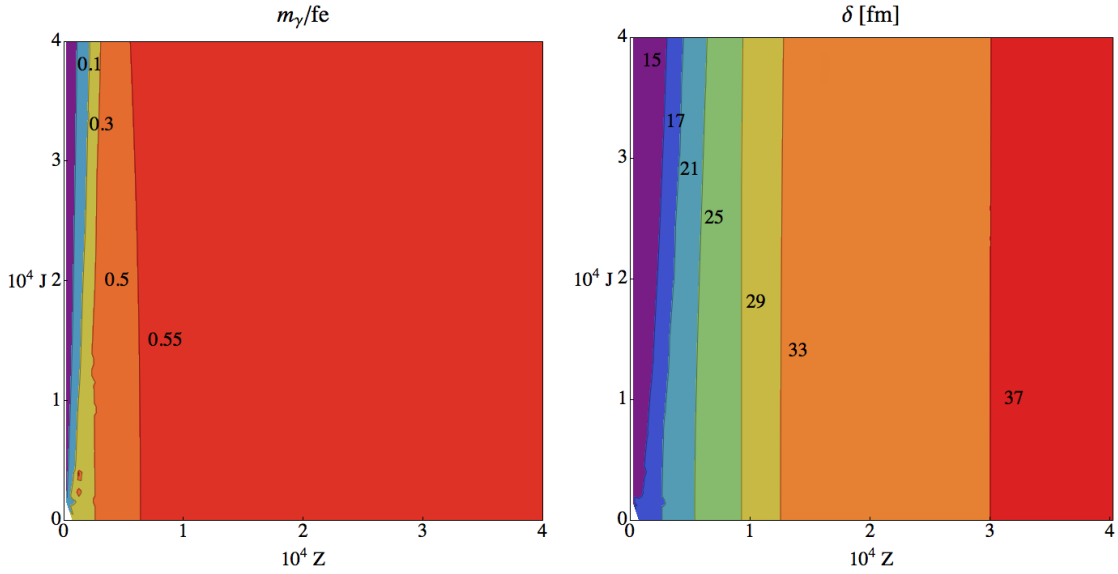

(a) Photon mass

(b) String thickness

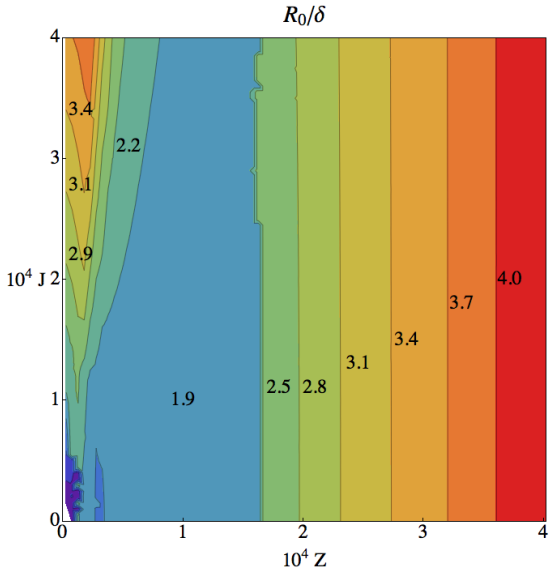

(c) Aspect ratio R_0/δ

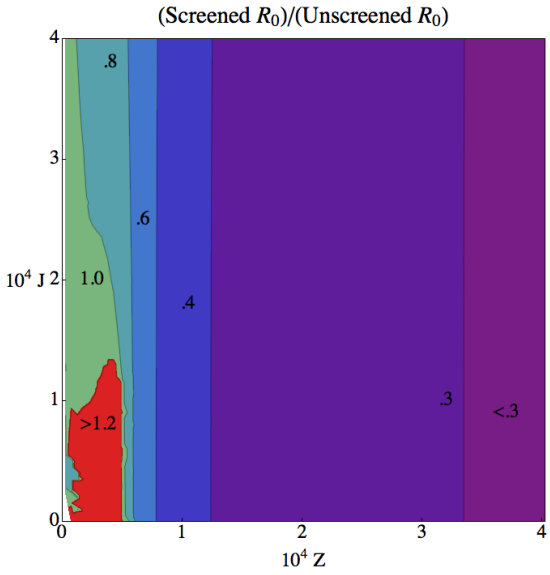

(d) Vortonium vs. vorton radius

Figure 3.4: Various equilibrium quantities as a function of Z and J for the EFT parameters as in Fig. 3.2. All but Fig. 3.4b are directly reproduced from Reference [2].

The shielded equilibrium radius is compared to the unshielded equilibrium radius in Figure 3.4d. It is interesting that in the region of small Z and small J there is a region where shielded vortons are actually *larger* than unshielded vortons. This peculiar effect might be interpreted as the electron degeneracy helping keep the vorton open, picking up the slack of the shielded far-field electrostatic terms. However, it is important to note that in this region the aspect ratio of the shielded vortons is relatively small. Moreover, if the degeneracy pressure is large enough to accomplish this feat, it seems reasonable to expect that the fictitious pressure created by excluding the electrons from the vorton core could be non-negligible.

In order to verify whether this is an artifact of our uncontrolled approximation or a true physical effect, a fully numerical calculation of F is required—leaving φ, K^+, and K^0 all dynamical. The complication of simultaneously solving the Thomas-Fermi equation (3.53) and all of the equations of motion is far beyond the scope of this work. With such a framework for solving these equations all at once it would be easy to incorporate fully three-dimensional geometry, magnetic and curvature effects, and the circulation of K^0 around and through the vorton as well.

3.4 Summary and Possible Future Directions

In this chapter we have discussed the vortons supported by the CFL+K^0 phase of dense quark matter. Gauging and charge play extremely important roles in the dynamics of these vortons, and add significant complication compared to the "warm-up" BEC vortons discussed in Chapter 2. In particular, shielding of electrons makes

a dramatic difference and must be incorporated into the description of these charged vortons, these two things making up vortonium.

There are many directions one might pursue with regards to these objects. One was discussed at the end of Section 3.3.2: a fully numerical formulation of the problem would give accurate mean-field field profiles and would skirt a variety of problems introduced by attempting to keep some of the calculation analytic.

It is easy to imagine that if there are many vortons in the CFL+K^0 bulk, they might radically alter the phase's transport properties. To understand how these change one needs to understand vortonium-vortonium interactions. One might also imagine all sorts of vortonic "chemistry"; in this high-density environment, one might be able to study the Periodic Table out to atomic numbers beyond 10^4.

Perhaps the most pressing concern should be trying to develop an estimate of how many vortons there are in the first place. If in a neutron-star-core sized volume there are but a few vortons, they will almost certainly have no observable consequences. In order to understand if pursuing the other lines of inquiry are worthwhile, we need a very rough estimate. This is a difficult proposition, because the Kibble-Zurek mechanism described in Section 2.4.1 is a dynamical process that requires fast thermal quenching, and it is unclear if the timescales on which neutron stars cool will be good enough to lock topological properties into the condensates; as the other production mechanism required an experimenter, it seems unlikely that it will be applicable in the CFL+K^0 context.

Part 2

Nuclear Condensation in Helium White Dwarfs

Introduction

There is a large separation of scales between typical atomic phenomena, which have a natural length scale of the Bohr radius $a_0 \sim .5\text{Å} = 5 \cdot 10^{-11}\text{m}$, and typical nuclear phenomena, which occur on the QCD confinement scale 1fm$= 10^{-15}$m. Theorists who study matter at Bohr-radius inter-nucleus spacings are primarily considered atomic or condensed matter physicists (or even chemists), and typically post in the `physics.atom-ph` or `cond-mat` sections of the arXiv, while those who study phenomena with fermi-scale interparticle spacings are thought of as nuclear physicists and typically post in `nucl-th`. While this is simply a sociological observation, it is indicative of a vast, under-studied, density regime. It seems unlikely that at densities with interparticle spacings that lie in the four-and-a-half orders of magnitude between these two scales nothing interesting happens.

Moreover, there is plenty of room, so to speak, for densities where the typical inter-nucleus spacing is much greater than the size of the nucleus itself but much smaller than the Bohr radius. Such a regime not only has tremendous theoretical appeal but also has real-world applications in astrophysics and more down-to-Earth high-density conditions such as inertial confinement experiments or diamond anvil cells.

In this Part we will discuss the behavior of helium atoms compressed to densities where the average inter-nucleus spacing ℓ is smaller than the Bohr radius a_0. At these densities it is no longer possible to associate any particular electron with any particular nucleus; instead we must consider the helium nuclei to be a totally ionized plasma in an environment of degenerate electrons, where the nuclei and elec-

trons interact electromagnetically. These densities are expected to exist in the core of helium white dwarfs (HeWDs).

The zero-temperature ground state at such densities is expected to be a nuclear Coulomb crystal[62, 63, 64], where the nuclei themselves lock themselves into a lattice via mutual electromagnetic repulsion, while at high temperatures one expects a plasma. Typical models of HeWDs assume that this plasma cools and cools until it reaches the crystallization temperature and freezes (for one such example see Reference [65]).

It was recently noticed that if the density is high enough, this is not the correct phase transition sequence to go from hot plasma to cold lattice—instead the plasma cools until the helium nuclei condense and this condensate then cools until it freezes; this extra step may have observable consequences[66, 67, 68]. The density beyond which this intermediate condensed phase exists grows with the mass of the ions, as we will motivate with some simple scaling arguments in Chap. 4; carbon-oxygen white dwarfs do not get dense enough to trigger the condensation of carbon nuclei, but it is possible that helium white dwarfs may get dense enough to trigger the condensation of helium nuclei.

This phase is quite different from the other two expected phases—we will show that it has a previously-unnoticed gapless quasiparticle which, unlike plasmons, will not get Boltzmann-suppressed at low temperatures. This degree of freedom causes the specific heat to drop precipitously—where it might previously be dominated by the helium plasma, the condensed ions have a low enough specific heat that it is the degenerate electrons that dominate.

This extra phase may help explain a peculiarity in the observation of HeWDs recently pointed out in Reference [69]. In order to understand this peculiarity, it is helpful to know a little bit of background knowledge about white dwarfs.

White dwarfs are stars that have finished fusing but are not heavy enough to collapse and then explode as a supernova but instead are held up by their electron degeneracy pressure. Most white dwarfs are primarily made of carbon or oxygen, which are fusion-chain end products if the core temperature is not hot enough to burn oxygen into silicon. These white dwarfs are called carbon-oxygen white dwarfs (COWDs). Helium white dwarfs, on the other hand, result from stars that do not get hot enough to trigger the triple-alpha process that creates produces carbon-12.

Stars that are hotter burn their fuel faster and go through their life cycle more quickly, and heavier stars typically have hotter cores. Thus, the production rate of COWDs is much greater than that of HeWDs if we normalize against the number of stars that are destined to become each type, simply because a star that will be light enough to not burn helium will also burn more slowly. In fact, the amount of time it takes a single star to evolve into a HeWD via the normal white dwarf lifecycle is longer than the current age of the universe[70].

It has been known for more than 40 years, however, that HeWDs can evolve in binary partners[71, 72, 73, 74], and modern calculations can model HeWD generation in more extreme situations, such as partners to neutron stars[75] or with brown dwarf or heavy planetary partners[76]. A binary partner can pull off the hydrogen atmosphere of a heavy star that has already produced a lot of helium—if it pulls off enough hydrogen the helium core that remains will not have sufficient mass to

ignite fusion of helium into carbon, so that the star is bound to cool into a helium white dwarf. By this mechanism helium white dwarfs can be produced much faster than they would if they followed the same sequence a typical carbon-oxygen white dwarf does.

Because their evolution is relatively complicated and can only have happened, as of yet, in a binary pair, we expect very few HeWDs compared to the number of COWDs. However, Reference [69] gives a detailed population of the globular cluster NGC 6397, which is the second-closest such cluster to the sun, and shows that not only are there fewer HeWDs, but there are almost no very dim, cool HeWDs. That is, even though the Hubble Space Telescope sees many dim, cool carbon-oxygen white dwarfs above magnitude 24 in the R_{625} channel, it sees too few helium white dwarfs in that channel; indeed, it sees just a few that dim while many more were expected.

This puzzling dearth of HeWDs can be explained in a few ways. First, it may be that NGC 6397 happens to be a particularly HeWD-sparse globular cluster. Second, it may be that the production, and thus population, of HeWDs is not what is expected. These first two explanations are at their root astrophysical in nature. Finally, it may be the evolution of HeWDs is peculiar, and that once they get cool enough they suddenly and unexpectedly cool very quickly, so that the reason there are so few dim specimens is that the dim ones have cooled beyond the sensitivity of our telescopes. This would be an explanation from nuclear physics.

In this Part we will keep this third possibility in mind. Specifically, we will focus on whether the unusual phase of condensed nuclei might provide a cooling

mechanism, which would explain the difference between HeWDs and COWDs.

In Chapter 4 we will discuss the simple scaling arguments that suggest that such a condensed phase really exists at astrophysical densities for helium (but not carbon-oxygen) white dwarfs, while in Chapter 5 we will discuss the effective field theory (EFT) that characterizes this phase and investigate its spectrum, uncovering a previously-unknown gapless quasiparticle[77]. In Chapter 6 we will perform some simple calculations investigating the potential observational signatures of this phase. In particular, we will show that the specific heat of the condensed phase is much smaller than either the plasma or lattice phase that the condensed phase replaces at some temperatures, and that the annihilation of the new quasiparticles into neutrinos is only competitive with surface photoemission if the critical temperature at which the condensate vanishes is high enough. In Chapter 7, we will investigate the critical temperature and demonstrate that, barring a few caveats, it seems unlikely that the critical temperature is, in fact, high enough; the neutrino emission process is likely uncompetitive.

Chapter 4

Motivation

Reference [66] first pointed out, using very simple arguments, the possibility of helium nuclei condensing at astrophysical densities. Let us review these arguments here.

A good guide is that crystals melt when the typical thermal fluctuations are greater than the potential barrier that localizes the crystal sites. In the case of interest, at low temperature the helium nuclei are locked into place by their mutual Coulomb interaction. If we assume that the nearest-neighbor interaction dominates, then the potential energy E_C is of the size

$$E_C = \frac{Z^2\alpha}{\ell} \tag{4.1}$$

where the atomic number Z is 2 for helium, $\alpha \approx 1/137$ is the electromagnetic fine structure constant, and ℓ is the spacing between the helium nuclei. The interparticle spacing is related to the number density n by

$$n\left(\frac{4\pi}{3}\ell^3\right) = 1; \tag{4.2}$$

by charge neutrality we expect to find that the electron number density n_e to be Zn.

The thermal energy E_T in the plasma, on the other hand, can simply be estimated by the free Bose gas result,

$$E_T = T \tag{4.3}$$

where we have adopted units where Boltzmann's constant k_B is set to 1.

Combining (4.1) and (4.3) we can estimate the temperature at which the crystal melts from thermal fluctuations. We define the ratio Γ to be the ratio

$$\Gamma = \left.\frac{E_C}{E_T}\right|_{T=T_{\rm melt}} \tag{4.4}$$

when the crystal melts.

Monte Carlo techniques show that Γ is around 180. References [78, 79] found that the crystal melts when $\Gamma \approx 180$; Reference [80] found $\Gamma = 168 \pm 4$; Reference [81] that Γ is 178 for body-centered-cubic crystals and 192 for face-centered cubic crystals, respectively. Using $\Gamma = 180$, one can resolve (4.4) for $T_{\rm melt}$, to find

$$T_{\rm melt} = \frac{Z^2\alpha}{\Gamma a_0}\left(\frac{a_0}{\ell}\right) \approx \left(\frac{a_0}{\ell}\right)\ 1750\ Z^2\ {\rm K}, \tag{4.5}$$

which is $(a_0/\ell)\,7000{\rm K}$ for $Z = 2$. This is the temperature at which *were there no condensed phase* the nuclear crystal would melt into a plasma. Note that this temperature scales like ℓ^{-1}. We should compare this temperature to the temperature at which the helium nuclei condenses.

One way to estimate the condensation temperature is to compare the thermal de Broglie wavelength to the interparticle spacing. The thermal wavelength is

$$\lambda_{\rm T} = \sqrt{\frac{2\pi}{MT}} \tag{4.6}$$

where M is the ion mass; for ^{4}He $M \approx 3.7{\rm GeV}$. When the thermal wavelength is of the same scale as the interparticle spacing, one expects the wavefunctions of neighboring nuclei to overlap enough to behave coherently. Equating $\lambda_{\rm T}$ and ℓ gives

a condensation temperature

$$T_{\mathrm{C}} = \frac{2\pi}{M\ell^2}. \tag{4.7}$$

The primary lesson from this scaling argument is the dependence on the mass and interparticle spacing; the 2π is by far less certain. In fact, a free Bose gas condenses at[82]

$$T_{\mathrm{Bose}} = \left(\frac{3}{(4\pi\zeta\,(3/2))}\right)^{2/3} \frac{2\pi}{M\ell^2} \approx \frac{1.27}{M\ell^2}, \tag{4.8}$$

while some estimates[68] and more serious calculations[83] suggest

$$T_{\mathrm{C}} = \frac{2\pi}{3}\,\frac{2\pi}{M\ell^2} \approx \frac{13.2}{M\ell^2}. \tag{4.9}$$

It is generally expected[84] that repulsive interactions should raise the critical temperature compared to the free Bose gas. We will therefore normalize the critical temperature to T_{Bose}:

$$T_{\mathrm{C}} = CT_{\mathrm{Bose}}. \tag{4.10}$$

We will investigate the quantity C in Chapter 7; what is important to note is that this argument produces a temperature that scales like $(M\ell^2)^{-1}$.

Below the melting temperature (or equivalently, the freezing temperature) we expect a crystal; below the condensation temperature we expect the nuclei to condense. It is clear from the analytic expressions of those two transition temperatures—the crystal melting temperature T_{melt} in (4.5) and the nuclear condensation temperature T_{C} in (4.9)—that when either Z or M is increased, the lowest density where the nuclei might condense is pushed deeper into the high-density regime. These temperatures are equal when the interparticle spacing becomes

$$\ell_{\mathrm{max}} = \frac{4\pi^2\Gamma}{3MZ^2\alpha}, \tag{4.11}$$

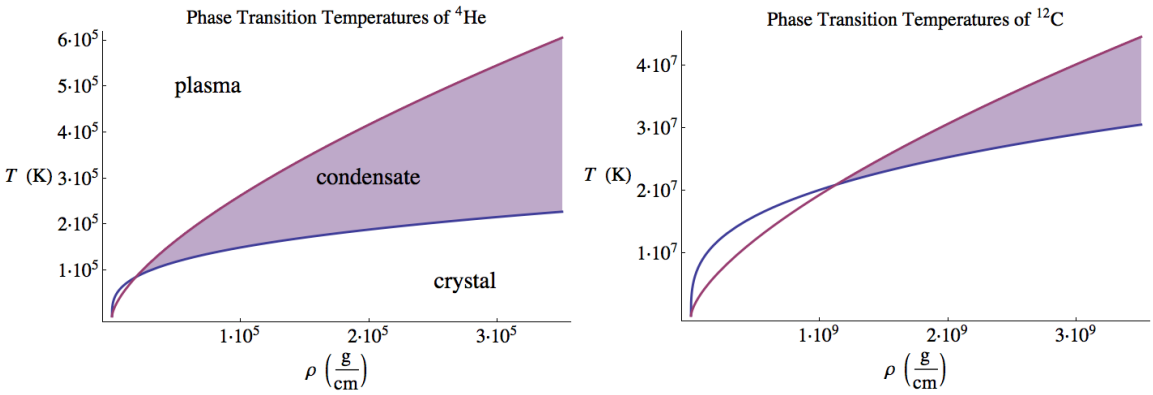

(a) Helium (b) Carbon

Figure 4.1: Below the melting temperature (blue) the nuclei form a crystal; below the condensation temperature given by (4.9) (maroon), but above the melting temperature the nuclei could condense. Above the condensation temperature the nuclei are a plasma.

at smaller interparticle spacings (higher densities), the condensation temperature is larger than the freezing temperature, and a bulk of cooling nuclei has a temperature regime where it is cold enough to condense but not cold enough to freeze.

This is the reason that we focus on helium white dwarfs: for helium ($Z = 2$, $M \approx 3.7\text{GeV}$) $\ell_{\max}$ is about $a_0/12$ while for carbon ($Z = 6$, $M \approx 11.18\text{GeV}$) $\ell_{\max}$ is roughly $a_0/330$; these correspond to mass densities $1.9 \cdot 10^4 \text{g/cm}^3$ and $1.2 \cdot 10^9 \text{g/cm}^3$, respectively. Figure 4.1 shows these temperatures for helium and carbon as a function of mass density ρ.

If instead of using T_C in (4.9) we instead use the more pessimistic condensation temperature in (4.7) the intersection point for helium becomes $\ell_{\max} \approx a_0/26$; for carbon $a_0/700$—mass densities of $1.7 \cdot 10^5 \text{g/cm}^3$ and $1.1 \cdot 10^{10} \text{g/cm}^3$, respectively.

Helium white dwarf central mass densities are typically between $1 \cdot 10^5 \mathrm{g/cm}^3$ and $1 \cdot 10^6 \mathrm{g/cm}^3$[85, 86]. While models of the most extreme far-from-equilibrium super-Chandrasekar-mass supernova-progenitor carbon-oxygen white dwarfs require central densities around $10^9 \mathrm{g/cm}^3$[87] very few of these stars have ever been observed; almost all COWDs have densities around $10^6 \mathrm{g/cm}^3$—well below the densities that allow nuclear condensation. It therefore seems certain that if nuclear condensation has any observable astrophysical signatures, one should consider primarily HeWDs.

The argument to focus on helium has one glaring omission: deuterium! Deuterium is not only lighter but also has a smaller charge—both factors lower the density at which condensation can occur. In fact, deuterium condensation has been considered elsewhere[88, 89, 90, 91] and brown dwarfs are expected to contain a layer of dense deuterium[92]. Deuterium is slightly more complicated—it is spin-1, and therefore admits a number of interesting phases[93] that helium does not, some of which support topological defects. We gain simplicity by studying the spin-0 case.

Chapter 5

Effective Field Theory & Spectrum

In order to understand whether the nuclear condensate has any observable effects we need a framework for performing calculations that encapsulate the dynamics of such a phase well. Fortunately, we can apply the general ideas of effective field theory (EFT) to characterize the low-energy excitations—and thus the dominant aspects of the dynamics at low temperature.

The applicability of EFT methods is actually a little subtle in this regime, because we are interested particularly in temperature regimes *higher* than the crystallization temperature of the nuclei. That is: we expect *a priori* that at zero temperature the condensed phase is unstable. However, the transition between crystal and condensed phases should be first-order, meaning that the condensed phase is only unstable globally, and there should be no local instability. Therefore we can apply zero-temperature EFT methods to deduce the properties of the condensed phase *as though it really survived to* $T = 0$, and then to correct for finite-temperature effects. Thus, we will concern ourselves with the spectrum and other properties at $T = 0$—finite-temperature considerations will be left for Chapter 7.

At the densities of interest the interparticle spacing ℓ is much more than the size of a nucleus, meaning that the nuclei may be treated like point particles and that we may ignore the effect of strong dynamics (as they are relatively short-range),

but much less than a Bohr radius, meaning that the electrons will be degenerate. The Lagrangian that describes nonrelativistic ions and electrons interacting electromagnetically is

$$\mathcal{L} = \psi^\dagger \left(iD_0 + \mu + \frac{\mathbf{D}^2}{2M} \right) \psi - \frac{1}{4} F_{\mu\nu} F^{\mu\nu} + \bar{\chi} \left(iD_\mu \gamma^\mu + \mu_e \gamma^0 + m \right) \chi + \cdots , \quad (5.1)$$

where ψ is the second-quantized ion field, χ the electron field, $F_{\mu\nu} = \partial_\mu A_\nu - \partial_\nu A_\mu$ is the electromagnetic field strength tensor, and the gauge derivatives are

$$D_\mu \psi = (\partial_\mu - iZeA_\mu)\, \psi \quad \text{and} \quad D_\mu \chi = (\partial_\mu + ieA_\mu)\chi \quad (5.2)$$

where Z is the atomic number of the ions; $Z = 2$ for helium. The strong interactions between the helium nuclei are omitted, because the nuclear force between nuclei only becomes strong on length scales comparable to the size of a nucleus, and we are interested in a regime where the nuclei are far apart compared to their size.

To extract the spectrum of this Lagrangian we simply need to diagonalize the sector that is quadratic in the fields. Because the electrons are strongly degenerate a sensible first step towards this goal is to integrate them out. Because the Lagrangian is quadratic this may be done exactly, giving a fermion determinant in the partition function,

$$\begin{aligned} Z &= \int \mathcal{D}\psi^\dagger \, \mathcal{D}\psi \, \mathcal{D}A \, \mathcal{D}\chi \, \mathcal{D}\bar{\chi} e^{iS_{\text{everything}}} \\ &= \int \mathcal{D}\psi^\dagger \, \mathcal{D}\psi \, \mathcal{D}A \ \text{Det} \left[iD_\mu \gamma^\mu + \mu_e \gamma^0 + m \right] e^{iS_{\text{everything but electrons}}} \end{aligned} \quad (5.3)$$

Then, using the identity

$$\text{Det} \left[\widehat{\mathcal{O}} \right] = e^{\,\text{Tr}\left[\log \widehat{\mathcal{O}}\right]} \quad (5.4)$$

we can cast the fermion determinant back into the action as a trace-log,

$$\begin{aligned} S_{\text{electron}} &= \text{Tr}\left[\log\left(iD_\mu\gamma^\mu + \mu_e\gamma^0 + m\right)\right] \\ &= \int \text{đ}^4p \Bigg(\text{tr}\left[\log\left(\not{p} + \mu_e\gamma^0 + m\right)\right] - Zen\left(-p\right)A_0(p) \\ &\qquad + \frac{1}{2}A^\mu\left(-p\right)\Pi_{\mu\nu}(-p,p)A^\nu\left(p\right) + \mathcal{O}\left(A^3\right)\Bigg) \end{aligned} \tag{5.5}$$

where Tr indicates a complete functional trace, tr a trace only over Dirac indices, $\text{đ} = \text{d}/2\pi$ is convenient shorthand for the correctly-normalized momentum integrals, Zn is the electron number density $\chi^\dagger\chi$, and $\Pi_{\mu\nu}$ is the polarization tensor which encapsulates how the two-point function of the electromagnetic field is modified due to the existence of the electrons.

The first term is $\mathcal{O}\left(A^0\right)$ and describes particle-hole excitations—it gives the free energy of the Fermi sphere. The second term, $\mathcal{O}\left(A^1\right)$, will cancel against the charge density of the helium ions for charge neutrality. The third term, $\mathcal{O}\left(A^2\right)$, describes how the degenerate electrons deform and respond to the electromagnetic field, and will prove crucial in determining the correct spectrum. We will ignore all higher order terms, since they do not effect the spectrum at tree level.

As discussed at length in Appendix C, when there is a privileged rest frame—like the situation of interest, since chemical potentials break Lorentz symmetry—the polarization tensor is made of two scalar functions of p_0 and $\mathbf{p}^2$. One particularly convenient encoding that automatically obeys constraints from the Ward-Takahashi identity is

$$\Pi_{\mu\nu} = \begin{pmatrix} \Pi & -\frac{p_i p_0}{\mathbf{p}^2}\Pi \\ -\frac{p_i p_0}{\mathbf{p}^2}\Pi & \frac{p_i p_j p_0^2}{\mathbf{p}^4}\Pi + \left(p_i p_j - \delta_{ij}\mathbf{p}^2\right)\Pi^\perp \end{pmatrix}. \tag{5.6}$$

It is also convenient for our purpose here to parameterize the helium field ψ by

$$\psi = (v + h)e^{i\phi} \tag{5.7}$$

where v is the vacuum expectation value, h is the radial excitation analogous to the Higgs boson, and ϕ is the phase.

In order to proceed, we must fix a gauge. We use the Fadeev-Popov method, and will pick a particular R_ξ gauge. To extract the spectrum it is particularly convenient to fix the gauge

$$\mathcal{L}_{\text{spectrum}} = -\frac{1}{2\xi}\left(\nabla \cdot \mathbf{A} - \frac{2M}{ev}\partial_0 h - \xi\frac{Zev^2}{M}\phi\right)^2. \tag{5.8}$$

Taking $\xi \to \infty$ we will find significant simplification and decoupling of fields from one another.

It is worth pointing out, however, that this gauge fixing is a bit peculiar, because the gauge-fixing condition explicitly depends on v, and so were we to compute a finite-temperature effective potential (a gauge-dependent quantity) with this choice, we would be computing it in a different gauge for each v. We will therefore use the Coulomb gauge

$$\mathcal{L}_{\text{Coulomb}} = -\frac{1}{2\xi}(\nabla \cdot \mathbf{A})^2 \tag{5.9}$$

followed by the $\xi \to 0$ limit to perform finite-temperature calculations in Chapter 7.

The gauge-fixing in (5.8) was chosen to remove all mixing between ϕ and h or $\mathbf{A}$. Moreover, the ghosts introduced by this gauge-fixing are totally decoupled, so we can completely ignore them when we determine the spectrum. With the explicit form of the polarization tensor and gauge-fixing term, the Lagrangian up to

quadratic order in the fields is

$$\begin{aligned}\mathcal{L}_{\text{quad}} &= 2\mu v h + Ze(v^2 - n)A_0 \\ &\quad - \frac{1}{2M}(\nabla h)^2 + \mu h^2 + 2Zevh A_0 - \frac{v^2}{2M}(\nabla\phi)^2 - \frac{Z^2e^2v^2}{2M}\mathbf{A}^2 \\ &\quad - \frac{2M^2}{\xi v^2}(\partial_0 h)^2 - \frac{2M}{\xi Zev}(\nabla\cdot\mathbf{A})\partial_0 h - \frac{1}{2\xi}(\nabla\cdot\mathbf{A})^2 - \frac{\xi Z^2e^2v^4}{2M^2}\phi^2 \\ &\quad - \frac{1}{4}F_{\mu\nu}F^{\mu\nu} + \frac{1}{2}A^\mu \Pi_{\mu\nu} A^\nu; \end{aligned} \tag{5.10}$$

the first line represents the terms constant and linear in the fields A^μ, h, ϕ, the last line is purely electromagnetic, and the other terms are all the other quadratic pieces. Now we take the limit $\xi \to \infty$, which eliminates the first three terms on the third line. Examining the fourth term on that line we see that in that limit ϕ gets an infinite mass, so that excitations of ϕ become impossible to excite: we can drop them from consideration as well.

We also separate the electromagnetic field A_μ into three parts: the time-like part A_0 and two 3-vectors $A^\parallel$, the longitudinal component, and $A^\perp$, the transverse component. These satisfy

$$A_i^\perp p_i = 0 \quad \text{and} \quad A_i^\parallel A_i^\perp = 0. \tag{5.11}$$

where $\mathbf{p}$ is the spatial momentum of any excitation.

With these simplifications the quadratic part of the Lagrangian is

$$\begin{aligned}\mathcal{L}_{\text{quad}} &= 2\mu v h + Ze(v^2 - n)A_0 + h\left[\mu + \frac{\nabla^2}{2M}\right]h + \frac{1}{2}A_i^\perp\left[-\partial_0^2 + \nabla^2 - m_A^2 + \Pi^\perp\right]A_i^\perp \\ &\quad + \frac{1}{2}A_0\left[-\nabla^2 + \Pi\right]A_0 + A_0\left[\partial_0\partial_i\left(-1 + \frac{\Pi}{\nabla^2}\right)\right]A_i^\parallel + 2Zevh A_0, \\ &\quad + \frac{1}{2}A_i^\parallel\left[\delta_{ij}(-\partial_0^2 + \nabla^2 - m_A^2) - \partial_i\partial_j\left(1 - \frac{\partial_0^2}{\nabla^4}\Pi\right)\right]A_j^\parallel \end{aligned} \tag{5.12}$$

where we have defined the photon mass

$$m_A^2 = \frac{Z^2 e^2 v^2}{M} = \frac{Z^2 4\pi\alpha v^2}{M}. \tag{5.13}$$

To ensure charge neutrality one must, at zero temperature, pick $\langle\, \psi \,\rangle = v = \sqrt{n}$ and $\mu = 0$. We will, until Chapter 7, simply set $\mu = 0$. This choice implies that single-photon-exchange contributes nothing to the energy, which is exactly what one expects if the ion and electron charge densities cancel one another exactly. Instead, only two-(or-more)-photon-exchange can contribute to the energy: the first photon induces a charge density imbalance and the second communicates the interaction of the resulting charge fluctuations. These loop effects are higher order in α and are thus small.

We can now begin examining $\mathcal{L}_{\text{quad}}$ and determining its spectrum. First, note that $A^\perp$ is totally decoupled from all other fields at this order. It encodes the two transverse photons with dispersion relation

$$p_0^2 = \mathbf{p}^2 + m_A^2 - \Pi^\perp(p_0, \mathbf{p}^2). \tag{5.14}$$

Assuming that the magnetic effects of due to the electrons, such as Landau damping, are unimportant so that $\Pi^\perp$ is small, this simplifies to

$$p_0^2 = \mathbf{p}^2 + m_A^2, \tag{5.15}$$

the dispersion relation of a massive scalar.

The rest of the remaining fields mix. Since this sector is quadratic we can exactly integrate them out one by one. The choice of which fields to integrate out is arbitrary and the physics must be independent of this choice.

Let us integrate out $A^{\parallel}$. Note that

$$(A\delta_{ij} + B\partial_i\partial_j)^{-1} = \frac{1}{A}\left(\delta_{ij} - \frac{B}{A + B\nabla^2}\partial_i\partial_j\right) \tag{5.16}$$

and therefore we can integrate out $A^{\parallel}$ easily. The result is

$$\begin{aligned}\mathcal{L}_{\text{quad}} = &\frac{1}{2}A_i^{\perp}\left[-\partial_0^2 + \nabla^2 - m_A^2 + \Pi^{\perp}\right]A_i^{\perp} \\ &+ h\left[\mu + \frac{\nabla^2}{2M}\right]h + \frac{1}{2}A_0\left[m_A^2\frac{\nabla^2 - \Pi}{-\partial_0^2 - m_A^2 + \Pi\frac{\partial_0^2}{\nabla^2}}\right]A_0 + 2Zevh A_0\end{aligned} \tag{5.17}$$

Notice that the second line contains no time derivatives but for those that arose from integrating out $A^{\parallel}$; without the dynamical effects of $A^{\parallel}$ it is not possible to get a quasiparticle from the remaining h, A_0 sector.

Finally, let us eliminate A_0. Integrating it out yields

$$\begin{aligned}\mathcal{L}_{\text{quad}} =&h\left[\mu + \frac{\nabla^2}{2M} + 2M\frac{-\partial_0^2 - m_A^2 + \Pi\partial_0^2/\nabla^2}{-\nabla^2 + \Pi}\right]h \\ &+ \frac{1}{2}A_i^{\perp}\left[-\partial_0^2 + \nabla^2 - m_A^2 + \Pi^{\perp}\right]A_i^{\perp}.\end{aligned} \tag{5.18}$$

We have already discussed the excitations associated with the transverse photons $A^{\perp}$, so let us focus on the h sector of this Lagrangian. The propagator $G_h(p_0, \mathbf{p}^2)$ associated with h is

$$G_h\left(p_0, \mathbf{p}^2\right) = \frac{\mathbf{p}^2/2M}{p_0^2 - \left(\frac{\mathbf{p}^2}{2M}\right)^2 - \frac{\mathbf{p}^2 m_A^2}{\mathbf{p}^2 + \Pi(p_0, \mathbf{p}^2)}}. \tag{5.19}$$

The dispersion relation of the quasiparticle excitations of h can be found by finding the poles of $G_h(p_0, \mathbf{p}^2)$. The poles are the solutions to

$$p_0^2 = \left(\frac{\mathbf{p}^2}{2M}\right)^2 + \frac{\mathbf{p}^2 m_A^2}{\mathbf{p}^2 + \Pi(p_0, \mathbf{p}^2)}. \tag{5.20}$$

but actually deducing the dispersion relation with a nontrivial $\Pi(p_0, \mathbf{p}^2)$ is nontrivial and will be the focus on the remainder of this chapter.

Before we pursue these dispersion relations it is helpful to perform some sanity checks to see if (5.20) has correct limiting cases. First, notice that if the ions were uncondensed, ie. $m_A = 0$, this relation reduces to

$$p_0^2 = \left(\frac{\mathbf{p}^2}{2M}\right)^2, \tag{5.21}$$

simply the dispersion relation for the nonrelativistic ions that we put in. Second, notice that if the electrons were totally rigid and didn't respond to electromagnetic fields, the function $\Pi(p_0, \mathbf{p}^2)$ would vanish, leaving us with

$$p_0^2 = \left(\frac{\mathbf{p}^2}{2M}\right)^2 + m_A^2, \tag{5.22}$$

the gapped dispersion relation from the jellium model of Coulomb-interacting scalars with a static charge-neutralizing background[94, 95]. Our more general expression (5.20) passes these checks, which gives confidence in our procedure.

To progress any further we need explicit functions for the polarization tensor function $\Pi(p_0, \mathbf{p}^2)$. A simple comparison indicates that for our purposes it is okay to use the zero-temperature polarization tensor: the smallest densities where a condensate might appear have $a_0/\ell \approx 12$ have Fermi energy around 0.5MeV, while the typical temperature is 10^6K≈86eV, dramatically smaller: any finite-temperature corrections should be suppressed.

The function $\Pi(p_0, \mathbf{p}^2)$ is nonanalytic, and its behavior as p_0 and $\mathbf{p}^2$ become small depends therefore depends intricately on how they relate to one another as

they become small. In particular there are three interesting limits of $\Pi(p_0, \mathbf{p}^2)$:

$$\begin{aligned} \lim_{\mathbf{p}^2 \to\ 0} \operatorname{Re}\Pi(p_0 = 0, \mathbf{p}^2) &= m_s^2 \\ \lim_{\mathbf{p}^2 \to\ 0} \operatorname{Im}\Pi(p_0 = 0, \mathbf{p}^2) &= 0 \end{aligned} \tag{5.23}$$

$$\begin{aligned} \lim_{\mathbf{p}^2 \to\ 0} \operatorname{Re}\Pi(p_0, \mathbf{p}^2) &\to\ -\frac{4\alpha k_{\mathrm{F}}^3}{3\pi\mu_e}\frac{\mathbf{p}^2}{p_0^2} \\ \lim_{\mathbf{p}^2 \to\ 0} \operatorname{Im}\Pi(p_0, \mathbf{p}^2) &= 0 \end{aligned} \tag{5.24}$$

$$\begin{aligned} \lim_{\mathbf{p}^2 \to\ 0} \operatorname{Re}\Pi(p_0 = x v_{\mathrm{F}} p, \mathbf{p}^2) &= m_s^2 \left(1 - \frac{x}{2}\ln\left|\frac{1+x}{1-x}\right|\right) \\ \lim_{\mathbf{p}^2 \to\ 0} \operatorname{Im}\Pi(p_0 = x v_{\mathrm{F}} p, \mathbf{p}^2) &= \frac{\pi}{2} m_s^2\, x\ \theta(1-x) \end{aligned} \tag{5.25}$$

which can be found in a large number of different references[96, 97, 98, 82].[1] In these relations θ is the usual Heaviside function,

$$\begin{gathered} \mu_e = \sqrt{k_{\mathrm{F}}^2 + m^2}, \qquad v_{\mathrm{F}} = \frac{k_{\mathrm{F}}}{\mu_e}, \qquad k_{\mathrm{F}}^3 = 3\pi^2 n_e = 3\pi^2 Z n, \\ m_s^2 = \frac{4\alpha\mu_e k_{\mathrm{F}}}{\pi}, \quad \text{and} \quad p = \sqrt{\mathbf{p}^2} \end{gathered} \tag{5.26}$$

are the electron chemical potential, Fermi velocity, and Fermi momentum, screening mass, and magnitude of the spatial momentum, respectively, and $n_e = Zn$ is the electron density; the non-relativistic analogues of the first two quantities are found simply by replacing μ_e with the electron mass m. Let us discuss how each of these limits fits into the implicit dispersion relation (5.20).

The first limit is useful for deducing the momentum-dependent static potential between the excitations encoded in h. The polarization tensor keeps the

[1] In Reference [4] there is a typo in the equation analogous to (5.24): it claims that these expressions are the limit as p_0, and not $\mathbf{p}^2$, vanishes. This would prevent us from making a self-consistent approximation when finding the gapped mode.

potential from being Coulomb; instead one gets a screened potential with Friedel oscillations[82, 99, 100, 68, 101, 102, 103].

If the dispersion relation supports gapped quasiparticles then there should be a solution wherein p_0 remains finite while the spatial momentum $\mathbf{p}$ vanishes. Thus, we can use the polarization tensor as in (5.24); using that limit in the dispersion relation and taking $\mathbf{p} \to 0$ one finds

$$p_0^2 = m_A^2 + \frac{4\alpha Z n}{\mu_e} = 4\pi Z \alpha n \left(\frac{Z}{M} + \frac{1}{\mu_e} \right) = \frac{4\pi Z \alpha n}{m_{\text{red}}} \tag{5.27}$$

where the reduced mass $m_{\text{red}}^{-1} = Z/M + \mu_e^{-1}$. That we found a finite p_0 shows that the approximation made is a self-consistent one: *assuming* p_0 remains finite as $\mathbf{p}^2 \to 0$ in the polarization tensor one can *derive* a p_0 that solves the implicit dispersion relation that indeed has that property.

This frequency differs from the electron plasma frequency

$$\omega_p = \frac{4\pi \alpha n_e}{m} \tag{5.28}$$

in but one way—the electron mass should be changed to the reduced mass. This change makes it seem clear that we should think of this mode, called the plasmon, as the result of the electrons vibrating against the neutralizing ion background instead of a rigid neutralizing background. Plugging in realistic numbers for helium,

$$p_0 \approx 500\text{eV} \left(1 + \frac{m^2}{k_{\text{F}}^2} \right)^{-1/4} \frac{a_0}{\ell} \approx 5.8 \cdot 10^6 \text{K} \left(1 + \frac{m^2}{k_{\text{F}}^2} \right)^{-1/4} \frac{a_0}{\ell}, \tag{5.29}$$

which is ten time hotter than the typical temperature at which we might expect condensation to occur (as in, for example Figure 4.1a). These degrees of freedom should thus be strongly Boltzmann-suppressed at these temperatures.

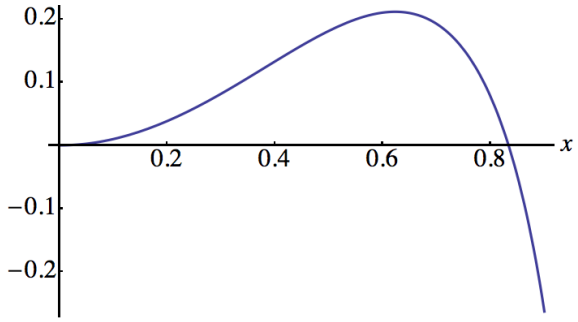

Figure 5.1: The left-hand side of (5.30). The function takes its maximum value of ≈ 0.212 at $x \approx 0.623$ and vanishes at $x \approx 0.834$; for all larger x the function is negative. Unshown is the asymptote of $-1/3$ as $x \to \infty$.

In addition to gapped modes we can also look for gapless modes: modes which have p_0 proportional to p. For this search we use the limit of the polarization tensor in (5.25), where we take $p_0 = x v_{\rm F} p$ with constant x and then take $\mathbf{p} \to 0$. In this limit the $(\mathbf{p}^2/2M)^2$ term may be neglected and the dispersion relation may be massaged into the a constraint on the dimensionless constant x. One finds

$$x^2 \left(1 - \frac{x}{2} \ln \left| \frac{1+x}{1-x} \right| + i \frac{\pi}{2}\, x\, \theta(1-x)\right) = \frac{m_A^2}{v_{\rm F}^2 m_s^2}. \tag{5.30}$$

The real part of the left-hand side is plotted as a function of x in Figure 5.1. The right-hand side is, numerically,

$$\frac{m_A}{v_{\rm F} m_s} = 0.8 Z^{2/3} \left(1 + \frac{m^2}{k_{\rm F}^2}\right)^{1/4} \alpha^{1/2} \sqrt{\frac{m}{M}} \sqrt{\frac{a_0}{\ell}} \approx 0.0012 \left(1 + \frac{m^2}{k_{\rm F}^2}\right)^{1/4} \sqrt{\frac{a_0}{\ell}}, \tag{5.31}$$

squared, and even a very large astrophysically possible density (and a_0/ℓ) will yield quite a small quantity. We can therefore solve (5.30) and (5.20) by an expansion in x. At leading order one finds $x = m_A/m_s v_{\rm F}$ and

$$p_0 = \frac{m_A}{m_s} p - i\pi \frac{m_A^2}{4 v_{\rm F} m_s^2} p. \tag{5.32}$$

Note that the imaginary part, which conveys how quickly the mode decays, is smaller than the real part by a factor of x, so that it is reasonable to say that the quasiparticle is long-lived. We identify the speed of this mode c_H as

$$c_H = \frac{m_A}{m_S}, \tag{5.33}$$

which for realistic numbers is roughly $0.001c$, or 300km/s. The attenuation is only apparent using the full form of Π as in (5.25); if we had used simply the Thomas-Fermi approximation $\Pi = m_s^2$ the mode would be truly stable. This makes it clear that the imaginary part encodes the inelastic coupling to electron-hole pairs that the polarization tensor incorporates. Note that this coupling actually becomes stronger at high density, but is kept small by the ratio of the electron mass to ion mass m/M, which totally overwhelms any enhancement that a_0/ℓ provides. It thus seems clear that the gapless mode is long-lived because this mass mismatch keeps most of the quasiparticle–particle-hole interactions elastic. The dispersion relation (5.32) is valid for a wide temperature range, including those for realistic HeWD densities, as discussed in Reference [4].

Note that c_H doesn't vanish as $\alpha \to 0$: this mode survives as electromagnetism is dialed down. This leads us to conclude that the mode does not correspond to the electrons and nuclei vibrating in opposite directions which would require electromagnetism to restore their imbalance, but that the mode is a density fluctuation.

This gapless quasiparticle was first pointed out in Reference [4]. Previous analyses missed this quasiparticle because they omitted the off-diagonal terms in (5.6) proportional to Π, violating the Ward-Takahashi identities and thus violating

gauge invariance. However, its omission might not be unexpected—its existence depends intricately on a number of factors. First, if either the electrons or nuclei were not dynamical, the mode would not exist. Second, if the nuclei were not condensed (ie. $m_A = 0$) the mode would also disappear. This is comforting, because it is well-known that an electron plasma has no gapless mode, but only a gapped plasmon.

Our tree-level analysis has yielded two quasiparticles: the massive plasmon and the gapless mode. Gaplessness at tree-level, though, is not guaranteed to survive quantum corrections. Indeed, typically gaplessness only survives if the mode is protected by a symmetry that eliminates the possibility of developing a gap. It isn't clear that this mode is so privileged, and because even a small mass is qualitatively different from no mass we should try to understand whether it indeed remains gapless.

The effective Lagrangian that results from integrating all the fields out except for h and $A^\perp$ (of which $\mathcal{L}_{\text{quad}}$ in (5.18) is a part) will be expressed in powers of those two fields. However, this is not the most convenient effective Lagrangian, in the sense that the propagator of the field h in (5.19) has nontrivial momentum-dependent residues, which is obvious from the $\mathbf{p}^2/2M$ factor in its numerator. Instead we can work with the canonically-normalized field

$$H = \left(\frac{1}{\sqrt{2}}\sqrt{-\frac{\nabla^2}{2M}}\right)^{-1} h \tag{5.34}$$

which has the propagator

$$G_H\left(p_0, \mathbf{p}^2\right) = \frac{1}{p_0^2 - \left(\frac{\mathbf{p}^2}{2M}\right)^2 + \frac{\mathbf{p}^2 m_A^2}{\mathbf{p}^2 + \Pi(p_0, \mathbf{p}^2)}} \tag{5.35}$$

which in the gapless quasiparticle regime $p_0 = x v_{\mathrm{F}} p$ and $\mathbf{p}^2 \to\ 0$ becomes

$$G_H\left(p_0, \mathbf{p}^2\right) = \frac{1}{p_0^2 - c_H^2 \mathbf{p}^2 + \cdots}. \tag{5.36}$$

Expressed in terms of H, any interactions that h had must now carry derivatives. That it is always derivatively coupled implies that H has the shift symmetry

$$H \to\ H + \delta H \tag{5.37}$$

where δH is a constant. Since no mass term for H can be written that is invariant under this symmetry we know that no quantum effects can generate a mass for this mode.

This argument—that the field is derivatively coupled, enjoys a shift symmetry, and thus is exactly massless—is formalized for this system in Reference [4] but is logically the same as a common argument that guarantees that Goldstone bosons remain massless to all orders. The question then arises: is H a Goldstone mode?

At first it seems like this is impossible: H arose from the breaking a gauge symmetry, the U(1) of electromagnetism and so it should be eaten by the photon, as required by the Higgs mechanism. However, in non-relativistic theories the Higgs mechanism is not so straightforward. With broken Lorentz invariance from the chemical potential, whether the gapless modes are traded for massive gauge bosons depends on whether that gauge force is screened or not[104, 105]. In particular, the Higgs mechanism evades the Goldstone theorem by a loophole via the IR divergences

intimately connected to the photons' $1/r^2$ force. In this case, even though we have a gauge symmetry this loophole is destroyed by the screening. This subtle exception-to-the-exception is well-known to those who know it[104, 105, 107, 108, 109]. The static potential generated by (5.23) falls off more quickly[68, 99, 101, 102] than the required[105] $1/r^3$ to yield a Goldstone mode with a linear dispersion relation.

To summarize, degenerate electrons and condensed ions support three distinct quasiparticles: the massive transverse photons with dispersion relation

$$p_0^2 = \mathbf{p}^2 + m_A^2, \tag{5.38}$$

the familiar plasmon with dispersion relation

$$p_0^2 = \frac{4\pi Z\alpha n}{m_{\text{red}}} + \left(\frac{\mathbf{p}^2}{2M}\right)\left(1 - \frac{m_{\text{red}}}{\mu_e}\right), \tag{5.39}$$

and the new, unusual, long-lived gapless mode with dispersion relation

$$p_0 = c_H\left(1 - i\pi\frac{c_H}{v_{\text{F}}}\right)p. \tag{5.40}$$

Even though this mode is a density oscillation with a linear dispersion relation, it is *not* the typical zero-sound that Fermi liquids support, but neither is it the hydrodynamic first-sound. We call this particle the *half-sound* to remind us of its unusual properties.

Chapter 6

Potential Signatures

Now that we have a good understanding of the low-energy degrees of freedom that the nuclear condensate supports, we can try to understand whether it has any potentially astrophysically observable consequences.

The primary observable way that these degrees of freedom nuclear condensation supports might effect helium white dwarfs is by changing how they cool[66, 67, 68]. In particular, we will examine how the half-sound can help cool the star in two different ways.

In order to appreciate the changes nuclear condensation effects, it is helpful to understand the standard lore of white dwarfs cooling. Young, hot ($T \gtrsim 10^9$K) white dwarfs primarily cool by the decay into neutrinos of the massive plasmon mode that exists even without the condensation of the nuclei[110, 111, 112]. These neutrinos promptly escape the star, allowing the whole bulk radiate at once. The cooling through neutrino emission is observable through the nonradial excitations those stars exhibit[113, 114]. However, as the star cools plasmon excitations become Boltzmann-suppressed, and the neutrino emission is essentially extinguished, so that below roughly 10^9K the primary way energy is radiated is electromagnetic surface radiation.

In Section 6.1, we will quantify the annihilation of half-sound quasiparticles

into neutrinos. Because it is a gapless mode, the half-sound does not suffer Boltzmann suppression at any temperature, so one might expect this process to prolong the period in which bulk neutrino cooling dominates. We will show that without a very large condensation temperature T_C (which translates to a large C by (4.10)), the neutrino emission from half-sound annihilation is not competitive with photoemission from the surface. Combined with the conclusions of Chapter 7, this makes it seem unlikely that neutrino emission will be observable.

In Section 6.2, we will show that nuclear condensation changes the specific heat dramatically. This change would help get interior heat to the surface faster, meaning that they would cool much faster. Whether the change in HeWD cooling curves would be noticeable remains unsettled, with simple calculations[67] and models[115] indicating a notable difference and more detailed calculations[86] indicating that a difference exists but will be difficult to establish observationally. Previous calculations of the specific heat[66, 67, 68] did not account for the (then-unknown) half-sound but merely noted that the condensed nuclei had a very low specific heat, so that even the more detailed calculations should not be considered definitive.

Moreover, as discussed in Reference [67], if the heat capacity of the crystalline phase is much higher than the condensed phase, then when the star cools and the core leaves the condensed phase in favor of the crystal phase, there will effectively be a cessation of heat transport from the core to the surface, meaning that the stars should become very dim, as the crust sheds the heat it has and comes into a new equilibrium with the crystal. It is tempting to think that the post-crystallization

period of dimness a HeWD would exhibit is an explanation of the dearth of HeWDs discussed in the introduction to this Part, though it is unknown and beyond the scope of this work to determine if this explanation can survive more detailed scrutiny.

6.1 Half-sound Annihilation

Let us focus on the annihilation of the half-sound into neutrinos. The half-sound is described by the effective Lagrangian

$$\mathcal{L}_{\mathrm{H}} = \frac{1}{2} H \left[-\partial_0^2 + c_H^2 \nabla^2 \right] H + \cdots \tag{6.1}$$

where we have exhibited only the quadratic piece explicitly, but there are many interaction terms unshown.

Because H is gapless, it is kinematically impossible for it to decay into a neutrino-antineutrino pair. Therefore, in contrast to the massive plasmon, the main mechanism to get neutrino radiation from the half-sound is by the annihilation process $HH \to \nu\bar{\nu}$.

Naïvely we can estimate the neutrino emissivity Q by simple arguments. The leading contribution is given by the square of the Feynman diagram shown in Figure 6.1. Thus, we know that

$$Q \sim G_F^2 \frac{1}{M^2} T^{11}. \tag{6.2}$$

There are two factors of the Fermi constant G_F, as in any weak process. There are two factors of the ion mass M in the denominator because H is derivatively coupled, and as argued in Chapter 5, each H in a vertex brings $\sqrt{-\nabla^2/2M}$, so that the amplitude given by Figure 6.1 is proportional to M^{-1}. Finally, T^{11} makes

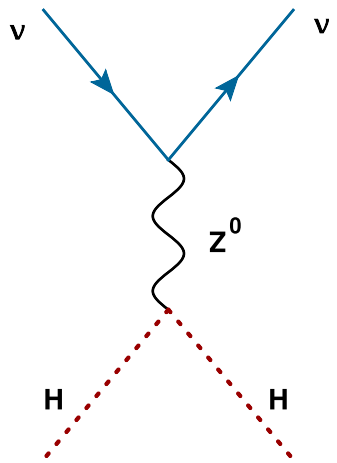

Figure 6.1: The leading process by which two H quasiparticles (red dotted lines) can decay into neutrinos (blue solid) is mediated by a Z-boson (black wavy line). Reproduced from Reference [5].

up the rest of the required dimensions, since the temperature is the only remaining dimensionful scale in the problem.

The mass suppression is a severe penalty, and is discouraging for the relevance of quasiparticles annihilating into neutrinos. However, the simple reasoning that gives us the scaling cannot tell us how Q depends on the dimensionless quantity c_H. Because the temperature and typical energy should be equal, on the one hand it seems reasonable to think that $T \sim c_H p$, so that momentum integrals should have their scale set by T/c_H, which would provide an enormous enhancement: $Q \sim c_H^{-11}$. On the other hand, the phase space for the decay should vanish as $c_H \to 0$, which should reduce Q. On the gripping hand we need not argue a certain dependence on c_H: we can simply calculate the annihilation probability per unit volume and the emissivity Q.

By a series of matching calculations we will derive the coupling between the

half-sound and neutrinos, compute the annihilation probability, and show that Q is enhanced by c_H^{-7}, but that while this enhancement is still tremendous, it is not enough to make neutrino emission competitive with photo emission.

6.1.1 Matching to the Standard Model

In this section we will deduce the coupling of the half-sound to neutrinos. The half-sound H is a collective mode of both the degenerate electrons and the condensed nuclei; both electrons and nuclei couple to the Z-boson. By understanding how the nuclei couple to the Z-boson and using the coupling of the Z to neutrinos supplied[118] by the Standard Model (SM),

$$\mathcal{L}_{Z\nu\bar{\nu}} = \frac{g_{\mathrm{W}}}{\cos\theta_{\mathrm{W}}} Z_\mu \frac{1}{2}\bar{\nu}\gamma^\mu \left(\frac{1-\gamma_5}{2}\right)\nu, \tag{6.3}$$

we can calculate the diagram in Figure 6.1; an effective $HH\nu\bar{\nu}$ vertex. Here g_{W} is the weak coupling constant, θ_{W} is the Weinberg angle, ν represents the neutrino fields and γ the usual Dirac matrices.

The SM also provides the coupling of the Z-boson to the quarks. The relevant terms in the SM Lagrangian are[118]

$$\begin{aligned}\mathcal{L}_{Z\bar{q}q} = \frac{g_{\mathrm{W}}}{\cos\theta_{\mathrm{W}}} Z_\mu \Bigg[& \frac{1}{2}\bar{u}\gamma^\mu \left(\frac{1-\gamma_5}{2}\right) u - \frac{2}{3}\sin^2\theta_{\mathrm{W}}\bar{u}\gamma^\mu u \\ & -\frac{1}{2}\bar{d}\gamma^\mu \left(\frac{1-\gamma_5}{2}\right) d + \frac{1}{3}\sin^2\theta_{\mathrm{W}}\bar{d}\gamma^\mu d \Bigg]\end{aligned} \tag{6.4}$$

where the u and d fields represent the up and down quarks, respectively.

From this, we can immediately deduce the form of the Lagrangian that describes how the Z interacts with the nucleon isospin doublet N. By symmetry we

know that the coupling is described by

$$\mathcal{L}_{Z\bar{N}N} = \frac{g_{\rm W}}{\cos\theta_{\rm W}} Z_\mu \bar{N}\gamma^\mu \left[\frac{1}{2}T^3 - \sin^2\theta_{\rm W} Q - (g_A + \Delta_s)\gamma_5 T^3 + \cdots\right] N \tag{6.5}$$

where $T^3 = \tau^3/2$ is the third component of weak isospin, Q the electric charge in units of the fundamental charge, g_A is the nucleon axial charge (roughly 1.26), Δ_s the strange axial charge (-0.16 ± 0.15), and higher dimensional terms are not shown.

Importantly, because the vector current is conserved the corresponding coupling (the piece without γ_5) does not get renormalized, unlike the axial coupling. Equivalently, one can note that the SM enjoys a spurious U(1) gauge symmetry, where the spurious gauge fields are proportional to $Z_\mu T^3$. The effective action when we pass to nucleon degrees of freedom must also have this spurious symmetry, and this restriction is enough to fix the coefficient on that term.

We can take the nonrelativistic limit of this Lagrangian, so that we can make it compatible with the non-relativistic terms that we used for the nuclei in effective Lagrangian while deriving the spectrum. It is easy to verify that this reduction yields

$$\mathcal{L}_{ZN\bar{N}} \xrightarrow[\text{nonrel.}]{} \frac{g_{\rm W}}{\cos\theta_{\rm W}} \left[\frac{1}{2} Z_0 N^\dagger \left(T^3 - \sin^2\theta_{\rm W} Q\right) N - (g_A + \Delta_s) Z_i N^\dagger \sigma^i T^3 N + \cdots\right]. \tag{6.6}$$

So that we see that Z couples to the isospin and electric charge, and to the spin of the nucleons in an isospin-dependent way.

We can perform the same trick, this time passing from nucleon degrees of freedom to helium-nuclei degrees of freedom. Helium is isospin-0, so the first term will vanish. Moreover, the wavefunction of ^{4}He is dominated by the total-spin-0

piece (between 85% and 90% is $S = 0$; see Reference [119]), so the spin-dependent piece should be negligible and we can ignore the final terms. Thus, we expect the dominant coupling of helium nuclei to the Z-boson to be encapsulated by

$$\mathcal{L}_{Z^4\mathrm{He}^4\mathrm{He}} = -2\frac{g_\mathrm{W}\sin^2\theta_\mathrm{W}}{\cos\theta_\mathrm{W}} Z_0 \psi^\dagger \psi, \tag{6.7}$$

where the 2 comes from the fact that the electric charge of the helium nucleus is 2 and the ψ, as in Chapter 5, represent the nuclei. This interaction again has no unknown coefficient because it corresponds to part of a conserved current and is not renormalized. Note the suppression of this interaction by the Weinberg angle. If $\sin\theta_\mathrm{W}$ vanished, then the Z would not couple to an isoscalar source like ^{4}He at all.

Finally, combining (5.7) and (5.34) we can eliminate ψ in favor of the half-sound degree of freedom. The result is

$$\mathcal{L}_{ZHH} = -\frac{g_\mathrm{W}\sin^2\theta_\mathrm{W}}{2M\cos\theta_\mathrm{W}} Z_0 \left(\sqrt{-\nabla^2} H\right)^2. \tag{6.8}$$

In principle H mixes linearly with Z, but this weak-sector mixing is negligible and can be ignored for our purposes. One might be concerned that this linear mixing allows a single H to decay directly into neutrino pairs, but this is prohibited kinematically: an on-shell H carries a space-like four-momentum, while a pair of on-shell massless neutrinos have either time-like or light-like four-momentum.

We can finally ascribe an amplitude to the diagram in Figure 6.1. This is facilitated by noting that the temperatures of interest, 10^6K or even the astrophysically very high 10^9K correspond to 10^{-7} or 10^{-5}GeV respectively. The typical momentum in the Z propagator will be on the scale of the typical half-sound momentum T/c_H.

Even with the enhancement by c_H the four-momentum in the propagator will be negligible compared to the mass $m_{\rm Z} \approx 91{\rm GeV}$.

Simply integrating the Z-boson out, we find the coupling between half-sound excitations and neutrinos,

$$\begin{aligned}\mathcal{L}_{HH\bar{\nu}\nu} &= \left(\frac{2g_{\rm W}}{\cos\theta_{\rm W}}\right)^2 \frac{\sin^2\theta_{\rm W}}{8MM_Z^2}\bar{\nu}\gamma^0\left(\frac{1-\gamma_5}{2}\right)\nu\left(\sqrt{-\nabla^2}H\right)^2 \\ &= \frac{2G_F\sin^2\theta_{\rm W}}{\sqrt{2}M}\bar{\nu}\gamma^0\left(\frac{1-\gamma_5}{2}\right)\nu\left(\sqrt{-\nabla^2}H\right)^2 \end{aligned} \tag{6.9}$$

where we simply replaced

$$\left(\frac{g_{\rm W}}{\cos\theta_{\rm W}}\right)^2 = \frac{8G_F M_Z^2}{\sqrt{2}}, \tag{6.10}$$

which we can take to be the definition of the Fermi coupling constant G_F. The coupling $\mathcal{L}_{HH\bar{\nu}\nu}$ in (6.9) will indeed yield a decay rate that is proportional to $(G_F/M)^2$, as advertised.

6.1.2 The Neutrino Emissivity Q

The energy carried away per unit volume per unit time in neutrinos, or the neutrino emissivity, Q can be compute by integrating the distribution of half-sound quasiparticles agains the probability that they annihilate. That is,

$$Q = \int \text{đ}^3k\,\text{đ}^3k'\; n\left(k_0\right) n\left(k_0'\right)\left(k_0+k_0'\right)\Gamma(k,k') \tag{6.11}$$

where we include the factor $(k_0 + k_0')$ so that we keep track of the energy emitted, and not just the number of neutrino pairs. Here n is the Bose-Einstein distribution that the half-sound obeys,

$$n\left(k_0\right) = \frac{1}{e^{k_0\beta}-1} \tag{6.12}$$

where we use the inverse temperature $\beta = k_{\mathrm{B}}/T = 1/T$, and $\Gamma(k, k')$ is the probability per unit time per unit volume that two half-sound quasiparticles annihilate. We will first compute $\Gamma(k, k')$ and use it to compute Q.

To compute $\Gamma(k, k')$ we adopt a finite-volume regularization so that we will imagine all processes happening in a cubic volume of linear size L in a time T, and we normalize all fields to the volume $V = L^3$. With this prescription the field operators are given by

$$H = \frac{1}{\sqrt{V}} \sum_k \frac{1}{\sqrt{2\omega_k}} \left[a_k e^{-ikx} + {a_k}^\dagger e^{ikx} \right] \tag{6.13}$$

$$\nu = \frac{1}{\sqrt{V}} \sum_{p,s} \frac{1}{\sqrt{2\omega_p}} \left[c_p u_p^s e^{-ipx} + {d_p}^\dagger v_p^s e^{ipx} \right] \tag{6.14}$$

where a is a bosonic ladder operator, c and d are fermionic ladder operators, the momenta $\mathbf{k}$ and $\mathbf{p}$ take values $2\pi\mathbf{z}/L$, where $\mathbf{z}$ is a triplet of integers, ω_k and ω_p are the energies of an excitation of their respective fields with their labelled momenta, and u_p^s and v_p^s are the usual Dirac spinors of momentum p and spin s.

At finite volume we also should not integrate over all momenta, nor should we use the normal Dirac delta function. Instead, we should freely substitute

$$\delta^4(p - p') \Leftrightarrow \frac{VT}{(2\pi)^4} \delta_{pp'}, \quad \delta^3(p - p') \Leftrightarrow \frac{V}{(2\pi)^3} \delta_{pp'} \quad \text{and} \quad \int \text{đ}^3 p \Leftrightarrow \frac{1}{V} \sum_p . \tag{6.15}$$

Up to an irrelevant phase the amplitude for two half-sound particles annihilating

into a pair of neutrinos is

$$\begin{aligned}\mathcal{A}^{st}_{kk'pp'} = 2 \times \bar{u}^s_p \gamma^0 \left(\frac{1-\gamma_5}{2}\right) v^t_{p'} \frac{2G_F \sin^2\theta_{\rm W}}{\sqrt{2}M} kk' \\ \times \left(\frac{1}{\sqrt{V}}\right)^4 \frac{1}{\sqrt{2\omega_k 2\omega_{k'} 2\omega_p 2\omega_{p'}}} \\ \times (2\pi)^4 \delta^4(p+p'-k-k')\end{aligned} \tag{6.16}$$

where the first factor of 2 accounts for the two possible contractions of H with the vertex, and the rest of the first line accounts for the neutrinos in the final state, and the value of the vertex itself; the second line tracks the normalization; and the third enforces the required kinematics.

Because neutrinos of any spin or momentum will escape the star, we sum over all possible final states and compute

$$\begin{aligned}\Gamma(k,k') &= \frac{1}{T}\sum_{pp'st} \left|\mathcal{A}^{st}_{kk'pp'}\right|^2 \\ &= \sum_{pp'} \frac{2G_F^2 \sin^4\theta_{\rm W}}{M^2V^4T} \frac{(kk')^2}{2^4\omega_k\omega_{k'}\omega_p\omega_{p'}} \times \left(VT\delta_{p+p',k+k'}\right)^2 \\ &\qquad \times \ \mathrm{tr}\left[(\not{p}+m_\nu)\gamma^0(1-\gamma^5)(\not{p}'-m_\nu)\gamma^0(1-\gamma^5)\right].\end{aligned} \tag{6.17}$$

The fermionic trace is independent of the neutrino mass m_ν and gives $8\,(p_0p'_0 + \mathbf{p}\cdot\mathbf{p}')$. Translating back to continuous language,

$$\Gamma(k,k') = \frac{G_F^2 \sin^4\theta_{\rm W}}{M^2V^3} \int V\mathrm{d}^3p\, V\mathrm{d}^3p' (2\pi)^4\delta^4(p+p'-k-k') \frac{(kk')^2(p_0p'_0+\mathbf{p}\cdot\mathbf{p}')}{\omega_k\omega_{k'}\omega_p\omega_{p'}}. \tag{6.18}$$

We evaluate this integral exactly in Appendix D. The result is

$$\Gamma(k,k') = \frac{G_F^2 \sin^4\theta_{\rm W}}{6\pi c_H^2 M^2 V} kk' \left|k+k'\right|^2 \theta\Big[c_H(k+k') - \left|k+k'\right|\Big]. \tag{6.19}$$

Two powers of c_H find their way into the denominator because the normalization of each half-sound carries an $\omega_k^{-1/2} = (ck)^{-1/2}$.

We can now integrate to find Q,

$$Q = \sum_{kk'} n(k_0)n(k'_0)(k_0 + k'_0)\Gamma(k, k') = \frac{1}{V}\int V\text{đ}^3k\, V\text{đ}^3k' \frac{c_H(k + k')\Gamma(k, k')}{(e^{\beta c_H k} - 1)(e^{\beta c_H k'} - 1)}. \tag{6.20}$$

Since Γ is proportional to V^{-1}, we can see that the emissivity is volume (and thus, we expect, regularization) independent. This integral may also be simplified dramatically without approximation, but may be executed entirely with a simple approximation that relies on the smallness of c_H. This program is carried out in Appendix E. The result is

$$Q = \frac{2048}{99\pi^5}\left(\pi^{10} - 93555\zeta(11)\right)\frac{G_F^2 \sin^4\theta_{\text{W}}}{M^2 c_H^7 \beta^{11}}. \tag{6.21}$$

where ζ is the Riemann zeta function. We reemphasize that $Q \propto c_H^{-7}$ is a nontrivial enhancement that cannot be deduced from simple dimensional analyses. For a complete accounting of the powers of c_H, see Appendix E.

The Q we have computed represents how much power a bulk of nuclear-condensed helium radiates into a single neutrino flavor per unit volume. Since there are three light flavors that couple to the Z equally, we see that the total neutrino emissivity is

$$Q = \frac{2048}{33\pi^5}\left(\pi^{10} - 93555\zeta(11)\right)\frac{G_F^2 \sin^4\theta_{\text{W}}}{M^2 c_H^7 \beta^{11}} \approx 9.5\frac{G_F^2 \sin^4\theta_{\text{W}}}{M^2 c_H^7 \beta^{11}}. \tag{6.22}$$

6.1.3 Half-Sound and White Dwarf Cooling

Understand whether the annihilation of half-sound quasiparticles into neutrino radiation is competitive with the other major radiative mechanism—photoemission from the surface—is not exactly straightforward. The issue is that the the neutrino emissivity is a per-unit-volume quantity while the photon emissivity is a per-unit-area quantity. Thus, we need to compare the corresponding luminosities, and not the production rates directly. Moreover, the photoemission depends on the temperature of the surface while the neutrino emission depends on the temperature of the core as well as the density (through its dependence on $c_H = m_A/m_s$). Therefore, to get a feel for the importance of the half-sound annihilation we need a stellar model that can connect these parameters and allow us to compute the respective luminosities.

We will use the simplest stellar model which gives qualitatively correct answers and is quantitatively reasonable but is incorrect in many details. Such a model consists of a large isothermal, degenerate, and highly heat-conducting core surrounded by a thin envelope of non-degenerate matter. It is well-known that if radiative heat transport dominates over convection one can use a free gas equation of state for the degenerate electrons and Kramer's opacity law for the envelope to obtain the relation[120, 121]

$$\frac{L_\gamma}{L_\odot} = \left(\frac{T}{7 \cdot 10^7 \mathrm{K}}\right)^2 \left(\frac{M}{M_\odot}\right) \tag{6.23}$$

where L_γ and $L_\odot$ are the luminosities of the star and the sun, respectively, T is the core temperature, and M and $M_\odot$ represent the masses of the star and the sun, respectively. Such a model is called a Mestel model[120]. The photon luminosity is

not the naïvely expected blackbody T^4 because to make a fair comparison with the neutrino luminosity we re-express everything in terms of the core temperature; it does indeed reflect a fourth-power dependence on the surface temperature.

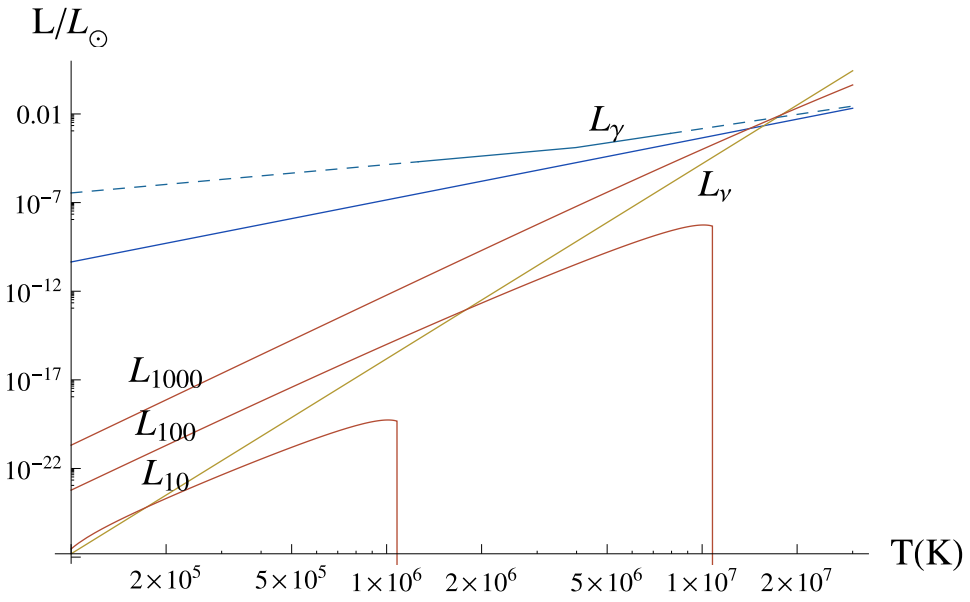

Figure 6.2: Various luminosities for a HeWD with $M = 0.406 M_\odot$. The blue L_γ lines are those from (6.23) and the linear extrapolation of the model in Reference [122] (the extrapolated region is dashed). The yellow L_ν line is to guide the eye: it represents the neutrino luminosity for a star with physically-unrealistic constant density so that it simply represents the T^{11} behavior. The red L_C stars are our results if the critical temperature is fixed as in (4.10) by C=10, 100, or 1000 respectively. This figure is reproduced from Reference [5].

For specificity we will consider a HeWD with $M = 0.406 M_\odot$, which allows us to use results for the photoemission calculated in Reference [122]. In Figure 6.2 we show the simplest Mestel luminosity (6.23) and the luminosity curve from that reference in blue; the dashed lines are linearly extrapolated from the temperature

regime where Reference [122] provides computations. One can see that the two blue curves are at least qualitatively similar, so that the Mestel luminosity dependence T^2 is qualitatively affirmed by more detailed models.

With those electromagnetic luminosities in hand, we now need only to compute the neutrino luminosities for the same star. This requires coarse knowledge of the stellar structure; hydrostatic equilibrium implies

$$\frac{1}{r^2}\frac{d}{dr}\left(\frac{r^2}{\rho}\frac{dP}{dr}\right) = -4\pi G_N \rho \tag{6.24}$$

where G_N is Newton's gravitational constant, P the pressure, ρ the mass density, and r the distance from the star's center. Since the degenerate electrons totally dominate the pressure we can simply use their equation of state,

$$P = \frac{1}{24\pi^2} k_{\mathrm{F}} \left(2k_{\mathrm{F}}^2 - 3m^2\right)\sqrt{k_{\mathrm{F}}^2 + m^2} + \frac{1}{8\pi^2} m^4 \operatorname{arcsinh}\frac{k_{\mathrm{F}}}{m}, \tag{6.25}$$

which is derived in Appendix F, where k_{F} should be thought of as representing the local density ρ.

Solving (6.24) with P given by (6.25) gives a density profile for the star. Knowing the density at all radii in turn lets us compute Q everywhere. We should only consider densities where we are in the regime of condensation for a given temperature. Thus, we pick up a minimum and maximum radius, which are set by the densities at which we form a Coulomb crystal or a classical plasma, respectively. That is, relating the density to the interparticle spacing we know that only the radii between r_{min} and r_{max} given by

$$T_{\mathrm{C}}\left(\frac{a_0}{\ell(r_{\mathrm{max}})}\right) = T = T_{\mathrm{melt}}\left(\frac{a_0}{\ell(r_{\mathrm{min}})}\right) \tag{6.26}$$

will radiate neutrinos. That the star is isothermal helped simplify this constraint; without that fact we would need to consider temperature profiles as well.

We can finally calculate the luminosity by integrating the emissivity against the density profile over the radii where we expect a nuclear condensate. Using

$$L_\nu = \int_{r_{\min}}^{r_{\max}} 4\pi r^2 \mathrm{d}r \, Q(r,T) \tag{6.27}$$

where we emphasize that Q depends on the radius, because c_H depends on the density. Because the condensation temperature T_{C} is uncertain and might potentially be large we show luminosity curves for C =10, 100, and 1000 as red curves labelled as L_C in Figure 6.2. Those curves represent a competition between the sensitive dependence of Q on the temperature and the fact that if the temperature is higher, the $r_{\max}$ is smaller, and there is less volume where condensate exists: the precipitous drops represent the temperatures where the there is no condensate at all.

The two important temperatures T_{melt} and T_{C} determine, as functions of density, where Q has support. This introduces uncertainties into the calculation. The uncertainties in T_{melt} are discussed around (4.5); it is safe to say assume that it is no more than 10% uncertain. Since (6.22) and (5.33) imply

$$Q \propto \rho^{-7/2}, \tag{6.28}$$

the region where there is possibly a transition to a crystalline core is at higher densities and is also suppressed volumetrically, we expect it to be relatively unimportant whether we use the true $r_{\min}$ or 0.

The uncertainties introduced by an undetermined C, however, are much more dramatic. Again, the dependence of Q on ρ means that regions further from the stel-

lar core will radiate energy faster. Add to this effect that larger radii are enhanced volumetrically, and it is clear that a good estimate of the critical temperature $T_{\rm C}$ (or the coefficient C) is extremely important. This importance is made clear by the red curves in Figure 6.2: increase C by a factor of 10 and the neutrino luminosity L_ν increases by a factor of about 10^4. In Chapter 7 we will present evidence that suggests C is of order 1, so that the neutrino emission is not competitive with the photoemission.

As an academic exercise, we should nonetheless point out that in addition to the uncertainties in C, each curve carries additional theoretical uncertainties. First, we used the zero-temperature, low-momentum dispersion relation for the half-sound quasiparticles, which certainly develops corrections when $T \gtrsim m_A$. Note that m_A is $2.1 \cdot 10^6$K for a_0/ℓ=30 and $4.6 \cdot 10^6$K when a_0/ℓ=50. Moreover, we defined $r_{\rm max}$ to be when T became $T_{\rm C}$ (through the critical temperature's density dependence); we therefore know we cannot trust the dispersion relation in the outer regions that we claimed made important contributions to the neutrino luminosity.

In general one expects finite temperature corrections to lower m_A, which would reduce c_H, *increasing* the neutrino luminosity. If the transition from the condensed phase to the plasma phase is first order m_A will change discontinuously and then this enhancement should be negligible. In contrast, if the transition is second order there will be a region where m_A is small, c_H would become arbitrarily small in the region where its temperature is near T_C, offering a huge enhancement to the luminosity.

In Chapter 7 we will show that it seems likely that although C small, the phase transition sequence is peculiar: evidence suggests that there is a first-order phase

transition with $T < T_{\rm Bose}$ where the nuclei go from mostly-condensed (and thus a large m_A) to barely-condensed (and a small m_A), followed by a second-order phase transition at $T_{\rm Bose}$ where the nuclei go from barely-condensed to totally uncondensed. If this is truly the case, whether or not neutrino emission is important should be recomputed with finite-temperature effects taken into account, especially the region where m_A is small, as it implies that there could be a tremendous enhancement of the neutrino emissivity Q.

6.2 Specific Heat

As discussed in the beginning of this chapter, one expects a bulk of nuclear condensate to have a much smaller specific heat than the classical plasma or Coulomb crystal, and such a small specific heat has potentially observable consequences that may include the sudden dimming of stars that is a tempting explanation of the dearth of observed HeWDs in NGC 6397.

In this section we compute the specific heat of the nuclear condensate at low temperatures. The specific heat in the plasma phase, the crystalline phase, and the nuclear condensate phase all have a contribution from the electron-hole excitations in the degenerate electrons. That contribution, per ion, is

$$c_v^e = Z^{1/3} \left(\frac{\pi}{3}\right)^{2/3} \frac{\mu_e}{n^{2/3}} T \approx 0.19 \sqrt{1 + \frac{m^2}{k_{\rm F}^2}} \left(\frac{\ell}{a_0}\right) \left(\frac{T}{10^6 {\rm K}}\right), \tag{6.29}$$

which is quite small. In fact, it is so small that it may be considered sub-dominant compared to the specific heat of the ions in the plasma phase

$$c_v^{\rm plasma} = \frac{3}{2} \tag{6.30}$$

and the specific heat of the lattice phonons in the crystalline phase, which is[123]

$$c_v^{\text{lattice}} = \frac{16\pi^4}{5}\left(\frac{T}{\theta_D}\right)^3 = \frac{16\pi^4}{15\sqrt{3}}\frac{1}{Z^3}\left(\frac{M}{m}\right)^{3/2}\left(\frac{a_0}{\ell}\right)^{-9/2}\left(\frac{T}{\alpha^2 m}\right)^3 \tag{6.31}$$

$$\approx 1.5\cdot 10^8\left(\frac{a_0}{\ell}\right)^{-9/2}\left(\frac{T}{10^6\text{K}}\right)^3 \tag{6.32}$$

as long as $T \ll \theta_D$, where the Debye temperature θ_D is the same as what we call m_A.

In contrast, the specific heat of the ions will dominate over the specific heat of the half-sound, while at low temperatures the massive plasmon and transverse photons are suppressed and may be ignored, so that the electron contribution to the specific heat, c_v^e will be an important contribution.

Let us compute the specific heat of a gas of free half-sound quasiparticles now. The calculation is straightforward:

$$c_v^H = \frac{1}{n}\frac{d\epsilon}{dT} = \frac{1}{n}\frac{d}{dT}\int \text{đ}^3 p\,\frac{c_H p}{e^{c_H p/T}-1} = \frac{1}{n}\frac{2\pi^2}{15 c_H^3}T^3 \tag{6.33}$$

using the dispersion relation $p_0 = c_H p$. We can massage this relation and eliminate c_H by (5.33), finding

$$c_v^H = \frac{Z\alpha^{3/2}}{\pi^{3/2}}c_v^{\text{lattice}} \approx 3.4\cdot 10^4\left(\frac{a_0}{\ell}\right)^{-9/2}\left(\frac{T}{10^6\text{K}}\right)^3, \tag{6.34}$$

Which is obviously smaller than c_v^{lattice} due to the factors of α.

The specific heats are shown in Figure 6.3 for a temperature $5\cdot 10^5$. It is clear that the effect of the condensation are dramatic even for the perhaps-unrealistically-high temperature $1\cdot 10^6$K, shown in Figure 6.3c, for the majority of astrophysically relevant densities the specific heat of the half-sound is less than that of the electrons; at even higher temperatures the half-sound contribution can become dom-

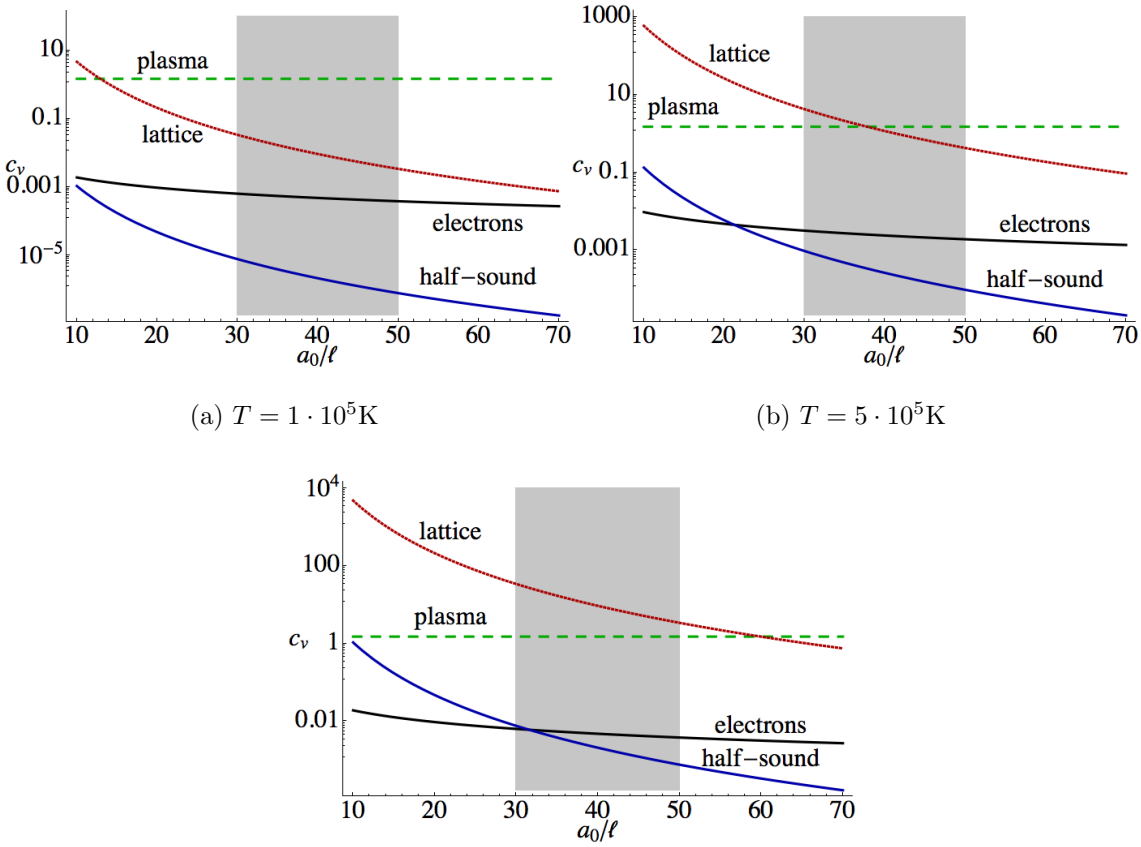

(a) $T = 1 \cdot 10^5$K

(b) $T = 5 \cdot 10^5$K

(c) $T = 1 \cdot 10^6$K

Figure 6.3: The specific heat of a gas of half-sound quasiparticles (blue), degenerate electrons (black), and what the specific heat *would be* were the system in the crystalline (dotted red) or classical plasma (dashed green) phases at sampling of temperatures. The gray band denotes astrophysically relevant densities.

inant. More important, though, is that Figure 6.3 makes it apparent just how drastically the specific heat is reduced if the nuclei are condensed.

Although calculated without knowledge of the half-sound mode, References [66], [68] and [67] calculate a numerically similar specific heat for the nuclear condensate. As discussed in the beginning of this chapter, that the phase with small specific heat is interposed between two phases with high specific heat has potentially observable consequences: alterations to the cooling curve compared to a situation where there is no condensate[67, 115, 86]. It is unclear whether this difference could be observed with current telescopes.

⋆ ⋆ ⋆

This concludes the discussion of two potentially observable astrophysical signatures that helium white dwarfs might exhibit if the nuclear condensate indeed exists: an altered specific heat, which would change the low-temperature cooling curve, and a neutrino emissivity, the relevance of which strongly depends on the thermodynamics of the condensed phase–the condensation temperature, and transition type, in particular. In the next Chapter we will investigate this phase's thermodynamics and present some puzzling results that suggest an unusual sequence of phase transitions between the totally condensed phase and the uncondensed phase, but that nonetheless suggests the critical temperature T_{C} is small so that the alteration of the cooling curve by neutrino radiation is totally and utterly irrelevant.

Chapter 7

Thermodynamics

Whether the half-sound annihilation into neutrino radiation is phenomenologically relevant is quite sensitive to to the critical condensation temperature $T_{\rm C}$, as demonstrated by Figure 6.2. Higher condensation temperatures make this potential channel more relevant.

As discussed in Chapter 4, this critical temperature is quite uncertain. Repulsive interactions are expected to raise[84] the critical temperature above $T_{\rm Bose}$, the condensation temperature of a free Bose gas, given in (4.8). Expressing the critical temperature $T_{\rm C}$ as

$$T_{\rm C} = C T_{\rm Bose}, \tag{7.1}$$

the scaling arguments given in that chapter suggest $C = [4\pi\zeta(3/2)/3]^{2/3} \approx 4.92$, while more detailed estimates[68] suggest $C = [2\pi/3]^{5/3}[2\zeta(3/2)]^{2/3} = 10.3$ which is supported by calculations in Reference [83]. However the then-unknown half-sound was not included in those calculations. In this chapter we develop an estimate of $T_{\rm C}$ that avoids this shortcoming, in an attempt to settle the question of the observational relevance of the half-sound annihilation process. We will broadly follow the discussion in Reference [6]; all of the figures in this chapter are modified versions, to one degree or another, of the figures in that work.

We will compute the one-loop effective potential for the system, and try to

use it to extract the critical temperature. Computing the effective potential involves summing over all energies and integrating over all momenta. Unfortunately, in a complete analysis of the system of degenerate electrons and nonrelativistic nuclei that step would require an extremely difficult calculation that not only incorporates the limits of the polarization tensor given in (5.23), (5.24), and (5.25) but the complete structure, including the branch cuts (which yield Friedel oscillations). To alleviate this calculational difficulty we will assume that the whole effect of the electrons is simply the screening of the Coulomb force with screening mass m_s, ie. we let $\Pi = m_s^2$.

It should be emphasized that this replacement is quite extreme: the electrons respond instantaneously, while with the realistic polarization tensor the electrons have inertia. The effect of this replacement on the spectrum is to change the gap of the plasmon to simply m_A^2, instead of $m_A^2 + (4\alpha Zn)/\mu_e$ as given in (5.27), which we will show in Section 7.1. Due to this approximation our investigation applies to any nonrelativistic charged spin-0 bosons interacting via a screened Coulomb (ie. a Yukawa) interaction. Interestingly, this simply-stated model is not well-characterized in the literature.

7.1 Effective Potential

If the v that minimizes the effective potential is not zero at a given temperature, then we know that at that temperature the nuclei will be condensed and the electromagnetic U(1) will be broken. Let us compute the effective potential now.

It is well-known[124, 125, 126, 127, 128, 129] that the unitary parameterization

$$\psi = (v + h)e^{i\phi} \tag{7.2}$$

that we used to deduce the spectrum in Chapter 5 surprisingly yields the incorrect phase transition temperature, presenting what is known as the unitary-gauge puzzle. To avoid confronting this difficulty we instead use the parameterization

$$\psi = v + h_R + ih_I \tag{7.3}$$

where the R and I subscripts denote the real and imaginary pieces, respectively.

Moreover, as briefly mentioned in Chapter 5, the effective potential is a gauge-dependent quantity[124]. The gauge fixing used there to eliminate as many linear mixings as possible involved the condensate v. Because the whole point of studying the effective potential is to examine the temperature dependence of v, it seems inappropriate to compute the effective potential in a gauge that itself depends on v: we would be computing it in different gauges at different values of v, possibly introducing fictitious dependences.

Instead, we will fix the Coulomb gauge

$$\mathcal{L}_{\text{Coulomb}} = -\frac{1}{2\xi}\left(\nabla \cdot \mathbf{A}\right)^2 \tag{7.4}$$

followed by $\xi \to 0$. The slight calculational inconvenience is worth the conceptual clarity that we get from picking a v-independent gauge.

We use the Euclidean-space action and integrate out the electrons in a matter directly analogous to Chapter 5. In momentum space the resulting action is, to

quadratic order

$$S_{\text{quadratic}} = \int \text{đ}^4 p \begin{pmatrix} h_R(-p) & h_I(-p) & A_0(-p) & A^{\parallel}(-p) \end{pmatrix} \times \tag{7.5}$$
$$\begin{pmatrix} -\frac{\mathbf{p}^2}{2M} + \mu & ip_0 & Zev & 0 \\ -ip_0 & -\frac{\mathbf{p}^2}{2M} + \mu & 0 & \frac{iZevp}{2M} \\ Zev & 0 & \frac{\mathbf{p}^2+\Pi}{2} & -\frac{p_0}{2p}(\mathbf{p}^2+\Pi) \\ 0 & -\frac{iZevp}{2M} & -\frac{p_0}{2p}(\mathbf{p}^2+\Pi) & \frac{1}{2}\left(-\frac{Z^2e^2v^2}{M} + p_0^2 - \frac{\mathbf{p}^2}{\xi} + \frac{p_0^2\Pi}{p^2}\right) \end{pmatrix} \begin{pmatrix} h_R(p) \\ h_I(p) \\ A_0(p) \\ A^{\parallel}(p) \end{pmatrix},$$

where we have omitted the uncoupled $A^{\perp}$ sector. The inverse of the big matrix in (7.5) is the propagator; the propagator will have zeroes where that matrix has vanishing eigenvalues. The eigenvalues themselves are $p_0 \pm iE_p$ where

$$E_p^2 = \frac{\mathbf{p}^4 - 2M\mathbf{p}^2\mu - 2Mm_A^2\mu\xi}{\mathbf{p}^4 + 4m_A^2\mathbf{p}^2\xi - 2Mm_A^2\mu\xi}\left(\frac{\mathbf{p}^2}{2M}\left(\frac{\mathbf{p}^2}{2M} - \mu\right) + \frac{\mathbf{p}^2 m_A^2}{\mathbf{p}^2+\Pi}\right) \tag{7.6}$$
$$\xrightarrow{\xi\to 0} \left(\frac{\mathbf{p}^2}{2M} - \mu\right)^2 + \left(\frac{\mathbf{p}^2}{2M} - \mu\right)\frac{2Mm_A^2}{\mathbf{p}^2+\Pi}, \tag{7.7}$$

which reproduces the familiar (5.20) for the tree-level $\mu = 0$ (which is indeed the value we used in Chapter 5).

The one-loop part of the effective potential $V^{(1)}$ can then be computed in the usual fashion.

$$V^{(1)} = \frac{1}{2}T\sum_{p_0}\int \text{đ}^3 p \ln\left(p_0^2 + E_p^2\right) = \int \text{đ}^3 p \frac{1}{2}E_p + T\int \text{đ}^3 p \ln\left(1 - e^{-\beta E_p}\right) \tag{7.8}$$

where $\beta = 1/T$. We show the formal manipulation giving the final result in Appendix G. This calculation required us to cleanly do the sum over $p_0 = 2\pi T j$, with integer j; this sum is only known if we pick $\Pi = m_s^2$.

Note that the effective potential cleanly breaks into a temperature-independent piece, which is simply the zero-point energy of the modes, and a temperature-

dependent piece. The temperature-independent piece is simply the zero-temperature one-loop correction effective potential, and is thus down compared to the tree-level piece,

$$V^{(0)} = -\mu v^2, \tag{7.9}$$

in the loop expansion, while the finite-temperature piece can be of arbitrary size depending on the temperature T. Since it must be small compared to the $V^{(0)}$ we ignore the temperature-independent piece of $V^{(1)}$.

7.2 Phase Diagram

The effective potential that sets the size of the condensate v is

$$V = V^{(0)} + V^{(1)} = -\mu v^2 + T \int \text{đ}^3 p \ln\left(1 - e^{-\beta E_p}\right); \tag{7.10}$$

the minimization of V with respect to v gives us the expectation value of the condensate at a fixed value of the chemical potential μ. However, in astrophysical situations the density is fixed by the density of electrons, so instead of a fixed chemical potential we would prefer to work with a fixed ion density n which neutralizes the charge of the electrons. We can perform a Legendre transformation to trade μ by n, to get the free energy F

$$F(v, n, T) = V(v, T) + \mu n \tag{7.11}$$

in which case we must simultaneously solve the equations

$$\frac{dF}{d\mu} = 0 \text{ or } \quad n = -\frac{\partial V}{\partial \mu} = v^2 + \int \text{đ}^3 p \; \frac{1}{e^{\beta E_p} - 1} \frac{1}{E_p} \left[\frac{\mathbf{p}^2}{2M} - \mu + \frac{M m_A^2}{\mathbf{p}^2 + m_s^2} \right], \tag{7.12a}$$

$$\frac{dF}{dv} = 0 \text{ or } \quad 0 = \quad \frac{\partial V}{\partial v} = -\mu v + v \int \text{đ}^3 p \; \frac{1}{e^{\beta E_p} - 1} \frac{1}{E_p} \left(\frac{\mathbf{p}^2}{2M} - \mu \right) \frac{4\pi Z^2 \alpha}{\mathbf{p}^2 + m_s^2} \tag{7.12b}$$

where the first terms are the tree-level terms and the integral terms come from the one-loop contribution. These relations reduce, in the absence of dynamical electrons and screening (ie. if $\Pi = m_s^2 = 0$), to those first derived in Reference [130]. Note that it is easy to pick out the tree-level relations

$$n = v^2 \quad \text{and} \quad \mu = 0, \tag{7.13}$$

and that deriving the first requires us to keep μ general and not substitute the tree-level values until after we have differentiated.

The relations in (7.12) have some subtle properties. In particular, the μ-determining second equation can be resolved for μ, and indicates that μ cannot possibly be negative if v is finite, so it is natural to expect that μ is positive. This expectation is somewhat problematic, because at positive μ the quantity E_p^2 given by (7.7) can take negative values, generating a complex 1-loop effective potential contribution (and complex contributions to the equations (7.12) themselves).

This sounds absolutely disastrous, but is actually not so bad. Complex effective potentials are relatively common and signal an instability[132] that can often be fixed by a resummation of higher loop effects[124]. However, even without resumming, the one-loop potential can contain information about the thermodynamics of the system under consideration[124], as happens in this model. Let us now extract what we can from the equations in (7.12).

If the condensate vanishes then (7.12a) becomes

$$n = \int \text{đ}^3 p \, \frac{1}{e^{\beta(\frac{p^2}{2M} - \mu)} - 1} = \frac{1}{2\pi^2}(2MT)^{3/2} \cdot \frac{\sqrt{\pi}}{4} \text{Li}_{\frac{3}{2}}\left(e^{\mu/T}\right) \tag{7.14}$$

where $\text{Li}_{\frac{3}{2}}$ is a standard polylogarithm function. That function has a branch cut for

real arguments greater than one, which corresponds to the limit $\mu \to 0$ from below, at which point it cannot be consistent to claim $v = 0$ any longer. Taking that limit gives

$$n = \left(\frac{MT}{2\pi}\right)^{3/2} \zeta\,(3/2) \tag{7.15}$$

which when solved for the critical temperature T unsurprisingly matches T_{Bose} as in (4.8). The temperature T_{Bose} is as small as possible while still admitting the required limit; negative chemical potentials allow for $v = 0$ solutions at all higher temperatures. The $v = 0$ uncondensed line is shown along the axis in Figure 7.1.

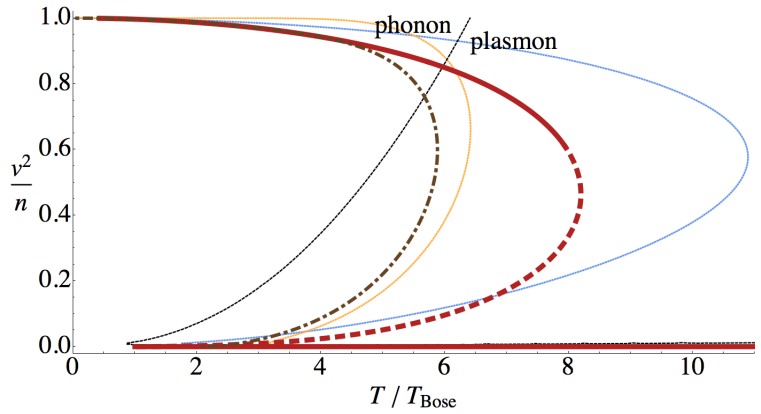

Figure 7.1: The phase diagrams assuming $a_0/\ell = 35$ and $\mu \ll \frac{\mathbf{p}^2}{2M}$ for only phonons (blue dotted line), only plasmons (orange dotted line), both phonons and plasmons (brown dot-dashed line),and the numerical solution (thick red line, which is dashed where that assumption fails).

Without a strategy for handling the complex effective potential, this is as much as we can say. All of the difficulties stem from finite μ, which can make E_p^2 finite. However, if we can make the approximation

$$\mu \ll \frac{\mathbf{p}^2}{2M} \tag{7.16}$$

then E_p^2 becomes

$$E_p^2 = \left(\frac{\mathbf{p}^2}{2M}\right)^2 + \frac{\mathbf{p}^2 m_A^2}{\mathbf{p}^2 + m_s^2} \tag{7.17}$$

which is nonnegative and the difficulty disappears. We therefore make this assumption, determining *a posteriori* the values of T and v for which it is justified, and attempt to solve the equations in (7.12) numerically and to investigate various limits analytically. Those equations simplify to

$$n - v^2 = \int \text{đ}^3 p \, \frac{1}{e^{\beta E_p} - 1} \frac{1}{E_p} \left[\frac{\mathbf{p}^2}{2M} + \frac{M m_A^2}{\mathbf{p}^2 + m_s^2}\right], \tag{7.18a}$$

$$\mu = \int \text{đ}^3 p \, \frac{1}{e^{\beta E_p} - 1} \frac{1}{E_p} \left(\frac{\mathbf{p}^2}{2M}\right) \frac{4\pi Z^2 \alpha}{\mathbf{p}^2 + m_s^2}, \tag{7.18b}$$

So that we can then check the validity of the $\mu \ll \mathbf{p}^2/2M$ approximation by computing μ via the second equation and comparing to the typical $\mathbf{p}^2/2M$ that contributes to the integral in the first equation.

However, since we know that there are two different kinds of quasiparticles, the plasmon and the half-sound phonon, we expect that for some temperatures and densities the integral in (7.18a) should have two typical momenta that contribute: one for each mode. One example of such a doubly-humped integrand is shown in Figure 7.2.

The numerical solution of (7.18) for $a_0/\ell = 35$ is shown as the thick red line in Figure 7.1, dashed where the negligible μ approximation fails, as we will show. That curve suggests that the condensation transition is first order. For temperatures in below T_{Bose} and above roughly $8T_{\text{Bose}}$ there is but one solution, which *should* therefore be globally stable. For intermediate temperatures, however, three solutions exist, the almost-totally-condensed and totally-uncondensed are locally stable while

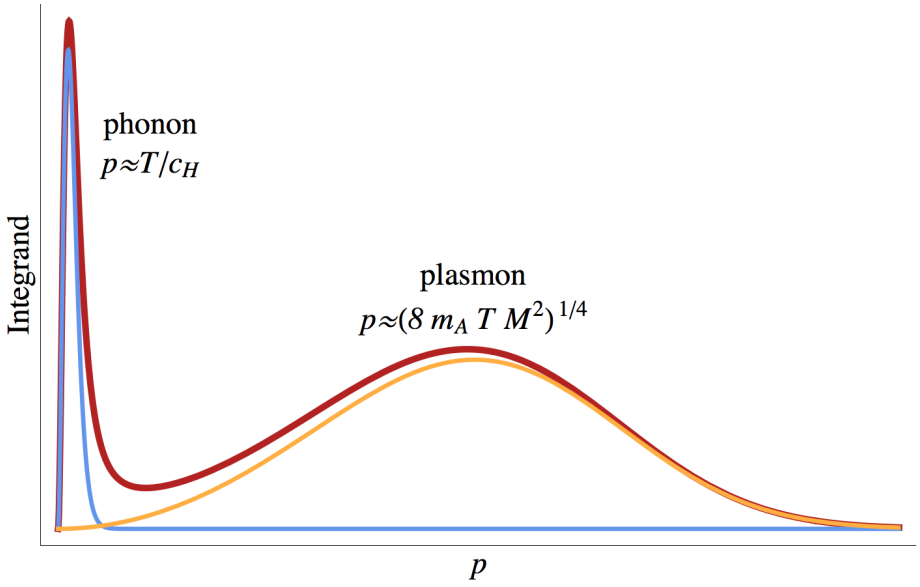

Figure 7.2: One potential integrand as a function of momentum. The thick red line is the full numerical integrand, while the dotted blue and dotted orange lines represent the half-sound and plasmon approximations, respectively.

the middle solution is unstable.

Of the two locally stable solutions only one can be the global ground state. Which solution plays that role is decided by the free energy F: whichever has the lower F will be globally stable. We will investigate global stability in Section 7.3, and find evidence for a more complicated phase diagram than the numerical solution neglecting μ suggests.

Let now us try to characterize the phonon and plasmon regimes separately.

The phonon region is given by

$$E_p \approx c_H p \tag{7.19}$$

which can be derived from (7.17) by letting

$$p^2 \ll m_s^2 \quad \text{and} \quad \left(\frac{\mathbf{p}^2}{2M}\right)^2 \ll c_H^2 p^2. \tag{7.20}$$

With the phonon dispersion relation, one can calculate the required integrals in (7.18). The results are

$$n = v^2 + \frac{M m_s}{12 m_A} T^2, \tag{7.21a}$$

$$\mu = \frac{Z^2 \pi^3}{15} \frac{\alpha m_s^3}{M} \frac{T^4}{m_A^5}. \tag{7.21b}$$

The resulting relation between v and T is shown as a dotted blue line in Figure 7.1.

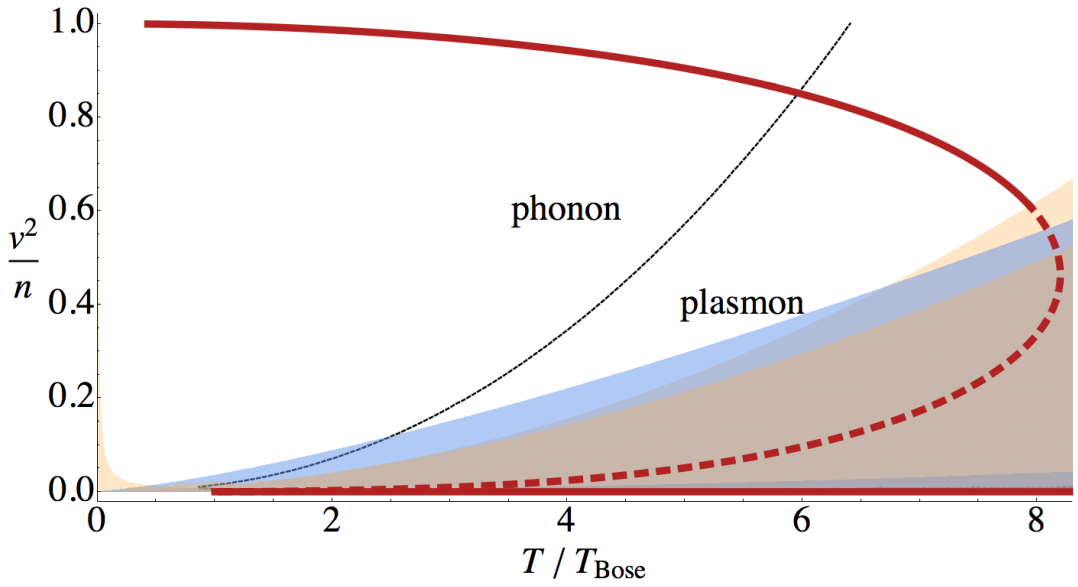

Figure 7.3: The numerically-computed phase diagram, with shaded regions where various approximations break down. Blue regions represent phonon approximations while orange regions represent plasmon approximations.

We can now check the various approximations that yielded these—the phonon—results. Note that the required integrals are cut off by a Boltzmann factor $\exp(-c_H p/T)$,

so that the momentum scale is set by T/c_H. Using this value of p reduces both approximations in (7.20) to

$$T \ll m_A \tag{7.22}$$

The region where this approximation fails is shown in dark blue in Figure 7.3. The requirement that μ be negligible so that E_p^2 is positive,

$$\mu \ll \frac{p^2}{2M} \qquad \text{translates, with } p = T/c_H, \text{ to} \qquad \frac{Z^2\pi^3}{15}\alpha m_s \frac{T^2}{m_A^3} \ll 1. \tag{7.23}$$

This region is the lighter blue region that covers most of where the numerical solution is dashed in Figure 7.3. We can see from that figure that this requirement is the more severe restriction for the validity of the phonon results.

The plasmon region is characterized by the approximations

$$m_s^2 \ll \mathbf{p}^2 \tag{7.24a}$$

$$\left(\frac{p^2}{2M}\right)^2 \ll m_A^2 \tag{7.24b}$$

and the dispersion relation has a gap

$$E_p^2 = \left(\frac{\mathbf{p}^2}{2M}\right)^2 + m_A^2, \tag{7.25}$$

as expected. Here we see the violence that simply using $\Pi = m_s^2$ inflicts as the cost for calculational tractability: the gap of this plasmon differs from the gap given by the full polarization function in (5.27). Whereas with the full polarization tensor the electrons also oscillate so that it is the reduced mass m_{red} that sets the gap, if they are totally rigid it is the ion mass. So, in this model the gap is much larger than it is in the more realistic case.

Using these approximations, the statistical factor in the integrals in (7.18) cut the integral off via a factor

$$e^{-E_p/T} \approx e^{-\frac{m_A}{T}} e^{-\frac{\mathbf{p}^4}{8M^2 m_A T}} \tag{7.26}$$

so that the typical momentum is set by $\mathbf{p}^2 \approx \sqrt{8 m_A T M^2}$ or equivalently

$$\frac{\mathbf{p}^2}{2M} = \sqrt{2 m_A T}. \tag{7.27}$$

Again those integrals may be done analytically, yielding

$$n = v^2 + \frac{\Gamma(5/4)}{2^{1/4}\pi^2} M^{3/2} m_A^{5/4} T^{1/4} e^{-m_A/T}, \tag{7.28a}$$

$$\mu = \frac{2^{1/4}\Gamma(3/4)}{\pi} Z^2 \alpha \sqrt{M} \frac{T^{3/4}}{m_A^{1/4}} e^{-m_A/T}. \tag{7.28b}$$

The resulting relation between v^2 and T is plotted as the dotted orange line in Figure 7.1.

We can now check the assumptions that led to *these*—the plasmon—results. The three approximations reduce to

$$m_s^2 \ll \mathbf{p}^2 \quad \Rightarrow \quad \frac{m_s^4}{8M^2 m_A^2} \ll T, \tag{7.29a}$$

$$\left(\frac{\mathbf{p}^2}{2M}\right)^2 \ll m_A^2 \quad \Rightarrow \quad T \ll \frac{1}{2} m_A, \tag{7.29b}$$

$$\mu \ll \frac{\mathbf{p}^2}{2M} \quad \Rightarrow \quad \frac{Z^2\Gamma(3/4)}{2^{1/4}\pi} \frac{\sqrt{M} T^{1/4}}{m_A^{3/4}} \alpha \; e^{-m_A/T} \ll 1. \tag{7.29c}$$

The first of these restrictions breaks down for small T and small v^2, and shaded orange in the lower-left hand corner of Figure 7.3. The latter two of these break down in similar regions, despite their wildly different appearances, because of the dominating exponential suppression by m_A/T in the last approximation. These are

also shown shaded in orange, and invalidate much of the numerical curve far from $v^2 = n$.

It is now clear why we draw the numerical curve in Figure 7.1 dashed below $v^2 \approx 0.6$: in those regions neglecting μ compared to $\mathbf{p}^2/2M$ is a poor approximation and we expect the complex nature of the effective potential to invalidate the calculations we have done, so that in that regime some resummation is required to extract sensible results. In other words, our $\mu \ll \mathbf{p}^2/2M$ approximation that rendered the effective potential nonnegative is a good approximation outside of the shaded curves in Figure 7.3.

Finally, we can incorporate both humps into the calculation of the phase diagram. That is, we can take both the phonon-regime and plasmon-regime one-loop contribution to (7.18). Simply reading off the one-loop pieces from (7.21a) and (7.28a) we arrive at the relation

$$n = v^2 + \frac{Mm_s}{12m_A}T^2 + \frac{\Gamma(5/4)}{2^{1/4}\pi^2}M^{3/2}m_A^{5/4}T^{1/4}e^{-m_A/T} \tag{7.30}$$

which is valid (in the negligible-μ sense) as long as it remains outside of both the phonon and plasmon breakdown regions in Figure 7.3. The curve specified by this relationship is shown as the brown dot-dashed line in Figure 7.1. We see that this curve reproduces the numerical solution for temperatures as high as roughly $4T_{\text{Bose}}$, whereas the phonon and plasmon curves only match the numerical answer as far as 1 or $2T_{\text{Bose}}$.

By taking the ratio of the two one-loop contributions in (7.30) we can come up with an idea of whether the effective potential is dominated by phonons or plasmons.

That ratio is

$$\frac{\text{one-loop phonon part}}{\text{one-loop plasmon part}} = \frac{2^{1/4}\pi^2}{12\ \Gamma(5/4)} \frac{m_s T^{7/4}}{\sqrt{M} m_A^{9/4}} e^{m_A/T}; \tag{7.31}$$

where that ratio is 1 is represented by dashed black curve in both Figure 7.1 and Figure 7.3. As indicated on those plots, the phonon piece dominates in the condensed region until $T \approx 5T_{\text{Bose}}$, when the plasmons become dominant. There is also a small region where the phonons dominate near the $v^2 = 0$ axis (ie. where $m_A^2 = 0$), where the denominator blows up.

The phase diagrams shown are all for the density set by astrophysically-sensible a_0/ℓ=35. The dependence on this parameter is relatively mild. Since according to (5.26) the screening mass m_s scales like $k_{\text{F}}^{1/2}$, while k_{F} itself scales like a_0/ℓ, changing this parameter is relatively innocuous, although (7.31) shows that increasing that density parameter tends to shrink the phonon-dominated region.

It therefore seems unlikely, simply from looking at the relevant temperatures in Figure 7.1 and Figure 7.3 that the critical temperature could possibly be much larger than roughly $11T_{\text{Bose}}$ in the most optimistic circumstances (looking simply at the phonon curve), while a presumably more reliable estimate is roughly $8T_{\text{Bose}}$ (from the numerical curve). Taking these phase diagrams seriously suggests that there is a first-order transition and that optimistically C is of order 10, so the neutrino emission from half-sound annihilation is dramatically uncompetitive with the photoemission from the surface of a star, as shown in Figure 6.2.

To nail down the critical temperature of the transition, we should try to deduce the temperature at which the free energies F of the condensed phase and uncon-

densed phase are equal. We pursue this question in the next section, and come upon a logical conundrum, and pose a conjecture which would resolve this problem.

7.3 Global Stability and a Conjecture

Up to now we have determined local minima of the free energy F. To determine the global minimum, we must compare those minima's free energies. We compute the free energy from (7.11)

$$F(v, n, T) = V(v, T) + \mu n \tag{7.32}$$

for the locally stable solutions to (7.12) at a given temperature and fixed density. Since we know the condensate v for these solutions, we can think of F there as simply a function of n and T, while if we wanted to know F for an out-of-equilibrium v we would need the full v-dependent function. At a given temperature, whichever locally stable solution has a lower free energy is the global ground state, and the transition temperature is defined by the temperature at which the two local minima switch roles: the global minimum becomes merely metastable and the metastable state becomes the global minimum.

The standard expectation is that at T_{Bose}, the condensed phase must be the global minimum, because for lower temperatures the uncondensed phase does not exist. This means that the transition temperature should be T_{Bose} or higher, and that the free energy of the uncondensed solution at T_{Bose} should be greater than the free energy of the condensed phase. Let us check this expectation now.

It is simple to compute the free energy for the uncondensed phase, because

right at T_{Bose} it has $\mu = 0$. When in the uncondensed region, v and m_A vanish, so that E_p is simply $\mathbf{p}^2/2M$. The integral in (7.10) may be done exactly:

$$F_{v=0}\left(n, T_{\text{Bose}}\right) = T_{\text{Bose}} \int \text{đ}^3 p \ \ln\left(1 - e^{-\mathbf{p}^2/2MT_{\text{Bose}}}\right) \tag{7.33}$$

$$= -\zeta(5/2) T_{\text{Bose}} \left(\frac{MT_{\text{Bose}}}{2\pi}\right)^{3/2} \approx -0.33 \frac{1}{M\ell^5}. \tag{7.34}$$

Since T_{Bose} is in the phonon-dominated regime, it we can compare this free energy to the free energy in the phonon approximation. Using (7.21) we compute

$$F_{\text{phonon}}\left(n, T\right) = \mu\left(n - v^2\right) + T \int \text{đ}^3 p \ \ln\left(1 - e^{-c_H p/T}\right) \tag{7.35}$$

$$= \frac{\pi^3 Z^2}{180} \frac{\alpha}{c_H^4 m_A^2} T^6 - \frac{\pi^2}{90 c_H^3} T^4. \tag{7.36}$$

We can evaluate this at T_{Bose} and plug in the $v^2 = n$ to estimate the free energy. The result is

$$F_{\text{phonon}}\left(n, T_{\text{Bose}}\right) = -\frac{3^{1/6}\pi^{7/3}}{5\ 2^{1/3}\zeta^{8/3}(3/2) Z^{5/2}} \frac{1}{M l^5} \left(\frac{m}{M}\right)^{3/2} \left(1 - \frac{3^{1/6}\pi^{4/3}}{2\zeta^{4/3}(3/2) Z^{5/6}} \sqrt{\frac{m}{M}}\right),$$

$$= -0.04 \left(\frac{m}{M}\right)^{3/2} \frac{1}{M\ell^5} \left(1 - 0.14\sqrt{\frac{m}{M}}\right) \tag{7.37}$$

which is less negative than the uncondensed free energy by factors of the mass ratio $(m/M)^{3/2} \approx 10^{-6}$, which makes the phonon free energy essentially negligible compared to the uncondensed free energy.

That the free energy of the phonons at T_{Bose} is much less negative than the free energy of the uncondensed phase at that temperature represents a tremendous logical problem, and stands in stark contrast to the typical first order phase transition. It implies that at all temperatures where the uncondensed state can possibly exist (ie. temperatures greater than T_{Bose}) it is the global minimum. Numerical calculations performed with the $\mu = 0$ dispersion relation confirm this result.

Usually, by the time the temperature is as low as T_{Bose}, F_{phonon} will be more negative than $F_{v=0}$. That is, the $v \neq 0$ minimum of the function $F(v, n, T)$ is below the $v = 0$ minimum. While the extrema of the unresummed free energy are physically meaningful, unfortunately we cannot know the full function $F(v, n, T)$ without a resummation that resolves the issue of complex effective potential.

In spite of this limitation it is obvious that as we change T continuously, there is no way for a global minimum to simply vanish, as the $v = 0$ seems to: it must first become a local minimum.

Put another way: at $T = 0$ the condensed phase is the global minimum, and an uncondensed phase is impossible. Now, consider raising the temperature to just below T_{Bose}. Again, the condensed phase is the only permissible phase: the uncondensed phase suggested in Figure 7.1 is not even *locally* stable. Now raise the temperature to T_{Bose}, and notice that just as the uncondensed phase becomes physically possible (that is, becomes a *local* minimum) it *also* becomes the *global* minimum—and a deep global minimum, at that. Surely no smooth function has this behavior.

Instead the true phase diagram must be more complicated. The simplest conceptually problem-free phase diagram is shown in Figure 7.5. By introducing a barely-condensed phase below T_{Bose}, we introduce the logical possibility that the phase transition is not the typical first-order transition. If the barely-condensed phase develops at some low temperature and becomes the global minimum before T_{Bose}, so that there is a first-order transition, then the fact that $F_{v=0}$ is the global minimum compared to F_{phonon} at T_{Bose} poses no problem: that minimum began its

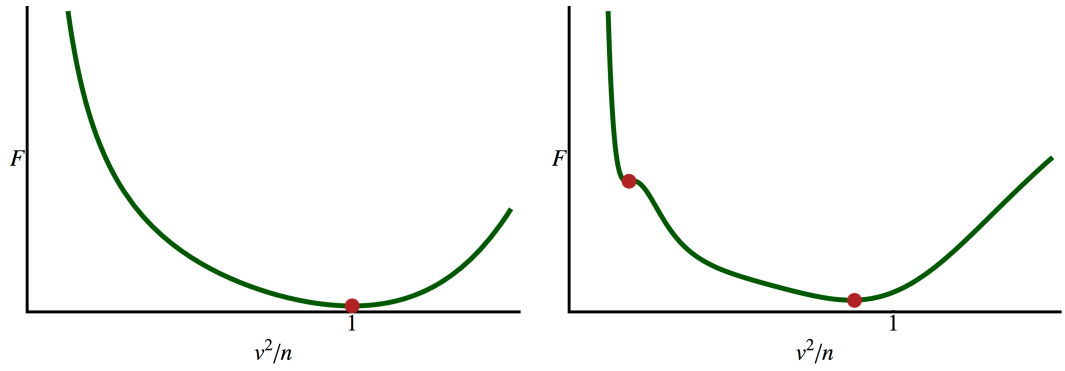

(a) Condensed phase only

(b) A barely-condensed phase develops

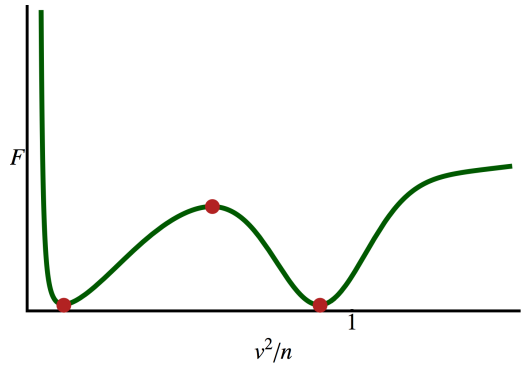

(c) First-order transition occurs

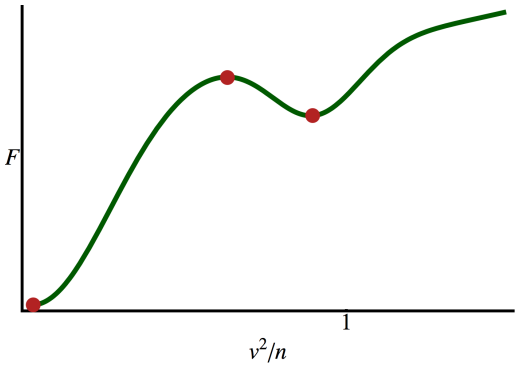

(d) Second-order transition occurs at T_{Bose}: totally uncondensed phase possible

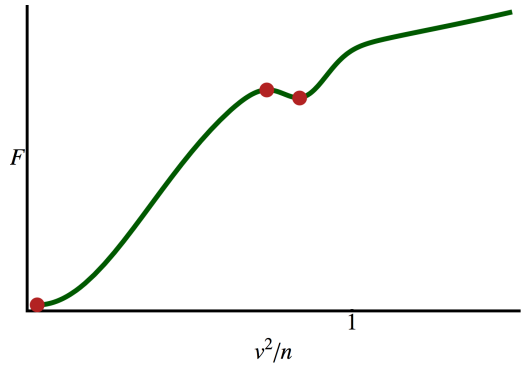

(e) Condensed phase very shallow

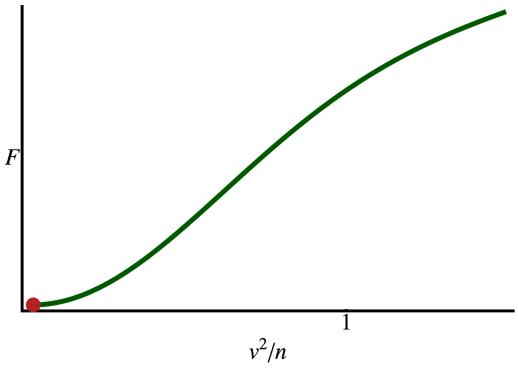

(f) Condensation impossible

Figure 7.4: The green curves represent slices of $F(v, n, T)$ at temperatures shown in Figure 7.5 that could remove the logical conundrum that $F_{v=0}(n, T_{\text{Bose}})$ is much more negative than $F_{\text{phonon}}(n, T_{\text{Bose}})$. The red points in these figures are the extrema of $F(v, n, T)$ that compose the red curve in that phase diagram.

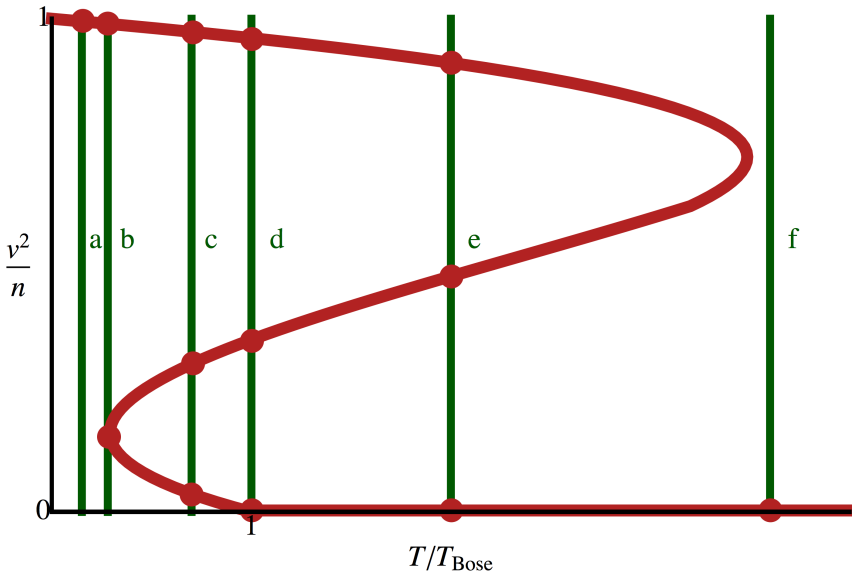

Figure 7.5: A hypothetical problem-free phase diagram. Each vertical green line corresponds to a temperature (and subfigure) in the phase transition sequence shown in Figure 7.4, while each red dot corresponds to a local minimum or maximum (or inflection point, in case b) on that F-as-a-function-of-v curve which one can extract from the effective potential without resumming.

existence as a disfavored local minimum and the transition to the totally uncondensed phase can be second-order. An example of a free energy $F(v, n, T)$ that accomplishes such a sequence is shown for illustrative purposes in Figure 7.4; the subfigures there correspond to the temperatures indicated in Figure 7.5.

One might ask: rather than believe in this more complicated phase diagram, might it be that the free energies we computed are simply misleading, and that a proper resummed effective potential might alleviate this problem? We answer this in the negative: even though the full effective potential is complex and thus requires resumming if we wish to know it as a function of v, the extrema (that is, the red curve

in Figure 7.5 and the red dots in Figure 7.4) should be valid without resumming[124]. The extra twist which allows the barely-condensed phase at $T < T_{\rm Bose}$ can occur in regions where the calculations we performed are out of theoretical control (in the shaded regions in Figure 7.3). Of course, the curve might make any complicated shape in that region—we have simply shown the simplest such shape that resolves the tension created by the fact that the uncondensed free energy is much lower than condensed free energy. Because those calculations are under control, we seem forced to believe in this unusual sequence of phase transitions.

$\star$ $\star$ $\star$

To summarize, in this chapter we have investigated a model with totally rigid electrons. That model is simply the realistic nuclear condensate phase but with a polarization tensor $\Pi = m_s^2$ instead of the true, complicated, function, limits of which are shown in (5.23), (5.24), and (5.25). The spectrum of this model supports both plasmons and gapless phonons (like the half-sound in the realistic spectrum), and has a simply calculated effective potential.

Extracting physical information from that effective potential required us to approximate $\mu \ll \mathbf{p}^2/2M$ to eliminate complexities; the calculation is out of theoretical control in the shaded regions of Figure 7.3. This is actually *fortunate*, because if the whole numerical curve were trustable, we would be unable to resolve the seemingly-paradoxical fact that $F_{v=0}$ is a much deeper free energy well than $F_{\rm phonon}$ (or, indeed, the numerical calculation of F) at $T_{\rm Bose}$. Put another way, if we could do a totally-trustable calculation, we would not find a paradox in the first

place!

The resolution of this paradox seems to be that the phase transition from a totally condensed phase to a totally uncondensed phase is quite unusual compared to the standard condensation transition: instead of a single first order transition at some temperature greater than T_{Bose}, the matter in this model cools, uncondensed, all the way down to T_{Bose}, at which point there is a second-order transition to a phase with a small condensate. As that substance continues to cool, at some temperature less than T_{Bose} there is a first-order transition to a totally-condensed state.

If we took some totally condensed bulk and began heating it up, the totally condensed phase would be metastable until $T \approx 8T_{\text{Bose}}$ (the highest temperature of the numerical curve in Figure 7.1), but at any point this superheated condensate could flash boil. That $T \approx 8T_{\text{Bose}}$ agrees nicely with the results in Figure 3 of Reference [83], despite the absence of screening (and therefore, necessarily, a gapless region in the dispersion relation) in the model examined there. This agreement makes sense, because the high temperature regime is well into the plasmon-dominated region, where the screening is irrelevant.

Summary and Outlook

In this Part we have investigated what happens to matter at densities much higher than atomic densities but simultaneously much lower than nuclear densities. For large enough densities, we have argued that there should be a temperature regime where the nuclear Coulomb crystal cannot yet exist yet the nuclei are close enough together to form a Bose-Einstein condensate.

We demonstrated that this phase has, in addition to the familiar and expected massive plasmon and transverse photons, a gapless mode, which we call the half-sound. We showed that the specific heat of a gas of half-sound quasiparticles is very low (so that for a large range of relevant temperatures, the dominant contribution is provided by the electrons). The ease with which such a dramatic drop in the specific heat is observable is an as-yet unsettled question[67, 86, 115].

We calculated the cross-section of two half-sound phonons annihilating into neutrinos, and showed that this process will only be competitive with surface photoemission if the critical condensation temperature was much, much larger than the critical temperature of a free Bose gas. While investigating the critical temperature of a similar model (with unrealistic, perfectly rigid electrons), we found that the critical temperature would only be roughly $8T_{\text{Bose}}$; if the critical temperatures of the model with responsive electrons and rigid electrons are similar, then this means the heat of a helium white dwarf lost to neutrino radiation is incredibly small.

It would be interesting to properly handle dynamic, responsive electrons with a realistic polarization tensor (and not simply take $\Pi = m_s^2$). The difficulty of such a calculation is entirely in one step: computing the effective potential, where the full

analytic structure of $\Pi\left(p_0, \mathbf{p}^2\right)$, including the cuts (Friedel oscillations), is included. In particular, it would be interesting to see if such a calculation automatically produced a phase diagram with an extra twist, so that the conundrum discussed in Section 7.3 is resolved in the conjectured manner.

If there is indeed a barely-condensed phase at low temperatures, it would be interesting to understand its quasiparticle spectrum, and to perform a reduction analogous to that performed in Section 6.2. Since the neutrino emissivity in that case scaled like c_H^{-7} and $c_H \propto m_A \propto v^2$, one might anticipate a tremendous enhancement of neutrino emission at *low* temperatures instead of high temperatures. Whether the scaling of the emissivity with c_H carries over into the barely-condensed phase is unknown.

While we discussed the metastability of the condensed phase for temperatures less than roughly $8T_{\text{Bose}}$, we did not estimate the timescale over which such a superheated condensate might release its energy. To fully characterize this violent boiling and rapid change of the condensate v, one needs to know the potential barrier between the two states. That is, one needs to know the full function $F(v, n, T)$ and not just its values at the locally stable values of v that fix the curve in Figure 7.1.

All of these potentially interesting calculations require an understanding of the resummation needed to cure the effective potential of its complexities. Developing this resummation for the more realistic polarization tensor is an ambitious undertaking—resolving the issues for merely the model with totally rigid electrons seems quite difficult, yet much more approachable than the full (and more interesting), and nonetheless interesting theoretically.

Finally there are a few other interesting calculations that suggest themselves.

The first is to repeat these calculations for deuterium. Since it is spin-1, these calculations should be slightly more difficult technically, but precisely the same conceptually. Because it is lighter than helium and has half the atomic number, we expect the condensed phase to happen at even lower densities than those in HeWDs: perhaps it will be clear that the condensed phase is important to the dynamics of brown dwarfs or inertial confinement experiments.

It may also be interesting to consider the role that contact interactions between the helium nuclei, which we neglected, play for the dynamics of the half-sound. In particular, it would be interesting to try to estimate the rate at which the helium nuclei fuse. Such pycnonuclear fusion may be surprisingly enhanced by the screening of the usual impediment to fusion: the Coulomb barrier. It may be worthwhile to investigate how much faster fusion might occur with a shielded, short-range force in lieu of long-range electromagnetism.

Much about this condensed phase remains unknown and is ripe for investigation.

Appendices & Bibliography

Appendix A

Dimensionless Functions for CFL+K^0 Vortons

We here collect the dimensionless functions f that arise in Chapter 3.

$$f_1(x) = \frac{2\pi}{e} I_1(x) \tag{A.1}$$

$$f_2 = -\frac{2\pi v}{e^2(1+v)}\Big(I_0(vm_\gamma\delta)I_1(m_\gamma\delta) + I_0(m_\gamma\delta)I_1(vm_\gamma\delta) + (1+v)m_\gamma\delta I_1(m_\gamma\delta)I_1(vm_\gamma\delta)\log(R/\delta)\Big) \tag{A.2}$$

$$f_3(x) = \frac{\pi}{e^2}\left(I_0(x)I_1(x) + xI_1^2(x)\log(R/\delta)\right) \tag{A.3}$$

$$f_4 = \pi f^2\left(1-\left(\frac{m_{sd}}{\mu_{sd}}\right)^2\right)\left(\frac{1}{2}\left(R^2-\delta^2\right)\mu_{sd} - w^2v^2\log(R/\delta)\right) \tag{A.4}$$

$$f_5 = 4\pi\delta^2\left(m_sm_u + m_d(m_s+m_u)\sqrt{1-\left(\frac{m_\gamma}{fe}\right)^2}\right) + 4\pi(R^2-\delta^2)\left(m_dm_s + m_u(m_d+m_s)\left(\frac{m_{sd}}{\mu_{sd}}\right)\right) \tag{A.5}$$

$$f_6 = -\frac{\pi^2 vm_\gamma\delta}{3\ e^2} I_1(m_\gamma\delta)I_1(vm_\gamma\delta) \tag{A.6}$$

$$f_7 = \frac{\pi^2\ m_\gamma\delta}{2\ e^2} I_1(m_\gamma\delta)^2 \tag{A.7}$$

$$f_8 = \frac{\pi^2\ vm_\gamma\delta}{48\ e^2} I_1(vm_\gamma\delta)^2 \tag{A.8}$$

The difference between f_7 and f_8, aside from the factors of v that are associated with $\tilde{k}_0$, is the dimensionless factor that arises from the fact that the magnetic field is a dipole and not a monopole like the electric field.

Appendix B

Toroidal Coordinates

The toroidal coordinates $\{u, v, \phi\}$ form an axially-symmetric orthogonal coordinate system that are particularly natural for describing toroidal phenomena. They are related to the usual Cartesian coordinates by

$$\begin{aligned} \frac{x}{a} &= \frac{\sinh v \cos\phi}{\cosh v - \cos u} & u &= -2\,\mathrm{Im}\left[\operatorname{arccoth}\frac{\sqrt{x^2+y^2}+iz}{a}\right] \\ \frac{y}{a} &= \frac{\sinh v \sin\phi}{\cosh v - \cos u} & v &= 2\,\mathrm{Re}\left[\operatorname{arccoth}\frac{\sqrt{x^2+y^2}+iz}{a}\right] \\ \frac{z}{a} &= \frac{\sin u}{\cosh v - \cos u} & \phi &= \phantom{-2\,\mathrm{Re}\,}\arctan\frac{y}{x} \end{aligned} \tag{B.1}$$

where a is the radius of the *reference circle*, the circle that is described by $v = \infty$ (or equivalently, $z = 0$ and $x^2 + y^2 = a^2$), and should be thought of as completely fixed.

We pick the fundamental domain so that the coordinates conventionally obey

$$u \in (-\pi, \pi], \quad v \in [0, \infty), \quad \text{and} \quad \phi \in (-\pi, \pi]. \tag{B.2}$$

The coordinate ϕ is the same as in familiar cylindrical coordinates, and specifies a semi-infinite plane that terminates on the z-axis.

A surface of constant u is the sphere that contains the reference circle and is centered at $z = a \cot u$; such a sphere has radius $a\,|\csc u|$.

A surface of constant v is a torus with

$$R = a \coth v \quad \text{and} \quad \delta = a\,\mathrm{csch}\, v \tag{B.3}$$

where δ is the radius of the tube and R is the distance of the center of the tube to the origin.

The relation (B.3) can be inverted so that a specific torus of radius R and thickness δ is a surface of constant v in a coordinate system with

$$a^2 = R^2 - \delta^2, \tag{B.4}$$

in which case the torus is the surface described by

$$v_{\text{torus}} = \operatorname{arcsinh} \sqrt{(R/\delta)^2 - 1}. \tag{B.5}$$

The Laplacian in these coordinates is

$$\begin{aligned} a^2\nabla^2 = &\operatorname{csch} v \left(\cosh v - \cos u\right)^3 \\ &\times \left[\partial_u \left(\frac{\sinh v}{\cosh v - \cos u}\partial_u\right) + \partial_v \left(\frac{\sinh v}{\cosh v - \cos u}\partial_v\right) + \partial_\phi \left(\frac{\operatorname{csch} v}{\cosh v - \cos u}\partial_\phi\right)\right]. \end{aligned} \tag{B.6}$$

Perhaps surprisingly, Laplace's equation is separable in spite of such a complicated differential operator. Unfortunately, and perhaps unsurprisingly, the Helmholtz equation is *not* separable, so that determining the electromagnetic fields of a charged, current-carrying torus of finite size is an extremely difficult task to accomplish analytically.

Appendix C

The Polarization Tensor In Non-relativistic Situations

General arguments require that the polarization tensor $\Pi^{\mu\nu}$ satisfy the Ward-Takahashi identity,

$$p_\mu \Pi^{\mu\nu}(p) = 0, \tag{C.1}$$

in order to maintain gauge invariance.

A privileged frame (the rest frame of some bulk, say, relative to which a chemical potential might be defined) can be specified by a four-vector n^μ which points in that frame's time direction. If we work in that frame,

$$n^\mu = (1, 0, 0, 0). \tag{C.2}$$

We can use n^μ to build a projection operator $N^{\mu\nu}$,

$$N^{\mu\nu} = g^{\mu\nu} - n^\mu n^\nu \tag{C.3}$$

that satisfies $N^{\mu\nu} n_\nu = 0$ and $N^\nu{}_\alpha N^{\alpha\mu} = N^{\nu\mu}$.

We can then build two Lorentz scalars: a temporal part $p_0 = p_\mu n^\mu$, and a 3-vector part $-\mathbf{p}^2 = p_\mu N^{\mu\nu} p_\nu$. The usual Lorentz scalar $p^2 = p_\mu p^\mu$ is simply the sum $p_0^2 - \mathbf{p}^2$.

Let us build the most general symmetric Lorentz-invariant tensor out of the available ingredients: the tensor $g^{\mu\nu}$, the 4-vectors p^μ and n^μ and the scalars p_0 and

$\mathbf{p}^2$. The most general form is

$$\Pi^{\mu\nu} = A\,p^\mu p^\nu + B\,n^\mu n^\nu + C\,(p^\mu n^\nu + n^\mu p^\nu) + D\,g^{\mu\nu} \tag{C.4}$$

where A, B, C, and D are any function of p_0 and $\mathbf{p}^2$.

For the polarization tensor we additionally have the Ward-Takahashi identity $p_\mu \Pi^{\mu\nu} = 0$. This implies

$$0 = A\,p^2\,p^\nu + B\,p_0\,n^\nu + C\left(p^2\,n^\nu + p_0\,p^\nu\right) + D\,p^\nu. \tag{C.5}$$

Because this equality must hold for any independent n^ν and p^ν we can separate this equality into two:

$$0 = A\,p^2 + C\,p_0 + D \tag{C.6}$$

$$0 = B\,p_0 + C\,p^2; \tag{C.7}$$

these two constraints can be used to eliminate two of the four general functions A, B, C, and D.

One particularly convenient way to use these constraints is to eliminate B and D so that

$$\Pi^{\mu\nu} = A\left(p^\mu p^\nu - p^2 g^{\mu\nu}\right) + C\left(p^\mu n^\nu + p^\nu n^\mu - \frac{p^2}{p_0} n^\mu n^\nu - p_0 g^{\mu\nu}\right) \tag{C.8}$$

and to substitute

$$A = \frac{p_0^2}{\mathbf{p}^4}\Pi + \Pi^\perp \quad \text{and} \quad C = \frac{p_0 p^2}{\mathbf{p}^4}\Pi - p_0\Pi^\perp \tag{C.9}$$

So that we can write

$$\Pi^{\mu\nu} = \begin{pmatrix} \Pi & \frac{p^i p_0}{\mathbf{p}^2}\Pi \\ \frac{p^i p_0}{\mathbf{p}^2}\Pi & \frac{p^i p^j p_0^2}{\mathbf{p}^4}\Pi + \left(p^i p^j - \delta^{ij}\mathbf{p}^2\right)\Pi^\perp \end{pmatrix}. \tag{C.10}$$

If we adopt the notational convention $p_i = p^i$ (so that we think of any explicit 3-vector as living in a Euclidean space with a positive metric) then

$$\Pi_{\mu\nu} = \begin{pmatrix} \Pi & -\frac{p_i p_0}{\mathbf{p}^2}\Pi \\ -\frac{p_i p_0}{\mathbf{p}^2}\Pi & \frac{p_i p_j p_0^2}{\mathbf{p}^4}\Pi + (p_i p_j - \delta_{ij}\mathbf{p}^2)\,\Pi^{\perp} \end{pmatrix}, \tag{C.11}$$

as in (5.6).

Appendix D

The Annihilation Probability $\Gamma(k, k')$

While calculating the neutrino emissivity Q we needed to evaluate the annihilation amplitude per unit volume per unit time $\Gamma(k, k')$, which in (6.18) is reduced to

$$\Gamma(k,k') = \frac{G_F^2 \sin^4\theta_{\mathrm{W}}}{M^2 V^3} \int V\mathrm{d}^3p\, V\mathrm{d}^3p' (2\pi)^4 \delta^4(p + p' - k - k') \frac{(kk')^2 (p_0 p_0' + \mathbf{p}\cdot\mathbf{p}')}{\omega_k \omega_{k'} \omega_p \omega_{p'}}. \tag{D.1}$$

This appendix reproduces some notes verbatim that were created in preparation for crafting Reference [5] which contain the evaluation of this integral.

It is straightforward to perform the integral over p' using three of the four δ-functions. Substituting the energy of the quasiparticles as $\omega_k = c_H |k|$ and the energy of the neutrinos as the usual relativistic $\omega_p = |p|$ gives

$$\begin{aligned}\Gamma(k,k' = \frac{G_F^2 \sin^4\theta_{\mathrm{W}} kk'}{c_H^2 M^2 V} \int \frac{d^3p}{(2\pi)^3} &\times (2\pi)\delta\left(p + |k + k' - p| - c_H k - c_H k'\right) \\ &\times \left[1 + \frac{\mathbf{p}\cdot(\mathbf{k} + \mathbf{k}' - \mathbf{p})}{p\,|k + k' - p|}\right]\end{aligned} \tag{D.2}$$

where for clarity we suppress any obvious absolute value delimiters. Interestingly, this integral may be evaluated exactly.

Note that for the δ-function to have support, it must be the case that $p \leq c_H(k + k')$. The strategy for evaluating this integral will be to consider the relation

of the $\mathbf{p}$ to the vector $\mathbf{k}+\mathbf{k}'$. Let us define an angle α by

$$\cos\alpha = \frac{\mathbf{p}\cdot(\mathbf{k}+\mathbf{k}')}{p\,|k+k'|}. \tag{D.3}$$

The δ-function implies

$$|k+k'-p| = c_H(k+k') - p \tag{D.4}$$

Squaring both sides allows us to rewrite the left-hand side as the square of the magnitude of a vector, which we can break into constituent pieces. That is,

$$(\mathbf{k}+\mathbf{k}')^2 - 2\mathbf{p}\cdot(\mathbf{k}+\mathbf{k}') + \mathbf{p}^2 = c_H^2(k+k')^2 + \mathbf{p}^2 - 2pc_H(k+k'); \tag{D.5}$$

solving for the cross-term on the LHS leads to

$$\cos\alpha_0 = \frac{|k+k'|^2 + 2pc_H(k+k') - c_H^2(k+k')^2}{2p\,|k+k'|}. \tag{D.6}$$

Here we denote the value of α that satisfies the δ-function α_0. Since the range of cosine is restricted, we can find additional constraints. Implementing $-1 \le \cos\alpha_0$ means

$$|p| \ge \frac{c_H(k+k') - |k+k'|}{2}. \tag{D.7}$$

Implementing $\cos\alpha_0 \le 1$ requires

$$|p|\,(|k+k'| - c_H(k+k')) \ge \frac{|k+k'|^2 - c_H^2(k+k')^2}{2}. \tag{D.8}$$

If the left-hand side is positive, then we conflict with the constraint that $p \le c_H(k+k')$, so we only consider the negative case. These two inequalities are summarized by

$$0 \le \frac{c_H(k+k') - |k+k'|}{2} \le p \le \frac{c_H(k+k') + |k+k'|}{2}. \tag{D.9}$$

The δ-function in the integral may be replaced, according to the usual rules of δ-function manipulation, by

$$\delta(\cos\alpha - \cos\alpha_0)\left|\frac{p - c_H(k+k')}{p\,|k+k'|}\right|. \tag{D.10}$$

Using the identities

$$\mathbf{p}\cdot(\mathbf{k}+\mathbf{k}'-\mathbf{p}) = p\,|k+k'|\cos\alpha - p^2 \tag{D.11}$$

$$|k+k'-p| = \sqrt{|k+k'|^2 + p^2 - 2p\,|k+k'|\cos\alpha}, \tag{D.12}$$

and simplifying $d^3p = 2\pi p^2 dp\; d\cos\alpha$, we can execute the angular integral with the remaining δ-function. We are left with

$$\begin{aligned}\Gamma(k,k') =& \frac{G_F^2\sin^4\theta_{\rm W} kk'}{c_H^2 M^2 V}\theta\big[c_H(k+k') - |k+k'|\,\big]\int\frac{p^2\;dp}{(2\pi)^2}\\ &\times 2\pi\theta\left[p - \frac{c_H(k+k')-|k+k'|}{2}\right]\theta\left[\frac{c_H(k+k')+|k+k'|}{2} - p\right]\\ &\times\frac{|k+k'|^2 - \big(c_H(k+k')-2p\big)^2}{2\,|k+k'|\,p^2}\end{aligned} \tag{D.13}$$

where the Heaviside θs implement the constraints in (D.9). This integral can be done easily. The final answer is

$$\Gamma(k,k') = \frac{G_F^2\sin^4\theta_{\rm W}}{6\pi c_H^2 M^2 V}kk'\,|k+k'|^2\,\theta\Big[c_H(k+k') - |k+k'|\,\Big]. \tag{D.14}$$

Appendix E

Emissivity Integral

Herein we execute the integral in (E.1), which amounts to calculating the neutrino emissivity Q. We wish to evaluate

$$Q = \frac{1}{V}\int V\text{đ}^3k\, V\text{đ}^3k' \frac{c_H(k+k')\Gamma(k,k')}{(e^{\beta c_H k}-1)(e^{\beta c_H k'}-1)}, \tag{E.1}$$

with $\Gamma(k,k')$ given by (D.14). This appendix reproduces some notes verbatim that were created in preparation for crafting Reference [5] which contain the evaluation of this integral, and the first clause of this sentence was taken verbatim from Appendix D.

Let $\cos\eta = \mathbf{k}\cdot\mathbf{k}'/kk'$. Then we have

$$\begin{aligned} Q = {} & \frac{G_F^2 \sin^4\theta_{\mathrm{W}}}{6\pi c_H M^2}\int \frac{d^3k}{(2\pi)^3}\frac{2\pi k'^2 dk'\; d\cos\eta}{(2\pi)^3} \\ & \times \frac{(k+k')kk'\,(k^2+k'^2+2kk'\cos\eta)}{(e^{\beta c_H k}-1)(e^{\beta c_H k'}-1)} \\ & \times \theta\left[c_H(k+k') - \sqrt{k^2+k'^2+2kk'\cos\eta}\right]. \end{aligned} \tag{E.2}$$

Note here that we have gained a power of c from the energy in the numerator. Executing the angular integral leaves

$$\begin{aligned} Q = {} & \frac{G_F^2 \sin^4\theta_{\mathrm{W}}}{192\pi^5 c_H M^2}\int dk\; dk'\; \frac{(k+k')k^2k'^2}{(e^{\beta c_H k}-1)(e^{\beta c_H k'}-1)} \\ & \times \left(c_H^4(k+k')^4 - (k-k')^4\right) \times \theta\left[c_H^4(k+k')^4 - (k-k')^4\right]. \end{aligned} \tag{E.3}$$

Changing variables to $k_\pm = (k \pm k')/2$ transforms this expression into

$$Q = \frac{G_F^2 \sin^4\theta_{\rm W}}{192\pi^5 c_H M^2}\, 2^6 \int_0^\infty dk_+ \int_{-c_H k_+}^{c_H k_+} dk_- \left(c_H^4 k_+^4 - k_-^4\right) \times \frac{k_+ (k_+^2 - k_-^2)^2}{(e^{\beta c_H (k_+ + k_-)} - 1)(e^{\beta c_H (k_+ - k_-)} - 1)} \tag{E.4}$$

where we have put the constraint from the θ-function into the limits of integration of k_-.

We now must approximate. Since $c_H \ll 1$, the bounds on k_- imply $k_- \ll k_+$. However, we cannot neglect terms where k_- is compared to $c_H k_+$, as these quantities are commensurate. Making this approximation we are left with

$$Q \approx \frac{G_F^2 \sin^4\theta_{\rm W}}{3\pi^5 c_H M^2} \int_0^\infty dk_+ \int_{-c_H k_+}^{c_H k_+} dk_- \frac{k_+^5 (c_H^4 k_+^4 - k_-^4)}{\left(e^{\beta c_H k_+} - 1\right)^2}. \tag{E.5}$$

Performing the remaining integrals is simple. The result is

$$Q = \frac{G_F^2 \sin^4\theta_{\rm W}}{3\pi^5 c_H M^2} \int_0^\infty dk_+ \frac{c_H^5 k_+^{10}}{\left(e^{\beta c_H k_+} - 1\right)^2} = \frac{2048}{99\pi^5}\left(\pi^{10} - 93555\zeta(11)\right) \frac{G_F^2 \sin^4\theta_{\rm W}}{M^2 c_H^7 \beta^{11}} \tag{E.6}$$

where ζ is the usual Riemann Zeta function. We emphasize dependence of the power density Q on c, $Q \propto c^{-7}$. This nontrivial dependence arose from -11 powers of c appearing with the temperature, -2 from the dispersion relation $\omega_k = ck$ in the normalization of the modes, $+1$ from the emitted energy, which is proportional to c, and $+5$ from the phase space allotted to this decay. Evaluating the dimensionless constant shows it to be of order 1:

$$\frac{2048}{99\pi^5}\left(\pi^{10} - 93555\zeta(11)\right) = 3.16459\ldots \tag{E.7}$$

Appendix F

Pressure of a Free Fermi Gas

The Fermi energy of a free, relativistic Fermi gas is

$$\epsilon_F = 2\int_0^{k_\mathrm{F}} \mathrm{đ}^3 p\,\sqrt{p^2+m^2} = \frac{1}{8\pi^2}\left(k_\mathrm{F}\sqrt{k_\mathrm{F}^2+m^2}(2k_\mathrm{F}^2+m^2) + m^4 \operatorname{arcsinh}\frac{k_\mathrm{F}}{m}\right) \tag{F.1}$$

while the number density is simply

$$n = 2\int_0^{k_\mathrm{F}} \mathrm{đ}^3 p = \frac{1}{3\pi^2}k_\mathrm{F}^3. \tag{F.2}$$

The pressure is the derivative of the total energy with respect to volume, keeping the total number of particles fixed.

$$P = -\left(\frac{dE}{dV}\right)_N = -\left(\frac{dV\epsilon_F}{dV}\right)_N = -\epsilon_F - V\left(\frac{d\epsilon_F}{dV}\right)_N. \tag{F.3}$$

Eliminating k_F in ϵ_F in favor of V and N through (F.2) and $n = N/V$, executing the derivative, and then re-substituting for n and then k_F, one finds

$$P = \frac{1}{24\pi^2}k_\mathrm{F}\left(2k_\mathrm{F}^2-3m^2\right)\sqrt{k_\mathrm{F}^2+m^2} + \frac{1}{8\pi^2}m^4 \operatorname{arcsinh}\frac{k_\mathrm{F}}{m}. \tag{F.4}$$

Appendix G

Deriving the Useful Form of the 1-Loop Effective Potential

Here we show how to calculate the 1-loop effective potential given in (7.8). We begin with the integral we wish to compute

$$V^{(1)} = \frac{1}{2} T \sum_{p_0} \int \text{đ}^3 p \ \ln\left(p_0^2 + E_p^2\right) \tag{G.1}$$

where the sum is over $p_0 = 2\pi T j$ with integer j. We introduce a spurious offset δ

$$V^{(1)} = \frac{1}{2} T \sum_{p_0} \int \text{đ}^3 p \ \ln\left(p_0^2 + E_p^2 + \delta\right) \Big|_{\delta=0} \tag{G.2}$$

which we may rewrite as an integral

$$V^{(1)} = \int^0 \text{d}\delta \ \frac{d}{d\delta} \frac{1}{2} T \sum_{p_0} \int \text{đ}^3 p \ \ln\left(p_0^2 + E_p^2 + \delta\right). \tag{G.3}$$

Moving the derivative through the momentum integral yields

$$V^{(1)} = \int^0 \text{d}\delta \ \frac{1}{2} T \sum_{p_0} \int \text{đ}^3 p \ \frac{1}{p_0^2 + E_p^2 + \delta}. \tag{G.4}$$

Now we perform the p_0 sum, giving

$$V^{(1)} = \int^0 \text{d}\delta \frac{1}{2} \int \text{đ}^3 p \ \frac{1}{2\sqrt{E_p^2 + \delta}} \coth\left(\frac{1}{2}\beta\sqrt{E_p^2 + \delta}\right). \tag{G.5}$$

We may execute the δ integral:

$$V^{(1)} = T \int \text{đ}^3 p \ \ln\left(2\sinh\left(\frac{1}{2}\beta E_p\right)\right). \tag{G.6}$$

This may be separated cleanly into a temperature-independent piece and a temperature dependent piece:

$$V^{(1)} = \int \text{đ}^3 p \ \frac{1}{2} E_p + T \int \text{đ}^3 p \ \ln\left(1 - e^{-\beta E_p}\right). \tag{G.7}$$

Bibliography

[1] Paulo F. Bedaque, Evan Berkowitz, and Aleksey Cherman. Vortons in dense quark matter. *Phys. Rev. D*, 84(2):023006, Jul 2011, nucl-th/1102.4795.

[2] Paulo F. Bedaque, Evan Berkowitz, Geoffrey Ji, and Nathan Ng. Electron shielding of vortons in high-density quark matter. *Phys. Rev. D*, 85:043008, Feb 2012, nucl-th/1112.1386.

[3] Paulo F. Bedaque, Evan Berkowitz, and Srimoyee Sen. Stable vortex loops in two-species BECs. *Journal of Physics B: Atomic, Molecular and Optical Physics*, 45(22):225301, 2012, cond-mat.quant-gas/1111.4507.

[4] Paulo F. Bedaque, Evan Berkowitz, and Aleksey Cherman. Nuclear condensate and helium white dwarfs. *The Astrophysical Journal*, 749(1):5, 2012, nucl-th/1111.1343.

[5] Paulo F. Bedaque, Evan Berkowitz, and Aleksey Cherman. Neutrino Emission from Helium White Dwarfs with Condensed Cores. *Submitted to Ap.J*, 2012, nucl-th/1203.0969.

[6] Paulo F. Bedaque, Evan Berkowitz, and Srimoyee Sen. Thermodynamics of Nuclear Condensates and Phase Transitions in White Dwarfs. *Submitted to JHEP*, 2012, astro-ph/1206.1059.

[7] Edward Witten. Superconducting Strings. *Nucl.Phys.*, B249:557–592, 1985.

[8] R.L. Davis and E.P.S. Shellard. COSMIC VORTONS. *Nucl.Phys.*, B323:209–224, 1989.

[9] U. Schlöder, H. Engler, U. Schünemann, R. Grimm, and M. Weidemüller. Cold inelastic collisions between lithium and cesium in a two-species magneto-optical trap. *The European Physical Journal D - Atomic, Molecular, Optical and Plasma Physics*, 7:331–340, 1999, physics/9902058.

[10] H. Pu and N. P. Bigelow. Collective excitations, metastability, and nonlinear response of a trapped two-species Bose-Einstein condensate. *Phys. Rev. Lett.*, 80:1134–1137, Feb 1998.

[11] J. Goldwin, S. B. Papp, B. DeMarco, and D. S. Jin. Two-species magneto-optical trap with ^{40}K and ^{87}Rb. *Phys. Rev. A*, 65:021402, Jan 2002, cond-mat/0108287.

[12] J. Ruostekoski and J. R. Anglin. Creating vortex rings and three-dimensional skyrmions in Bose-Einstein condensates. *Phys. Rev. Lett.*, 86:3934–3937, Apr 2001, cond-mat/0103310.

[13] J. Ruostekoski. Stable particlelike solitons with multiply quantized vortex lines in Bose-Einstein condensates. *Phys. Rev. A*, 70:041601, Oct 2004, cond-mat/0408376.

[14] Herman Feshbach. Unified theory of nuclear reactions. *Annals of Physics*, 5(4):357 – 390, 1958.

[15] Herman Feshbach. A unified theory of nuclear reactions. II. *Annals of Physics*, 19(2):287 – 313, 1962.

[16] C. Marzok, B. Deh, C. Zimmermann, Ph. W. Courteille, E. Tiemann, Y. V. Vanne, and A. Saenz. Feshbach resonances in an ultracold ^{7}Li and ^{87}Rb mixture. *Phys. Rev. A*, 79(1):012717, Jan 2009, cond-mat/0808.3967.

[17] Cheng Chin, Rudolf Grimm, Paul Julienne, and Eite Tiesinga. Feshbach resonances in ultracold gases. *Rev. Mod. Phys.*, 82:1225–1286, Apr 2010, cond-mat/0812.1496.

[18] C. Pethick and H. Smith. *Bose-Einstein condensation in dilute gases*. Cambridge University Press, ISBN:9780521665803.

[19] C. M. Savage and J. Ruostekoski. Energetically stable particlelike skyrmions in a trapped Bose-Einstein condensate. *Phys. Rev. Lett.*, 91:010403, Jul 2003, cond-mat/0306112.

[20] Richard A. Battye, N. R. Cooper, and Paul M. Sutcliffe. Stable skyrmions in two-component Bose-Einstein condensates. *Phys. Rev. Lett.*, 88:080401, Feb 2002, cond-mat/0109448.

[21] G. Ferrari, M. Inguscio, W. Jastrzebski, G. Modugno, G. Roati, and A. Simoni. Collisional properties of ultracold K-Rb mixtures. *Phys. Rev. Lett.*, 89:053202, Jul 2002, cond-mat/0202290.

[22] B Marcelis, E. G. M. van Kempen, B. J. Verhaar, and S. J. J. M. F. Kokkelmans. Feshbach resonances with large background scattering length: Interplay with open-channel resonances. *Phys. Rev. A*, 70(1):012701, July 2004, cond-mat/0402278.

[23] T. G. Tiecke. Properties of potassium. *Diploma thesis, van der Waals-Zeeman institute, University of Amsterdam*, 2010.

[24] L Khaykovich, F Schreck, G Ferrari, T Bourdel, J Cubizolles, L. D. Carr, Y Castin, and C Salomon. Formation of a matter-wave bright soliton. *Science*, 296(5571):1290–1293, 2002, cond-mat/0205378.

[25] T W B Kibble. Topology of cosmic domains and strings. *Journal of Physics A: Mathematical and General*, 9(8):1387, 1976.

[26] W. H. Zurek. Cosmological experiments in superfluid helium? *Nature*, 317(6037):505–508, 10 1985.

[27] T.W.B. Kibble. Some implications of a cosmological phase transition. *Physics Reports*, 67(1):183 – 199, 1980.

[28] W.H. Zurek. Cosmological experiments in condensed matter systems. *Physics Reports*, 276(4):177 – 221, 1996, cond-mat/9607135.

[29] Bogdan Damski. The simplest quantum model supporting the Kibble-Zurek mechanism of topological defect production: Landau-Zener transitions from a new perspective. *Phys. Rev. Lett.*, 95:035701, Jul 2005.

[30] Jacek Dziarmaga. Dynamics of a quantum phase transition: Exact solution of the quantum Ising model. *Phys. Rev. Lett.*, 95:245701, Dec 2005, cond-mat/0509490.

[31] A. del Campo, G. De Chiara, Giovanna Morigi, M. B. Plenio, and A. Retzker. Structural defects in ion chains by quenching the external potential: The inhomogeneous Kibble-Zurek mechanism. *Phys. Rev. Lett.*, 105:075701, Aug 2010, 1002.2524.

[32] Chad N. Weiler, Tyler W. Neely, David R. Scherer, Ashton S. Bradley, Matthew J. Davis, and Brian P. Anderson. Spontaneous vortices in the formation of Bose-Einstein condensates. 455(7215):948, Oct 2008, 0807.3323.

[33] J. V. Porto. Private communication, 18 Nov 2010.

[34] A. S. van de Nes and P. Török. Rigorous analysis of spheres in Gauss-Laguerre beams. *Opt. Express*, 15(20):13360–13374, Oct 2007.

[35] Sharon A. Kennedy, Matthew J. Szabo, Hilary Teslow, James Z. Porterfield, and E. R. I. Abraham. Creation of Laguerre-Gaussian laser modes using diffractive optics. *Phys. Rev. A*, 66:043801, Oct 2002.

[36] F. Pampaloni and J. Enderlein. Gaussian, Hermite-Gaussian, and Laguerre-Gaussian beams: A primer. Oct 2004, physics/0410021.

[37] Naoya Matsumoto, Taro Ando, Takashi Inoue, Yoshiyuki Ohtake, Norihiro Fukuchi, and Tsutomu Hara. Generation of high-quality higher-order Laguerre-Gaussian beams using liquid-crystal-on-silicon spatial light modulators. *J. Opt. Soc. Am. A*, 25:1642–1651, 2008.

[38] H. He, M. E. J. Friese, N. R. Heckenberg, and H. Rubinsztein-Dunlop. Direct observation of transfer of angular momentum to absorptive particles from a laser beam with a phase singularity. *Phys. Rev. Lett.*, 75:826–829, Jul 1995.

[39] Evan Berkowitz. Candidacy Paper: Vortons in dense quark matter. Submitted to the UMD Physics Department 8 Apr 2011.

[40] Mark G. Alford. Color superconducting quark matter. *Ann. Rev. Nucl. Part. Sci.*, 51:131–160, 2001, hep-ph/0102047.

[41] Mark G. Alford, Andreas Schmitt, Krishna Rajagopal, and Thomas Schäfer. Color superconductivity in dense quark matter. *Rev. Mod. Phys.*, 80:1455–1515, 2008, hep-ph/0709.4635.

[42] Krishna Rajagopal and Frank Wilczek. The Condensed matter physics of QCD. 2000, hep-ph/0011333. To appear as Chapter 35 in the Festschrift in honor of B.L. Ioffe, 'At the Frontier of Particle Physics / Handbook of QCD', M. Shifman, ed., (World Scientific).

[43] David B. Kaplan and Sanjay Reddy. Novel phases and transitions in quark matter. *Phys. Rev.*, D65:054042, 2002, hep-ph/0107265.

[44] Mark G. Alford, Krishna Rajagopal, and Frank Wilczek. Color flavor locking and chiral symmetry breaking in high density QCD. *Nucl.Phys.*, B537:443–458, 1999, hep-ph/9804403.

[45] D. T. Son and Misha A. Stephanov. Inverse meson mass ordering in color-flavor-locking phase of high density QCD. *Phys. Rev.*, D61:074012, 2000, hep-ph/9910491.

[46] Daniel F. Litim and Cristina Manuel. Photon self-energy in a color superconductor. *Phys. Rev.*, D64:094013, 2001, hep-ph/0105165.

[47] D. T. Son and Misha A. Stephanov. Inverse meson mass ordering in color-flavor-locking phase of high density QCD: Erratum. *Phys. Rev.*, D62:059902, 2000, hep-ph/0004095.

[48] Silas R. Beane, Paulo F. Bedaque, and Martin J. Savage. Meson masses in high density QCD. *Phys. Lett.*, B483:131–138, 2000, hep-ph/0002209.

[49] R. Casalbuoni and Raoul Gatto. Effective theory for color flavor locking in high density QCD. *Phys.Lett.*, B464:111–116, 1999, hep-ph/9908227.

[50] P. F. Bedaque and T. Schäfer. High-density quark matter under stress. *Nuclear Physics A*, 697(3-4):802 – 822, 2002, hep-ph/0105150v3.

[51] Paulo F. Bedaque. Charged kaon condensation in high density quark matter. *Phys. Lett.*, B524:137–143, 2002, nucl-th/0110049.

[52] Max A. Metlitski Kirk B. W. Buckley and Ariel R. Zhitnitsky. Drum vortons in high density QCD. 2002, hep-ph/0212074v2.

[53] D.T. Son. Light Goldstone boson and domain walls in the K^0 condensed phase of high density quark matter. 2001, hep-ph/0108260.

[54] M. Tinkham. *Introduction to superconductivity*. Dover books on physics and chemistry. Dover Publications, ISBN:9780486435039.

[55] L. H. Thomas. The calculation of atomic fields. *Mathematical Proceedings of the Cambridge Philosophical Society*, 23:542–548, 1927.

[56] E Fermi. Un methodo satistico par la determinazione di alcune proprietà dell'atome. *Rend Accad Naz del Lincei cl Sci fis Mat e Nat, 1927, 23 (6)*, pages 602–607, 1927.

[57] Charles Alcock, Edward Farhi, and Angela Olinto. Strange stars. *Astrophys.J.*, 310:261–272, 1986.

[58] F. Weber, C. Kettner, M. K. Weigel, and N. K. Glendenning. Strange-matter stars. In G. Vassiliadis, A. D. Panagiotou, S. Kumar, and J. Madsen, editors, *Strangeness and Quark Matter*, pages 308–317, 1995. LBL-36210, C94-09-01.

[59] K.S. Cheng and T. Harko. Surface photon emissivity of bare strange stars. *Astrophys.J.*, 596:451–463, 2003, astro-ph/0306482.

[60] V.V. Usov, Tiberiu Harko, and K.S. Cheng. Structure of the electrospheres of bare strange stars. *Astrophys.J.*, 620:915–921, 2005, astro-ph/0410682.

[61] Michael McNeil Forbes, Kyle Lawson, and Ariel R. Zhitnitsky. The Electrosphere of Macroscopic 'Quark Nuclei': A Source for Diffuse MeV Emissions from Dark Matter. *Phys.Rev.*, D82:083510, 2010, astro-ph.GA/0910.4541.

[62] A. Abrikosov. *Zh. Eksp. Teor. Fiz.*, 39:1798, 1960.

[63] D. A. Kirzhnitz. *Soviet Phys.-JETP*, 11:365, 1960.

[64] E. E. Salpeter. *ApJ*, 134:669, 1961.

[65] L. G. Althaus and O. G. Benvenuto. Evolution of Helium White Dwarfs of Low and Intermediate Masses. *Astrophys.J*, 477:313–+, March 1997.

[66] Gregory Gabadadze and Rachel A. Rosen. Charged Condensate and Helium Dwarf Stars. *JCAP*, 0810:030, 2008, astro-ph/0806.3692.

[67] Gregory Gabadadze and David Pirtskhalava. Quantum Liquid Signatures in Dwarf Stars. *JCAP*, 0905:017, 2009, hep-th/0904.4267.

[68] Gregory Gabadadze and Rachel A. Rosen. Effective Field Theory for Quantum Liquid in Dwarf Stars. *JCAP*, 1004:028, 2010, hep-ph/0912.5270.

[69] R. R. Strickler, A. M. Cool, J. Anderson, H. N. Cohn, P. M. Lugger, and A. M. Serenelli. Helium-core White Dwarfs in the Globular Cluster NGC 6397. *ApJ*, 699:40–55, July 2009, astro-ph.GA/0904.3496.

[70] Gregory Laughlin, Peter Bodenheimer, and Fred C. Adams. The end of the main sequence. *The Astrophysical Journal*, 482(1):420, 1997.

[71] R. Kippenhahn, K. Kohl, and A. Weigert. Entwicklung in engen Doppelstern systemen II. *Zeitschrift fuer Astrophysik*, 66:58, 1967.

[72] R. Kippenhahn, H.-C. Thomas, and A. Weigert. Entwicklung in engen Doppelsternsystemen V. Thermal Pulses in the White Dwarf Component of a Binary System. *Zeitschrift fuer Astrophysik*, 69:265, 1968.

[73] S. Refsdal and A. Weigert. On the Production of White Dwarfs in Binary Systems of Small Mass. *Astronomy and Astrophysics*, 13:367, August 1971.

[74] R. F. Webbink. Evolution of helium white dwarfs in close binaries. *Monthly Notices of the RAS*, 171:555–568, June 1975.

[75] Marek J. Sarna, Ene Ergma, and Jelena Gerkevit-Antipova. Cooling curves and initial models for low-mass white dwarfs ($< 0.25 M_{\odot}$) with helium cores. *Monthly Notices of the Royal Astronomical Society*, 316(1):84–96, 2000, astro-ph/0002261.

[76] G. Nelemans and T. M. Tauris. Formation of undermassive single white dwarfs and the influence of planets on late stellar evolution. *Astronomy and Astrophysics*, 335:L85–L88, July 1998, astro-ph/9806011.

[77] The Physics arXiv Blog. New particle born inside helium white dwarfs, say physicists. *Technology Review*, 2011. First posted 11 Nov 2011, Retrieved 1 Mar 2013. http://www.technologyreview.com/view/426097/ .

[78] D. Q. Lamb and H. M. van Horn. Evolution of crystallizing pure C-12 white dwarfs. *Astrophys.J*, 200:306–323, September 1975.

[79] G. Chabrier. Quantum effects in dense Coulumbic matter - Application to the cooling of white dwarfs. *Astrophys.J*, 414:695–700, September 1993.

[80] W. L. Slattery, G. D. Doolen, and H. E. DeWitt. Improved equation of state for the classical one-component plasma. *Phys. Rev. A*, 21:2087–2095, Jun 1980.

[81] Guy S. Stringfellow, Hugh E. DeWitt, and W. L. Slattery. Equation of state of the one-component plasma derived from precision monte carlo calculations. *Phys. Rev. A*, 41:1105–1111, Jan 1990.

[82] A.L. Fetter and J.D. Walecka. *Quantum Theory of Many-Particle Systems*. Dover Books on Physics Series. Dover Publications, ISBN:9780486428277.

[83] Rachel A. Rosen. Phase Transitions of Charged Scalars at Finite Temperature and Chemical Potential. *JHEP*, 12:024, 2010, hep-th/1009.0752.

[84] Kerson Huang. Transition Temperature of a Uniform Imperfect Bose Gas. *Phys. Rev. Lett.*, 83:3770–3771, 1999, cond-mat/9904027.

[85] J. A. Panei, L. G. Althaus, and O. G. Benvenuto. Mass-radius relations for white dwarf stars of different internal compositions. *Astronomy and Astrophysics*, 353:970–977, January 2000, astro-ph/9909499.

[86] O.G. Benvenuto and M.A. De Vito. On the occurrence and detectability of Bose-Einstein condensation in helium white dwarfs. *JCAP*, 1102:033, 2011, astro-ph.SR/1102.4813.

[87] D. A. Howell, M. Sullivan, P. E. Nugent, R. S. Ellis, A. J. Conley, D. Le Borgne, R. G. Carlberg, J. Guy, D. Balam, S. Basa, D. Fouchez, I. M. Hook, E. Y. Hsiao, J. D. Neill, R. Pain, K. M. Perrett, and C. J. Pritchet. The type Ia supernova SNLS-03D3bb from a super-Chandrasekhar-mass white dwarf star. *Nature*, 443:308–311, September 2006, astro-ph/0609616.

[88] J. Oliva and N. W. Ashcroft. Theory of the spin-1 bosonic liquid metal: Equilibrium properties of liquid metallic deuterium. *Phys. Rev. B*, 30(3):1326–1335, 1984.

[89] J. Oliva and N. W. Ashcroft. Theory of the spin-1 bosonic liquid metal: Quasiparticle interactions and electrical resistivity in liquid metallic deuterium. *Phys. Rev. B*, 30(9):5140–5149, 1984.

[90] N W Ashcroft. Hydrogen at high density. *Journal of Physics A: Mathematical and General*, 36(22):6137, 2003.

[91] N. W. Ashcroft. Metallic superfluids. *Journal of Low Temperature Physics*, 139(5/6):711–726, June 2005.

[92] Lasha Berezhiani, Gregory Gabadadze, and David Pirtskhalava. Field Theory for a Deuteron Quantum Liquid. *JHEP*, 04:122, 2010, hep-ph/1003.0865.

[93] Paulo F. Bedaque, Michael I. Buchoff, and Aleksey Cherman. The phases of deuterium at extreme densities. *JHEP*, 04:094, 2011, hep-ph/1007.1972.

[94] Leslie Foldy. Charged boson gas. *Phys. Rev.*, 124(3):649–651, 1961.

[95] Keith A. Brueckner. Charged boson gas at high density. *Phys. Rev.*, 156(1):204–206, Apr 1967.

[96] O.K. Kalashnikov and V.V. Klimov. Polarization Tensor in QCD for Finite Temperature and Density. *Sov.J.Nucl.Phys.*, 31:699, 1980.

[97] T. Altherr and U. Kraemmer. Gauge field theory methods for ultradegenerate and ultrarelativistic plasmas. *Astropart.Phys.*, 1:133–158, 1992.

[98] Cristina Manuel. Hard dense loops in a cold nonAbelian plasma. *Phys.Rev.*, D53:5866–5873, 1996, hep-ph/hep-ph/9512365.

[99] J. Kapusta and T. Toimela. Friedel oscillations in relativistic qed and qcd. *Phys. Rev. D*, 37:3731–3736, Jun 1988.

[100] Horacio D Sivak. Friedel oscillations in a relativistic quantum plasma. *Physica A: Statistical Mechanics and its Applications*, 129(2):408–414, 1985.

[101] Gregory Gabadadze and Rachel A. Rosen. Charge screening in a charged condensate. *Nucl. Phys. Proc. Suppl.*, 192-193:172–173, 2009.

[102] Gregory Gabadadze and Rachel A. Rosen. Effective lagrangian and quantum screening in charged condensate. *Journal of Cosmology and Astroparticle Physics*, 2009(02):016, 2009, hep-lat/0811.4423.

[103] Alexander D. Dolgov, Angela Lepidi, and Gabriella Piccinelli. Ferromagnetic properties of charged vector boson condensate. *JCAP*, 1008:031, 2010, astro-ph.CO/1005.2702.

[104] Robert V. Lange. Interaction range, the goldstone theorem, and long-range order in the heisenberg ferromagnet. *Phys. Rev.*, 156:630–631, Apr 1967.

[105] Tomas Brauner. Spontaneous Symmetry Breaking and Nambu-Goldstone Bosons in Quantum Many-Body Systems. *Symmetry*, 2:609–657, 2010, hep-th/1001.5212.

[106] Thomas Cohen. Private communication.

[107] G.S. Guralnik, C.R. Hagen, and T.W.B. Kibble. Global Conservation Laws and Massless Particles. *Phys.Rev.Lett.*, 13:585–587, 1964.

[108] R.V. Lange. Goldstone Theorem in Nonrelativistic Theories. *Phys.Rev.Lett.*, 14:3–6, 1965.

[109] Robert V. Lange. Nonrelativistic Theorem Analogous to the Goldstone Theorem. *Phys.Rev.*, 146:301–303, 1966.

[110] S. C. Vila. Pre-White Evolution. I. *Astrophys.J*, 146:437, November 1966.

[111] M. P. Savedoff, H. M. van Horn, and S. C. Vila. Late Phases of Stellar Evolution. I. Pure Iron Stars. *Astrophys.J*, 155:221, January 1969.

[112] G. S. Kutter and M. P. Savedoff. Evolution of Initially Pure ^{12}C Stars and the Production of Planetary Nebulae. *Astrophys.J*, 156:1021, June 1969.

[113] S. D. Kawaler, D. E. Winget, and C. J. Hansen. Evolutionary period changes in rotating hot pre-white dwarf stars. *Astrophys.J*, 298:752–755, November 1985.

[114] M. S. O'Brien and S. D. Kawaler. The Predicted Signature of Neutrino Emission in Observations of Pulsating Pre-White Dwarf Stars. *Astrophys.J*, 539:372–378, August 2000, astro-ph/0003261.

[115] M.E. Mosquera, O. Civitarese, O.G. Benvenuto, and M.A. De Vito. Bose–Einstein condensation in helium white dwarf stars. I. *Physics Letters B*, 683(2-3):119 – 122, 2010.

[116] Larry Niven and Jerry Pournelle. *The Mote In God's Eye*. Simon and Schuster, ISBN:0-671-21833-6.

[117] Larry Niven and Jerry Pournelle. *The Gripping Hand*. Pocket Books, ISBN:0-671-79573-2.

[118] Michael E. Peskin and Daniel V. Schroeder. *An Introduction to Quantum Field Theory*. Perseus Books, Cambridge, Massachusetts, ISBN:0201503972.

[119] A. Nogga, H. Kamada, and Walter Gloeckle. Modern nuclear force predictions for the alpha particle. *Phys.Rev.Lett.*, 85:944–947, 2000, nucl-th/0004023.

[120] L. Mestel. On the theory of white dwarf stars. I. The energy sources of white dwarfs. 112:583, 1952.

[121] A.C. Phillips. *The physics of stars*. Manchester physics series. Wiley, ISBN:9780471940579.

[122] A.M. Serenelli, L.G. Althaus, R.D. Rohrmann, and O.G. Benvenuto. The ages and colours of cool helium-core white dwarf stars. *Mon.Not.Roy.Astron.Soc.*, 325:607, 2001, astro-ph/0102417.

[123] S.L. Shapiro and S.A. Teukolsky. *Black holes, white dwarfs, and neutron stars: the physics of compact objects*. Physics textbook. Wiley, ISBN:9780471873167.

[124] L. Dolan and R. Jackiw. Symmetry behavior at finite temperature. *Phys. Rev. D*, 9:3320–3341, Jun 1974.

[125] Steven Weinberg. Gauge and global symmetries at high temperature. *Phys. Rev. D*, 9:3357–3378, Jun 1974.

[126] Yoshiaki Ueda. Gauge dependence of masses in gauge theory at finite temperature. *Phys. Rev. D*, 23:1383–1391, Mar 1981.

[127] M. Chaichian, E.J. Ferrer, and V. de la Incera. Unitary gauge and phase transition at finite temperature. *Nuclear Physics B*, 362(3):616 – 640, 1991.

[128] Peter Arnold, Eric Braaten, and Stamatis Vokos. Resolving the unitary gauge puzzle of thermal phase transitions. *Phys. Rev. D*, 46:3576–3586, Oct 1992.

[129] P. F. Kelly, R. Kobes, and G. Kunstatter. Parametrization invariance and the resolution of the unitary gauge puzzle. *Phys. Rev. D*, 50:7592–7602, Dec 1994, hep-ph/9406298.

[130] Alexander L Fetter. Low-temperature properties of a dense charged bose gas. *Annals of Physics*, 60(2):464 – 483, 1970.

[131] Shmuel Nussinov. Private communication.

[132] Erick J. Weinberg and Ai-qun Wu. Understanding Complex Perturbative Effective Potentials. *Phys.Rev.*, D36:2474, 1987.